

AFOSR-TR- 95 0113



Study of the Vortex-Glass Phase Transition in High T_c Superconductors

Thomas Lemberger
Department of Physics



Accession For	
NTIS	CRASH
DTIC	TAB
Unannounced	
Justification	
By _____	
Distribution /	
Availability Codes	
Dist	Avail and/or Special
A-1	

Air Force Office of Scientific Research
Bolling Air Force Base, D.C. 20332-6448

Grant No. AFOSR-91-0188
Final Report
RF Project 768793/724342

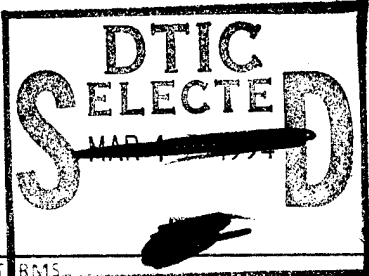
September 1994

19950626 077

REPORT DOCUMENTATION PAGE

Form Approved
OMB No. 0704-0188

Public reporting burden for this collection of information is estimated to average 1 hour per response, including the time for reviewing instructions, searching existing data sources, gathering and maintaining the data needed, and completing and reviewing the collection of information. Send comments regarding this burden estimate or any other aspect of this collection of information, including suggestions for reducing this burden, to Washington Headquarters Services, Directorate for Information Operations and Reports, 1215 Jefferson Davis Highway, Suite 1204, Arlington, VA 22202-4302, and to the Office of Management and Budget, Paperwork Reduction Project (0704-0188), Washington, DC 20503.

1. AGENCY USE ONLY (Leave blank)		2. REPORT DATE		3. REPORT TYPE AND DATES COVERED FINAL	
4. TITLE AND SUBTITLE Study of the Vortex-Glass Phase Transition in High Tc Superconductors				5. FUNDING NUMBERS 61102F 2305/GS	
6. AUTHOR(S) Prof Thomas Lemberger					
7. PERFORMING ORGANIZATION NAME(S) AND ADDRESS(ES) Department of Physics Ohio State University				8. PERFORMING ORGANIZATION REPORT NUMBER AFOSR-TR- 95 0113	
9. SPONSORING MONITORING AGENCY NAME(S) AND ADDRESS(ES) AFOSR/NE 110 Duncan Avenue Suite B115 Bolling AFB DC 20332-0001				10. SPONSORING MONITORING AGENCY REPORT NUMBER AFOSR-91-0188	
11. SUPPLEMENTARY NOTES					
12a. DISTRIBUTION AVAILABILITY STATEMENT APPROVED FOR PUBLIC RELEASE: DISTRIBUTION UNLIMITED				12b. DISTRIBUTION CODE	
13. ABSTRACT (Maximum 200 words) SEE FINAL REPORT ABSTRACT 					
14. SUBJECT TERMS				15. NUMBER OF PAGES	
				16. PRICE CODE	
17. SECURITY CLASSIFICATION OF REPORT UNCLASSIFIED		18. SECURITY CLASSIFICATION OF THIS PAGE UNCLASSIFIED		19. SECURITY CLASSIFICATION OF ABSTRACT UNCLASSIFIED	
20. LIMITATION OF ABSTRACT UNCLASSIFIED					

Final Technical Report for AFOSR-91-0188, 3/91-3/94. T.R. Lemberger, P.I.

Page 1, Section 13, *Abstract*:

This project extended understanding of vortex behavior in oxide superconductors in two important directions. First, we made discoveries regarding the morphology of the defects that pin vortices in films very effectively and regarding the nature of the phase transition that separates the low-magnetic-field, low temperature vortex glass from the high-field, high-temperature vortex liquid. In both cases, our results challenge the status quo. Second, we demonstrated fabrication of $\text{YBa}_2\text{Cu}_3\text{O}_{7-\delta}$ films with a variety of dopants for Cu, and we showed that only a few percent of dopant has a dramatic effect on the superconducting properties, in a way that might be useful in some superconducting devices.

Main body of report, per AFOSR amendment No. 2 dated 03/27/89.

a) Objectives.

Our primary scientific objective was to understand the dynamics of superconducting vortices created in films of the high-temperature superconductor, $\text{YBa}_2\text{Cu}_3\text{O}_{7-\delta}$, by application of a magnetic field perpendicular to the film. "Understanding" includes understanding of the defect that pins vortices in films, and understanding the nature of the phase transition from a vortex glass to a vortex liquid. A natural corollary of this project involved understanding how vortex behavior might be influenced by the simple expedient of substituting a few percent of the Cu atoms with other atoms like Ni and Zn.

Technical objectives included constructing electronics appropriate for measuring the magnitude and phase of extremely small ($\mu\Omega$ -m Ω) sample impedances at frequencies from dc to 20MHz in magnetic fields up to 8 Tesla. Another objective was development of sample fabrication facilities for making large area films of doped $\text{YBa}_2(\text{Cu}_{1-x}\text{M}_x)_3\text{O}_{7-\delta}$, where $M = \text{Ni}, \text{Zn}, \text{Co}, \text{Al}, \text{etc.}$ The final objective was to find the concentration of dopants that optimized vortex pinning.

b) Status of research effort.

All necessary apparatus were operational in the middle of the second year, including a 10 Tesla magnet, high-speed electronics, and software for data analysis. Sample films of $\text{YBa}_2(\text{Cu}_{1-x}\text{M}_x)_3\text{O}_{7-\delta}$ were made at OSU by codeposition and postannealing; films made by laser ablation were obtained from the laboratory of Michael McElfresh at Purdue University. Data were taken and analyzed by the graduate supported by the grant, Dimitrios G. Xenikos, through the third year, at which time he finished his PhD thesis and left the lab.

Extensive measurements of current-voltage characteristics were made on pure $\text{YBa}_2\text{Cu}_3\text{O}_{7-\delta}$ and $\text{YBa}_2(\text{Cu}_{0.98}\text{Al}_{0.02})_3\text{O}_{7-\delta}$ films up to 20MHz to explore vortex behavior. The results of these measurements are described below. As a peripheral project, films prepared using fabrication facilities supported in part by this AFOSR grant were used to explore the effect of dopants on the infrared response of $\text{YBa}_2\text{Cu}_3\text{O}_{7-\delta}$ films; hence publication 2 below cited AFOSR support.

The starting point for understanding the behavior of vortices in $\text{YBa}_2\text{Cu}_3\text{O}_{7-\delta}$ films is to understand the nature of the defect in the crystal structure that pins vortices. Surprisingly, despite the fundamental importance of this issue, very little is known about it. We have made a substantial contribution by measuring the inductance of vortices by measuring the inductance of a long narrow "bridge" patterned into a film as a function of temperature and magnetic field perpendicular to the film. The vortex inductance is intimately connected to the pinning strength - inductance grows as pinning weakens. At low magnetic fields, the bridge inductance grows linearly with field, which means that the total vortex inductance is simply linear in the number of vortices. At higher fields, the intervortex repulsion weakens vortex pinning. It turns out that the dependence of pinning strength on vortex density is extremely sensitive to the nature of pinning sites. We find that pinning is weakened only gradually with increasing vortex density, consistent with pinning sites being lines or planes, but inconsistent with point-like sites, which is the accepted paradigm. A manuscript describing this work is in preparation; results appear in the PhD thesis of Dimitrios G. Xenikos.

An important scientific issue concerns whether the "melting" vortices out of their pinning sites, as T is raised, is a glass-like softening or a true melting phase transition. We have found evidence which supports the phase transition view, and evidence which has yet to be reconciled with the phase transition view. Supporting evidence is that the "universal critical exponents" which describe the power laws by which various measurable quantities depend on T , or field B , or frequency ω , are unaffected when dopants are added to the film. This is nontrivial since the dopants have very strong effects on various "nonuniversal" quantities including the temperature at which the transition occurs. On the other hand, by measuring the frequency dependence of various quantities, in addition to the oft-studied low-frequency measurements, we discovered that the two free parameters in the theory were insufficient to describe the power law behavior of all of the measured quantities. Theory has yet to account for this serious shortcoming. The former result has been published; the latter is in manuscript form. Both results appear in the PhD thesis of Dimitrios G. Xenikos.

c) Publications.

1. "Vortex correlations in the superconducting transition of $\text{YBa}_2(\text{Cu}_{1-x}\text{Al}_x)_3\text{O}_{7-\delta}$ films in high magnetic fields," D.G. Xenikos, J.-T. Kim, and T.R. Lemberger, Phys. Rev. B. 48, 7742 (1993).
2. "Absence of a gap in the reflectance of $\text{YBa}_2(\text{Cu}_{1-x}\text{Ni}_x)_3\text{O}_{7-\delta}$ films," M.J. Sumner, J.-T. Kim, and T.R. Lemberger, Phys. Rev. B 47, 12248 (1993).

4. *"Inconsistent critical exponents for the vortex-glass transition,"* D.G. Xenikos, A.E. Cunningham, T.R. Lemberger, L. Hou and M.W. McElfresh, manuscript in preparation; to be submitted to Physical Review B.
5. *"Inductance of vortices in $YBa_2Cu_3O_{7-\delta}$ films,"* D.G. Xenikos, A.E. Cunningham, T.R. Lemberger, L. Hou and M.W. McElfresh, manuscript in preparation; to be submitted to Physical Review B.
6. *"Statics and dynamics of the mixed state in pure and Al-doped $YBa_2Cu_3O_{7-\delta}$ high temperature superconductors,"* D.G. Xenikos, Ph.D. thesis, The Ohio State University, 1994 (unpublished).

d) Personnel.

Thomas R. Lemberger, Prof. of Physics, Principal Investigator.

Dimitrios G. Xenikos, Graduate Research Associate, Physics Ph.D. program.

e) Interactions.

Presentations:

1. *"Vortex correlation length and critical slowing down in $YBa_2(Cu_{1-x}Al_x)_3O_{7-\delta}$ thin films in high magnetic fields,"* D.G. Xenikos and T.R. Lemberger, Bull. Am Phys. Soc. **38**, 70 (1993). Presented at the 1993 March Meeting of the American Physical Society.
2. *"Kinetic inductance of $YBa_2Cu_3O_{7-\delta}$ in high magnetic fields,"* D.G. Xenikos, T.R. Lemberger, L. Hou and M.W. McElfresh, Bull. Am. Phys. Soc. **39**, 182 (1994). Presented at the 1994 March Meeting of the American Physical Society.
3. *"Vortex dynamics in Al-doped $YBa_2Cu_3O_{7-\delta}$ films,"* D.G. Xenikos and T.R. Lemberger, a poster presentation the Vortex Conference, a Satellite conference to LT-20, held July 1993.
4. *"Pure, doped, and multilayer films of $YBa_2Cu_3O_{7-\delta}$,"* T.R. Lemberger, seminar at Ohio State University, October, 1993.
5. *"The effect of Al doping on the critical scaling of $YBa_2Cu_3O_{7-\delta}$ films in high magnetic fields,"* D.G. Xenikos and T.R. Lemberger, Proceedings of LT-20, held August, 1993.
6. *"Correlation length and time in the vortex-glass critical regime in $YBa_2Cu_3O_{7-\delta}$ films,"* D.G. Xenikos, T.R. Lemberger, L. Hou, and M.W. McElfresh, Proc. of Materials and Mechanisms of Superconductivity Conference, Grenoble, France, July 1994.

7. *"Vortex correlations and pinning in pure and doped YBCO films,"* D.G. Xenikos, seminar given at the National Center for Scientific Research "Demokritos", Athens, Greece, January 1994.
8. *"Vortex correlations and pinning in pure and doped YBCO films,"* D.G. Xenikos, seminar given at the Centre Nationale de Recherche Scientifique, Center de Recherches sur les Tres Basses Temperatures, Grenoble, France, January 1994.

Consultative functions:

Informal contact with Dr. Timothy Peterson at Wright-Patterson AFB, Dayton, OH.

f) Discoveries, etc.

The mobility of vortices can be greatly increased by addition of a few percent of Al or Zn in place of Cu. This should greatly improve the amplification properties of Flux-Flow Transistors under development in other laboratories.

g) Additional relevant information.

None.

ACKNOWLEDGMENTS

To the Ithacas of my mind and the lover of my heart that keep me going, and to my new friend who offered me the trip and now lets me start again.

And to the people that inspire me, my deepest appreciation.

"Ithaca- from the work of C. P. Cavafy:
When you start on your way to Ithaca,
Wish that the way be long,
Full of adventure, full of knowledge.
The Laestrygones and the Cyclopes
And Angry Poseidon, do not fear:
Such, on your way, you shall never meet
If your thoughts are lofty, if a noble
Emotion touch your mind, your body.
The Laestrygones and the Cyclopes
And angry Poseidon you shall not meet
If you carry them not in your soul,
If your soul sets them not up before you.

Wish that the way be long,
That on many summer mornings,
With great pleasure, with great delight,
you enter harbours for the first time seen;
That you stop at Phoenician marts,
And procure the goodly merchandise,
Mother-of-pearl and corals, amber and ebony,
And sensual perfumes of all kinds,
Plenty of sensual perfumes especially;
To went your way to many Egyptian cities,
To learn and yet to learn from the wise.

Ever keep Ithaca on your mind,
Your return thither your goal.
But do not hasten at all your voyage,
Better that it last for many years;

And full of years at length you anchor at your isle
Rich with all you gained on the way;
Do not expect Ithaca to give you riches.

Ithaca gave you your fair voyage.
Without her you would not have ventured on the way.
But she has no more to give you.

And if you find her poor, Ithaca won't have mocked you.
Wise as you have become, so full of experience,
You should understand already what Ithacas mean.

C.P. Cavafy, 1911. Translation from the Greek: G. Valasopoulos"

FIELDS OF STUDY

Major Field: Physics

Branches of Research:

Low temperature of Physics

Superconductivity

Research Advisor: Thomas R. Lemberger, Professor of Physics

TABLE OF CONTENTS

ACKNOWLEDGMENTS.....	ii
VITA.....	iv
TABLE OF CONTENTS.....	vi
LIST OF TABLES.....	viii
LIST OF FIGURES.....	ix

CHAPTER	PAGE
I. INTRODUCTION	1
A. On the issue of true critical currents in High- T_C superconductors.....	1
B. Vortex liquid-glass transition in the mixed state-theoretical aspects.....	5
C. The role of the disorder in the transition-theory and experiment.....	12
II. EXPERIMENTAL TECHNIQUE.....	19
A. Pure and Al doped $\text{YBa}_2\text{Cu}_3\text{O}_7$ films.....	19
B. Experimental set-up.....	26
III. STATICS.....	39
A. Universal characteristics at $T \geq T_g$	39
B. Nonuniversal characteristics at $T \geq T_g$	47
IV. DYNAMICS.....	64
A. Glass phase at $T < T_g$	64
B. Critical region at $T \approx T_g$	78
V. CONCLUSIONS	82

APPENDICES

A. Nonlinear magnetization of YBCO crystals.....	85
B. <i>ac</i> susceptibility apparatus for measuring the transition temperature of high- T_c crystals, sintered samples, and films.....	87
LIST OF REFERENCES	89

LIST OF TABLES

Table	Page
1. Critical scaling parameters of $\text{YBa}_2(\text{Cu}_{1-x}\text{Al}_x)_3\text{O}_{7-\delta}$ films. The uncertainties represent possible systematic errors in the calculations..	63
2. Summary of phenomenological laws in this work.....	84

LIST OF FIGURES

Figure	Page
1. "Vortex loop" excitation (continuous line). The vortex is pinned on weak point disorder.....	8
2. Vortex pinning in (from left to right) weak point disorder, strong point pins, and columnar defects. A current perpendicular to the page plane pushes the vortices to the right. [Ref. 37].....	13
3. Scanning electron microscope pictures of a 2 at. % Al, 1000 Å-thick film, made by codeposition and <i>ex situ</i> post annealing.....	21
4. T_c vs. dopant concentration for Al- and Ni-doped YBCO films. T_c corresponds to the onset of the diamagnetic response of the film.....	23
5. ab-plane resistivity of 3000 Å-thick, Al-doped YBCO films.....	25
6. Pattern design of the YBCO microbridge and 4-terminal wiring.....	28
7. Two configurations for 4-terminal I-V measurements. Values of R, R' are given in the text.....	30
8. Heterodyning scheme used for dynamical measurements at frequency range 500 Hz -20 MHz.....	33
9. Calibration of the electronic setup with: 1 mV reference (top); inductive microbridge (middle); 50 Ω resistor at the rf preamp input (bottom).....	35
10. I-V curves on a 2 at. % Al film, at B=4 T. The dashed line indicates the transition at $T_g=62 \pm 1$ K. Curves are taken approximately 1 K apart.....	42
11. Glass phase boundary $B_g(T)$ for three samples of variable Al	

CHAPTER I

INTRODUCTION

A. On the issue of true critical currents in high- T_c superconductors

The early reports on the statics and dynamics of the mixed state in the high-temperature superconductors (HTSC) carried a great deal of skepticism over whether true critical currents were attainable in these new materials. It seemed that the high temperatures, over which the superconductivity now persisted, conspired with a few anomalous properties of the materials (especially the short coherence length and the sample anisotropy) to destroy their defining property of zero linear resistivity in the superconducting state in the presence of applied magnetic field. In fact, power dissipation in the mixed state was an extensively studied phenomenon in the case of conventional superconductors. The new concern, however, was whether it were now possible to pin the magnetic flux quanta on the sample disorder, prohibiting their mobility in a *dc* current flow and thus diminishing the power dissipation in the high- T_c samples. A huge effort was then launched to understand these phenomena, with many groups around the world competing for innovation and applicable results, our own group included.

The issue of true critical currents was soon related to that of the nature of the "irreversibility line"^{1,2} $T_{ir}(B)$. This is a boundary in the phase diagram that separates the high-temperature reversible magnetization region, from the low-T irreversible magnetization one. Initially, the similarity of the functional form of the irreversibility line

$$T_C - T_{ir} \propto B^{2/3} \quad (1)$$

in HTSC with the Almeida-Thouless line³ in spin glasses suggested that magnetic flux in the mixed state could be considered as "frozen" in some random configuration, rather than participating in a long range magnetic order as, for example, in a triangular array.⁴ Detailed magnetization measurements though indicated that the fluxons in the irreversible region were not frozen, but were slowly rearranging themselves to eliminate magnetic field gradients in the sample at logarithmic relaxation rates ("giant flux creep").⁵ The fact that the critical state could not survive in HTSC crystals provided strong evidence that the disorder in the sample was not effective to pin the vortices in the mixed state.

Transport measurements were also interpreted along the same lines. The data for the temperature dependence of the resistivity $\rho(T)$ were plotted to fit Arrhenius curves $\rho \propto e^{-U/kT}$ and values for the potential barrier $U(B,T)$ (or a distribution of barriers) were extracted.⁶⁻¹¹ The suggestion was that thermally activated vortices (or bundles of vortices) could overcome this energy barrier, consistent with an Anderson-Kim picture¹²⁻¹⁴, and subsequently dissipate energy. Finally Tinkham¹⁵, by fitting the

resistivity data on $\text{YBa}_2\text{Cu}_3\text{O}_{7-x}$ (YBCO) crystals of Inui *et al.*⁸ using a simplified phenomenological analogue of the vortex motion over some reasonable potential barrier¹⁶, went all the way to suggest that thermal vortex fluctuations dissipating energy would dominate at liquid N_2 temperature, even in a room temperature superconductor. A true critical state^{17,18} could not be obtained at useful temperatures in HTSC.

The experiment that stirred the problem again providing a new angle to see things was that of R. Koch *et al.*^{19,20} This work showed that, below the irreversibility temperature (now called glass temperature T_g), the linear *dc* resistivity was vanishing faster than the Arrhenius behavior, following a power law $\rho \propto (T-T_g)^{\nu(z-1)}$, with $\nu(z-1)=6.5\pm0.6$. The data were interpreted as evidence for a *phase transition* at T_g , separating a vortex-liquid phase, where thermal fluctuations dominate, from a vortex-glass phase, with only short-range translational and long-range orientational order of the Abrikosov lattice surviving. This phase transition had been previously predicted by M.P.A. Fisher on theoretical grounds.²¹

From then on, a number of different theoretical models, which deal with the statics and the dynamical characteristics of the mixed state and often introduce novel phases with qualitatively different correlations among the vortices, have been proposed. The experimental evidence for the existence of a phase transition at T_g has been also building stronger, with current-voltage (I-V) curves in YBCO films¹⁹ and twinned crystals²² supporting the idea of a phase boundary associated with the "irreversibility line"² in these materials. The details, though, of the pinning

mechanism that gives rise to the critical behavior are still a matter of controversy. Fisher and coworkers^{21,23} model vortex behavior when vortex pinning is from *microscopic quenched disorder*, and they find a second order phase transition separating a vortex-glass phase with vanishing linear resistivity from a vortex-fluid phase with a finite low-voltage resistivity. However, the nature of the phase transition may be quite different from that of the vortex glass theory, if *correlated disorder* in extended defects is responsible for the flux pinning in these samples.²⁴ Since both models are consistent with measured exponents and scaling functions for $V(I)$, one must look to non-universal parameters to distinguish them.

Our work will move along two directions: First, we will check the universality of the critical power laws in a variety of doped (as well as pure) samples, that would support the concept of phase transition truly exists at T_g . Second, we will measure parameters that are non-universal in these samples, such as the resistivity and the pinning strength, in an effort to distinguish which of the many types of disorder is dominating in the vortex pinning, and relate to the appropriate theoretical models. Before we proceed to describe our measurements, we will put forward in section B of the introduction the theoretical tools that we borrow from the work in vortex glass, which we will use throughout our analysis. In addition, in section C of the introduction, we will describe the contribution of our work in the field, and its relationship with the rest of the experimental and theoretical advances in the recent literature.

B. Vortex glass phenomenology- the role of the disorder

In this section we will present the basics of the phenomenological approach to the glass transition which is developed by Daniel Fisher, Mathew Fisher and David Huse (FFH).²³ Their analysis provides the means to describe transport measurements close to T_g in terms of "vortex-loop" fluctuations, and will be used extensively in our work. We will see that, although its principles cannot not be confirmed directly from the experiment, the method offers an insight on the role of the disorder in the sample. Here, we examine the Larkin length, the phenomenology of the vortex loops, the correlation length and time, and finally the scaling characteristics of the transition at T_g .

As a starting point, the vortex is assumed to be a string-like object with certain elasticity ϵ_0 carrying magnetic flux ϕ_0 , which tends to be pinned in a sea of surrounding microscopic crystal imperfections. Then, as argued by Larkin and Ovchinnikov²⁵, the random forces due to the weak core pinning (core $\sim \xi$ in diameter) will distort the flux lattice at large distances. Let us assume that a transport current J passes in a direction perpendicular to the applied field. Then, a Lorentz force acts on the vortex, a segment L_1 of which may become unpinned and move sideways a distance L_\perp possibly smaller than L_1 (see Fig. 1). The gain in the free energy $F(L_\perp, L_1)$ by this motion is $J\phi_0 L_\perp L_1$. The energy cost, given that the vortex is approximated as a string with elasticity ϵ_0 per unit length, is $\epsilon_0 L_\perp^2 / L_1$. One writes

$$F(L_\perp, L_1) = \epsilon_0 L_\perp^2 / L_1 - J\phi_0 L_\perp L_1 - (\gamma \xi^2 L_1)^{1/2} \quad (2)$$

The third term in the above expression is the contribution from pinning. In the case of random point defects, as is assumed in FFH, the pinning energy $\langle \epsilon_{\text{pin}} \rangle$ of a stiff vortex of any length averages out to zero. On the other hand, the fluctuations of the pinning energy do not vanish, and

$$\langle \epsilon_{\text{pin}}^2(L_1) \rangle = \gamma \xi^2 L_1 \quad (3)$$

Here, γ is a measure of the pinning strength, and ξ the Ginzburg-Landau coherence length.²⁶ Then, minimizing the energy (Eq. 2) with respect to L_1 at $L_\perp = \xi$ and $J=0$, we get the Larkin pinning length for the moving vortex segment

$$L_{\text{pin}} = (\epsilon_0^2 \xi^2 / \gamma)^{1/3}. \quad (4)$$

On length scales up to L_{pin} , the distortions of the vortex line is smaller than the coherence length ($L_\perp < \xi$), which means that the vortex system will look as a lattice. However, at larger scales, "dislocation loops" (distortions of the triangular vortex array where a vortex segment progresses one or several lattice spacings away, locally rearranging the vortex distribution) of length L_1 will grow, because their contribution in the free energy is also $\epsilon_0 L_\perp^2 / L_1$.²³ Thus, at lengths larger than L_{pin} the vortex lattice description breaks down as far as the translational order goes. On the other hand, according to FFH the orientational order of the lattice survives. This particular vortex phase has been named "vortex-glass".

The next principle of the vortex glass phenomenology concerns the energy of the excitations of the vortex system. Making an analogy of the vortex line in quenched disorder to a "directed polymer in a random medium", FFH use the numerical results from the latter as an indication that the transverse displacement L_{\perp} of a vortex-line segment of length L_{\parallel} scales as

$$L_{\perp} \sim L_{\parallel}^{\zeta} \quad (5)$$

with an exponent $\zeta \approx 0.6$, a value *larger than 0.5* (which corresponds to thermal fluctuations and no pinning).²⁷ Then a typical vortex excitation (see Fig.1) can be thought as a "vortex loop" consisting from a vortex segment in the opposite direction at the initial position of the vortex segment that moved, connected to the final position of the moved vortex segment. The area of the loop is then

$$S = L_{\perp} L_{\parallel} \sim L_{\parallel}^{\kappa} \quad (6)$$

with $\kappa = 1 + 1/\zeta$. According to the model, the vortex loop can involve many vortices, so that L_{\perp} can exceed the intervortex distance: A segment from a vortex can move to the position occupied from another segment of the nearest vortex before it move to the next nearest neighbor vortex, and so on. It is not clear if the excitations of a multiple vortex-line array are preferred in the vortex system in the HTSC instead of

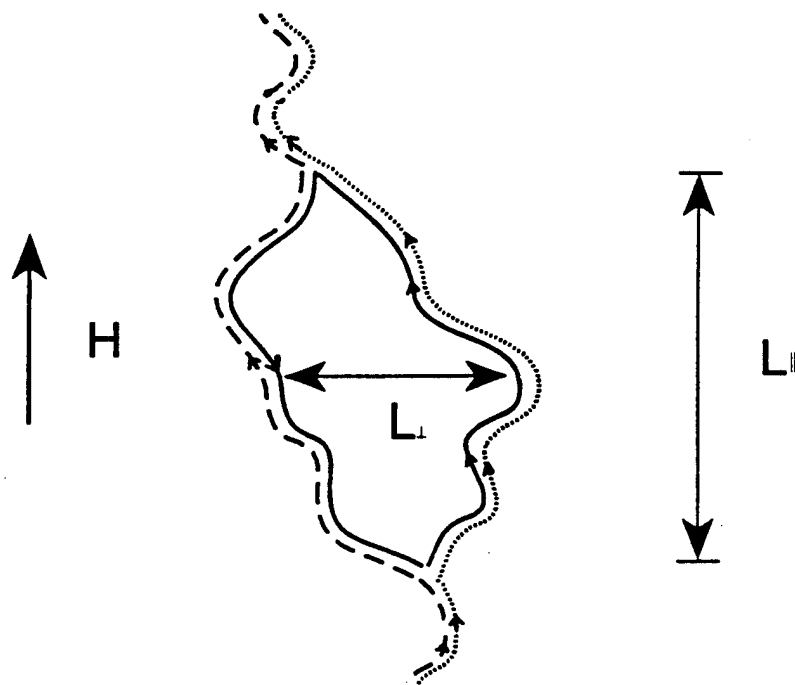


Figure 1. "Vortex loop" excitation (continuous line). The vortex is pinned on weak point disorder.

single vortex loop excitations. Leaving all possibilities open, FFH define a "stiffness coefficient" Y for the system of vortices involved in the vortex loop, so that they can postulate that the elastic energy of the excitation is

$$Y L_1^2 / L_1 \sim Y L_1^{2-1/\zeta}. \quad (7)$$

Then, balancing this elastic energy against the Lorentz energy of the vortex excitation $J\phi_0 L_1 L_1 \sim J L_1^2$, FFH obtain an equilibrium value of the transverse length of the vortex loop $L_1 \equiv \Lambda$ (at zero temperature), in the presence of transport current:

$$\Lambda = (Y/J)^{1/(2/\zeta-1)} \quad (8)$$

This is the size to which a fluctuation must grow before the current will drive it off to infinite radius. Note that the pinning information in this analysis is all contained in the exponent ζ , rather than with an extra term in the free energy expression as in the case of Larkin and Ovchinnikov (Eq. 2).

In the next step, FFH estimate the electric field generated by fluctuations of size Λ at a temperature T : If there is an energy barrier B_A associated with such fluctuation, which relates to the equilibrium length Λ through an (unknown) exponent ψ , such that

$$B_A \sim \Delta \Lambda^\psi, \quad (9)$$

where Δ is some appropriate constant that indicates the barrier height, then the resulting electric field generated by the transport current in the sample is

$$E(J) \sim \exp[-B_A/kT] \sim \exp[-(J_T/J)^\mu] \quad (10)$$

where $\mu = \psi/(2/\zeta - 1)$, and $J_T \sim Y(\Delta/kT)$, k =Boltzmann constant and T the temperature. The linear resistivity in the vortex glass is identically zero (*assuming of course that $\zeta \neq 0.5$*). Moreover, the expression (8) gives a nonlinear voltage which becomes exponentially small for current densities $J \ll J_T$. Thus, the theory of vortex glass predicts the existence of true critical currents in the mixed state.

In the vicinity of the glass transition, the theory resorts to another scaling argument, in order to estimate the electric field. It involves the "vortex correlation length" ξ_G , which is defined as the range of phase coherence in the lattice. This means that vortex loop fluctuations separated by distance less than ξ_G are correlated. The vortex correlation length is expected to diverge at the transition temperature T_g as $\xi_G \sim |T - T_g|^{-\nu}$, but the exponent ν is not estimated. In general, in an anisotropic material the correlation length parallel and perpendicular to the field could be different. However, the vortex glass theory assumes that they diverge with the same exponent ν . Furthermore, there is a second quantity assumed to diverge at the phase boundary: the vortex correlation time $\sim \xi_G^z$, with z the dynamical critical exponent, estimated to be in the range $z = 4 - 7$. Above T_g , this correlation time can be thought as the lifetime of vortex fluctuations due to thermal excitation.

Following the above definitions, FFH provide a units argument to relate the exponents z , ν of the theory to scaling expressions of the conductivity around T_g : Since $E = -\partial A/\partial t$ and the vector potential A enters the Ginzburg-Landau equation as an inverse length, E presumably scales as $1/(\text{length} \times \text{time})$. In addition, $J \sim \partial f / \partial A$, where the energy density f scales as $(\text{length})^{-D}$ and D is the dimensionality of the problem, suggesting that J scales as $(\text{length})^{1-D}$. Considering the length ξ_G and the time scale ξ_G^2 of the model, one concludes to a scaling expression

$$E \sim J \xi_G^{D-z-2} E_{\pm}(J \phi_0 \xi_G^{D-1}/kT) \quad (11)$$

$E_{\pm}(x)$ are scaling functions for temperatures above (+) and below (-) the transition temperature T_g , and should be universal in the materials where the vortex-glass transition occurs. The theory determines the scaling functions in certain limits:

$$E_{\pm}(x) \sim \exp(-a/x), \text{ when } x \rightarrow 0, \quad (12a)$$

$$E_{+}(x) \sim E_{-}(x) \sim \beta x^{(z+2-D)/(D-1)}, \text{ at large } x \quad (12b)$$

where a and β are universal constants. Then, at $T=T_g$ where $\xi_G \rightarrow \infty$ (and thus $x \rightarrow \infty$), a power law is expected for the current-voltage characteristic:

$$E \sim J^{(z+1)/(D-1)} \quad (13)$$

It is clear from the above qualitative units analysis that a different assumption for the length and time scales that are relative to the problem would lead to different combinations of the critical exponents ν and z in the exponents of the power laws. We will address this issue in our measurements in chapter III.

C. The role of the disorder in the transition- theory and experiment

The nature of the disorder that pins the flux lines in HTSC is still a controversial issue. As we noted in the previous section B, the vortex-glass model assumes that only microscopic quenched disorder is relevant to the problem. FFH maintain that their analysis could accommodate mesoscopic disorder (such as twin boundaries) in the order of the intervortex spacing length scale. However, it is not clear that the exponent $\zeta \neq 0.5$ of the theory (and thus all the critical exponents of the transition) will be unaffected in that case. Furthermore, the assumption that a single critical exponent ν characterizes the divergence of both ξ_{\parallel} and ξ_{\perp} at T_g could very well not hold for disorder of certain dimensionality (2-D grain boundaries, 1-D screw dislocations, etc).

In Fig. 2 we show some ways that the flux lines can be deformed in the sample. In the left, microscopic disorder (in the form of perhaps oxygen vacancies) weakly bends the vortices. In the middle, we show flux lines strongly pinned in point defects, when a Lorentz force is pushing them to the right. Another alternative can be pinning in columnar defects (picture on the right), where the vortices could move by the formation of kinks which nucleate by thermal fluctuation or large current

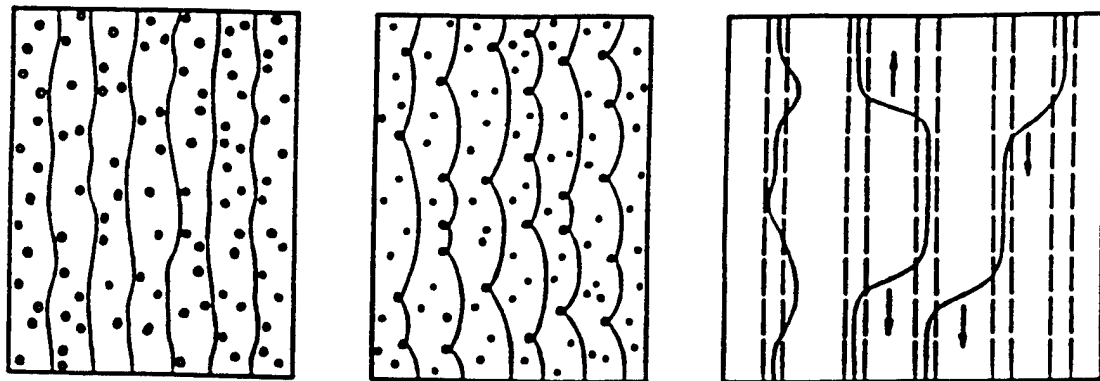


Figure 2. Vortex pinning in (from left to right) weak point disorder, strong point pins, and columnar defects. A current perpendicular to the page plane pushes vortices to the right. [Ref. 37]

density. Comparing the schematic figs. 1 and 2, we see that, in all cases of defects, the vortex excitations could be described as vortex loops, although the concept was initially perceived for quenched disorder. Starting from this purely phenomenological (unproven) point, we will keep the terminology of the vortex-loop that we described in the previous section, but we will be ready to consider a different relationship between its transverse ξ_{\perp} and parallel-to-field ξ_{\parallel} components if needed.

There are currently two theories, in addition to the vortex glass model, which embody specific types of defects and predict a low-temperature glass phase in the mixed state of the HTSC: the collective pinning theory and the Bose glass theory. Contrary to the vortex glass model, where all the information about pinning is included in the exponents ζ and μ (see eqs. 5, 10) through the analogue of the "directed polymer", the collective pinning theory is a statistical solution of the problem of a collection of vortices in the presence of point disorder. The theory generalizes the free energy expression of Eq. 2, by treating the flux lattice as an elastic medium, and *derives* the exponent μ of the glass phase. It treats as special cases the statics and dynamics of a single vortex and that of a collection of vortices of various sizes with respect to the Larkin length, and describes various regions in the H-T plane that may or may not be accessible in HTSC.

The Bose glass model, on the other hand, considers vortex pinning *columnar defects*, and predicts that $\xi_{\parallel} \propto \xi_{\perp}^2$, which leads to different scaling expressions in the flux fluid and glassy phase. In particular, Eq. 11 of vortex glass model becomes

$$E \xi_1^{z'+1} \approx E_{\pm}(J\phi_0\xi_1\xi_1/kT) \quad (14)$$

Then, one can find a relationship between the vortex glass exponents ν , z and those of the Bose glass ν' , z' , by comparing with Eq. 9:

$$\nu' = 2\nu/3 \quad (15a)$$

$$z' = (3z+1)/2 \quad (15b)$$

Furthermore, the critical exponent in the glass phase for the Bose glass is $\mu = 1/3$. We will discuss the success of the proposed theories to describe our data in chapters III and IV of this work.

Experiments testing the universality of the critical scaling in a variety of samples quickly followed the findings of Koch *et al.*¹⁹ The direction of the research moved to either look at samples of different anisotropic character (such as $\text{Bi}_2\text{Sr}_2\text{CaCu}_2\text{O}_8$, $\text{TlSr}_2\text{Ca}_2\text{Cu}_3\text{O}_9$, YBCO) -thus changing the physiognomy of the vortex, or look at different disorder characteristics (ex., point or columnar defects) - thus changing the size and the strength of the vortex pinning sites. As the quality of the samples improved, and as the disorder becomes better characterized, these experiments revealed a wide variety of phenomena associated with T_g , and led to improvements of the theories.

Although there is clear evidence for critical scaling in a variety of samples, there is some diversity in the published results. For example, the self consistency of

the critical scaling in YBCO microtwinned crystals was checked by the AT&T group²² and the group at Caltech^{28,29}, but led to different critical exponents: $z=5$, $\nu=1.6$, and $z=3$, $\nu=1.2$ respectively. The scaling functions between crystals and films were also different. This was indirect proof that the disorder could alter the nature of the transition in a qualitative manner, and thus, special care should be taken to characterize the sample defects. Then, high quality untwinned crystals showed evidence of a *first order transition* at the temperature associated with the irreversibility line.³⁰⁻³⁴ There is evidence that this melting transition is distinct from the vortex glass transition, which occurs only for disorder beyond a certain critical amount.^{35,36} This transition has been predicted from theoretical considerations of the effect of thermal fluctuations on the elastic moduli of the defect-free flux lattice.³⁷⁻⁴¹ Kwok *et al*⁴² studied the effect of twin planes on the transport measurements when the vortex is at an angle with respect to the plane of the defects. Finally, a number of groups showed a large enhancement of the critical currents and a raise in T_{ir} in crystals with columnar defects.⁴³⁻⁴⁵

How well does the theory describe the diverse experimental results and the new information of specific types of disorder affecting the transition? First of all, the existence of a phase transition at T_g is still a matter of controversy, although it is consistent with the bulk of the experimental evidence. Then, the scaling arguments in the vicinity of T_g or the exponent μ extracted from the data of the glass phase cannot distinguish between the vortex glass model (in the FFH phenomenological picture or the collective pinning solution^{26,51}) and the Bose glass model. In fact, the

collective pinning theory has not explicitly related the pinning details of the sample to a phase boundary in the mixed state, although it is consistent with a glass and a liquid phase at (in general unspecified) parts of the phase diagram. The Bose glass theory is definitely very successful in crystals with columnar defects (parallel or splayed) induced by heavy ion bombardment. However, the predicted dependence of the phase transition temperature on the angle of the magnetic field with respect of the defects was not shown in films.⁴⁶⁻⁴⁸ Recent Monte-Carlo simulations based on a mean field approach by Stroud and coworkers fit with no adjustable parameters the phase boundary at YBCO, in both clean samples and ones with columnar defects.^{49,50} However, some of the results for the pinning strength that we show in chapter IV (especially the field dependence of the Labusch parameter) cannot be incorporated in the simulations at their present form. Finally, we should mention that all the above theoretical models are seen with a large degree of skepticism from a large part of the scientific community, which carefully looks for more moderate conventional ideas to explain the experimental results, without the introduction of a vortex phase transition at all.

In our work we focused on films, where little has been done. We address several key issues: a) Is there a vortex phase transition in the films at a field-dependent temperature $T_g(B)$? b) What is the nature of the low temperature phase (vortex glass or Bose glass) and what kind of disorder is responsible for the critical scaling? c) How can one tune the non-universal parameters of the transition without affecting its universal characteristics?

Thus, for the first time in the literature we varied materials parameters by doping the YBCO film. We verified that the scaling exponents and functions of the conductivity around T_g are unchanged, a strong argument for the existence of a phase transition at T_g .^{54,55} Then our effort was coordinated on the study of the statics and dynamics of the two vortex phases at both sides of the transition, and find evidence that correlated disorder is responsible for the transition. We propose several empirical formulas describing the complex conductivity of the vortex phase, and we estimate the magnitude of the fundamental quantities of the transition, namely, the vortex correlation length and time. Finally, we suggest alternative ways to model the vortex excitations in the light of the vortex-glass and Bose-glass theoretical models which are available at present.

CHAPTER II

EXPERIMENTAL TECHNIQUES

A. Pure and Al-doped $\text{YBa}_2\text{Cu}_3\text{O}_7$ films

Doping is widely used for altering properties of the normal and the superconducting state in a continuous fashion, in order to draw relationships between the fundamental quantities and the microscopic information at an atomic level. In our experiment, Al was substituted for Cu in the YBCO lattice, in order to change the pinning characteristics of YBCO films. Yet, the role of pinning in many of the quantities that we measure, such as the critical current density or the transition width, is still quite a controversial issue, and forbids a quantitative estimation of the degree of change in pinning that we obtain through doping. Consequently, great emphasis in this work is given to identify the nature of the sites in the sample that are responsible for vortex pinning phenomena. It is therefore important to discuss the fabrication technique and the procedures followed to characterize the films, in order to find quantities that are sensitive probes of pinning.

The films used in this work are made by either codeposition and *ex situ* annealing⁵⁶, or by laser ablation. In particular, all the doped films were made by the first method, developed by Jin-Tae Kim in 1991, while some pure laser ablated YBCO

films were used at later stages of our experiments. The doped films were prepared on (001) SrTiO_3 substrates by codeposition of Y, BaF_2 , Cu and Al in the presence of 3×10^{-6} Torr of O_2 . Y was evaporated from an electron-beam source, while BaF_2 , Cu and Al were evaporated from heated filament sources. The evaporation rates were controlled independently by quartz crystal deposition controllers. The films were annealed *ex situ* in a tube furnace in flowing oxygen. The tube furnace was ramped quickly up to 870 °C at 40 °C/min and then slowly up to 900 °C at 5 °C/min to avoid thermal overshooting, left at 900 °C for 1 hour, cooled to 500 °C at 5 °C/min, left at 500 °C for 1 hour to oxygenate as fully as possible, and finally cooled slowly to room temperature. While the sample is at the highest temperature, 900 °C, the oxygen is bubbled through distilled water at room temperature. Annealing below 900 °C or shorter than 1 hour does not improve the sharpness of the transition, indicating that it does not raise the oxygen content of Al doped films. The method was successfully used for producing also Ni- and Zn-doped films.

X-ray diffraction patterns for films with less than 11 % dopant concentration are the same as for highly oriented pure YBCO films, with no evidence for second phases. Furthermore, evidence for the high orientation of the *ab* planes parallel to the film plane is provided by scanning-electron microscopy (SEM). As an example, we show in Fig. 3 SEM pictures of the surface of a 2% Al, 1000 Å-thick film. Clearly, there is no evidence of misoriented grains in the surface topography which appear only at Al concentrations in excess of 4 %. The most prominent defects we observe are holes about 1000 Å in diameter, which occur in groups of 1-5 clustered about 1

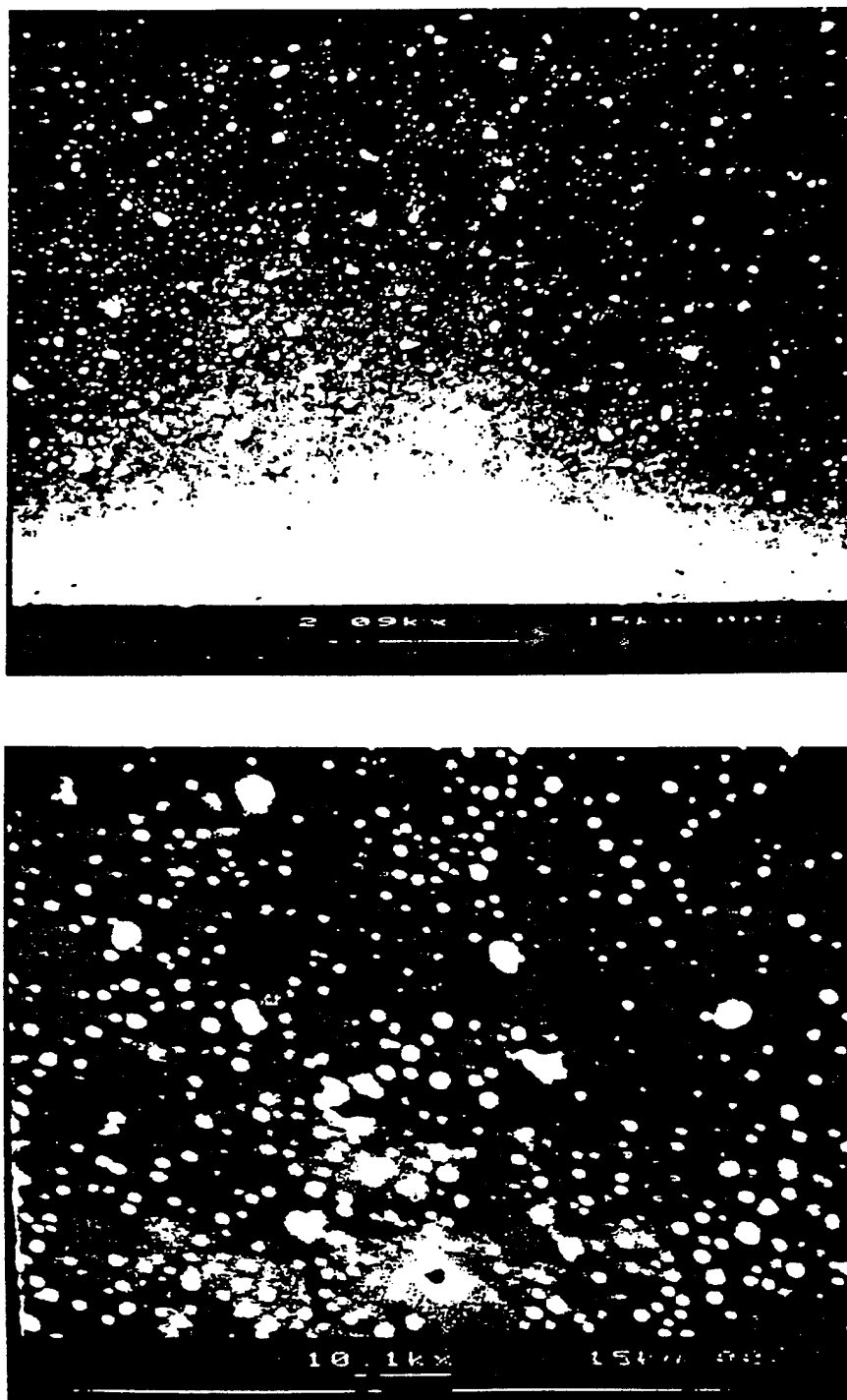


Figure 3. Scanning electron microscope pictures of a 2 at. % Al, 1000 Å-thick film, made by codeposition and *ex situ* post annealing.

μm apart. The clusters are $20\ \mu\text{m}$ apart. These holes may arise from the collective release of fluorine gas from the films during postannealing. The similarity of our results of our films made by either codeposition or laser ablation without such defects indicates that they did not play any fundamental role -for vortex pinning- in our measurements.

The mean field transition was measured using the apparatus in Appendix B. In Fig. 4 we compare the results in Al with the T_c of Ni-doped films made by the same technique. We find that the T_c in the Ni-doped films dips about 15 K over the first 5% of dopant concentration, contrary to Al-doped films where a plateau appears. As will become evident in chapter III, this attractive feature of the Al films is instrumental when one compares measurements of the transition width in the presence of magnetic fields between samples with different dopant concentration.

Two of our films were made by the method of pulsed laser ablation by Lifang Hou and Mike McElfresh in Purdue University. The films were pure YBCO, deposited on a heated SrTiO_3 and a LaAlO_3 substrates. After the deposition, they were left in the evaporation system in an O_2 atmosphere for several hours to anneal, as the temperature was gradually reduced. As far as the value of T_c , the sharpness of the transition and the normal state resistivity, the laser ablated film on SrTiO_3 was indistinguishable from the codeposited one. The film on LaAlO_3 had a broad transition with $T_c=82\ \text{K}$ and was used for setup calibration purposes.

Following their characterization by *ac* susceptibility, the films were patterned into microbridges suitable for 4-terminal measurements by standard photolithography

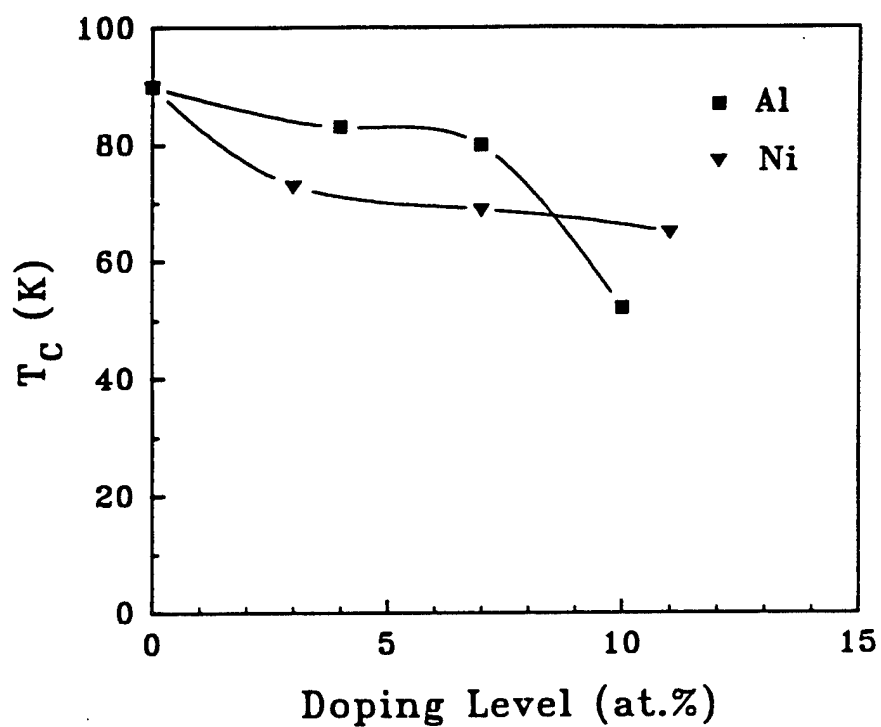


Figure 4. T_C vs. dopant concentration for Al- and Ni-doped YBCO films. T_C corresponds to the onset of the diamagnetic response of the film.

and chemical etching using dilute (0.03%) nitric acid. The etching rate was about 400 Å/min. The strips were typically 15-50 μm wide and 100-600 μm long. To reduce the contact resistance, approximately 400 nm of Ag was deposited on each pad, and then the samples are oxygenated again in a tube furnace at 450-500 °C for 1 hour. Miniature coaxial cables were attached by pressing indium on the pads and then pressing the wires into the indium. The resulting contact resistance was typically in the order of m Ω or less.

Figure 5 shows the ab-plane resistivity $\rho(T)$ for four 3000 Å films, which is measured by the usual *ac* technique, first published in ref. 56. The applied current density through the strip is about 30 A/cm², and its frequency 10-100 Hz. The resistivity $\rho(T)$ of the doped films is metallic from T_c to room temperature, similar to that of the pure YBCO film. A transition to semiconducting electron transport is evident only in the 11 at. % Al film that contains misoriented grains, where the resistivity exhibits a plateau just above T_c .

After considering the information from all characterization measurements described above, we selected only $\text{YBa}_2(\text{Cu}_{1-x}\text{Al}_x)_3\text{O}_{7-\delta}$ films with $x \leq 0.04$ for our measurements on the statics and dynamics of the mixed state. Our choice was directed by the need to perturb the pinning characteristics in the film without altering them qualitatively. Thus, misoriented grains or non-metallic normal state resistivity had to be avoided. At low Al concentrations, the SEM pictures of the film surface are indistinguishable from those of pure YBCO. The T_c decreases by only ~ 1 K per at. % dopant concentration. The 20%-80% transition width measured by either *ac*

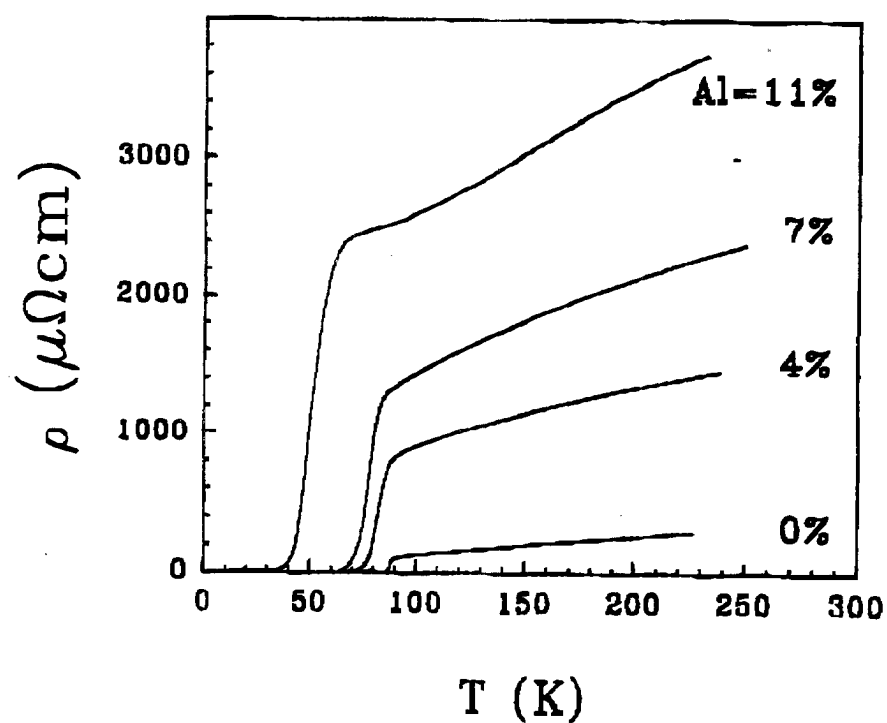


Figure 5. ab-plane resistivity of 3000 Å-thick, Al-doped YBCO films.

susceptibility or transport (at zero applied *dc* field) increases progressively from 1-2 K at pure YBCO to 4-5 K for the 4 at. % film. Still, the above do not guarantee that the defects in the sample (in the form of point quenched disorder, grain or twin boundaries, screw dislocations etc.) are affected by doping. They provide us, however, with a variety of parameters *controlled by doping* that will be finally associated to the pinning characteristics of the flux lattice.

B. Experimental setup

The bulk of our work consists of complex impedance measurements on the high- T_c films over a wide frequency range $10 - 2 \times 10^6$ Hz. In general terms, we have followed the *ac* lock-in technique, though the cabling and the general configuration varies at different frequency ranges. Specifically, the commercial lock-in amplifiers detect signals typically up to 100 KHz. In the radio-frequency (rf) range above this crossover, the sample response is heterodyned into audio frequency signals that can be detected by the commercial lock-in. The described apparatus has a sensitivity of ~ 10 nV and can resolve changes in the impedance of a microstrip corresponding to a few percent of the magnitude of its geometrical inductance, at excitation currents $\sim 10^{-5}$ A. Below, we describe the configuration and the specifications of our apparatus in some detail.

The central ideas behind our design can be summarized as follows:

- 1) Flexibility: Easy computer-controlled frequency sweep from 10 Hz to 20 MHz. The necessary changes in the cabling at the crossover $f=100$ KHz should only involve

the room temperature electronics.

- 2) Capability to measure the impedance of the microbridge which is in the order of $m\Omega$ and switches over from purely inductive at very low temperatures to resistive when approaching T_c .
- 3) Ability to record both linear and nonlinear current-voltage characteristics in the whole frequency range.
- 4) Sensitivity to resolve changes in the order of a fraction of the ($m\Omega$) physical inductance of the strip, at low current densities, where the sample response is linear to the excitation current.
- 5) Wiring: The measurement should not depend on the length of the wires connecting the sample to the room temperature electronics, so that the film can be placed in the core of a superconducting magnet. Any background from parasitic pickup in the cables should be reproducible on a day-to-day basis and consist only a small fraction of the measured signal.

Figure 6 shows the design of the pattern that was used in the wideband conductivity measurements. Dark colored is the film, white is the etched film area. Most of the film is used as a ground plate, connected to the jacket of the current bearing coaxial cable, which in turn is grounded to the sample holder in the cryostat, 1-2 cm away from the substrate. We can easily estimate the physical inductance of the strip in such design: When current $I \sin(\omega t)$ passes through the strip, a magnetic field is produced $B = [\mu_0 I / (2\pi r)] \sin(\omega t)$, with $r > w$ the half width of the strip. Then the induced voltage between the two voltage leads is $V = 3[\mu_0 I \omega d / (2\pi)] \cos(\omega t)$,

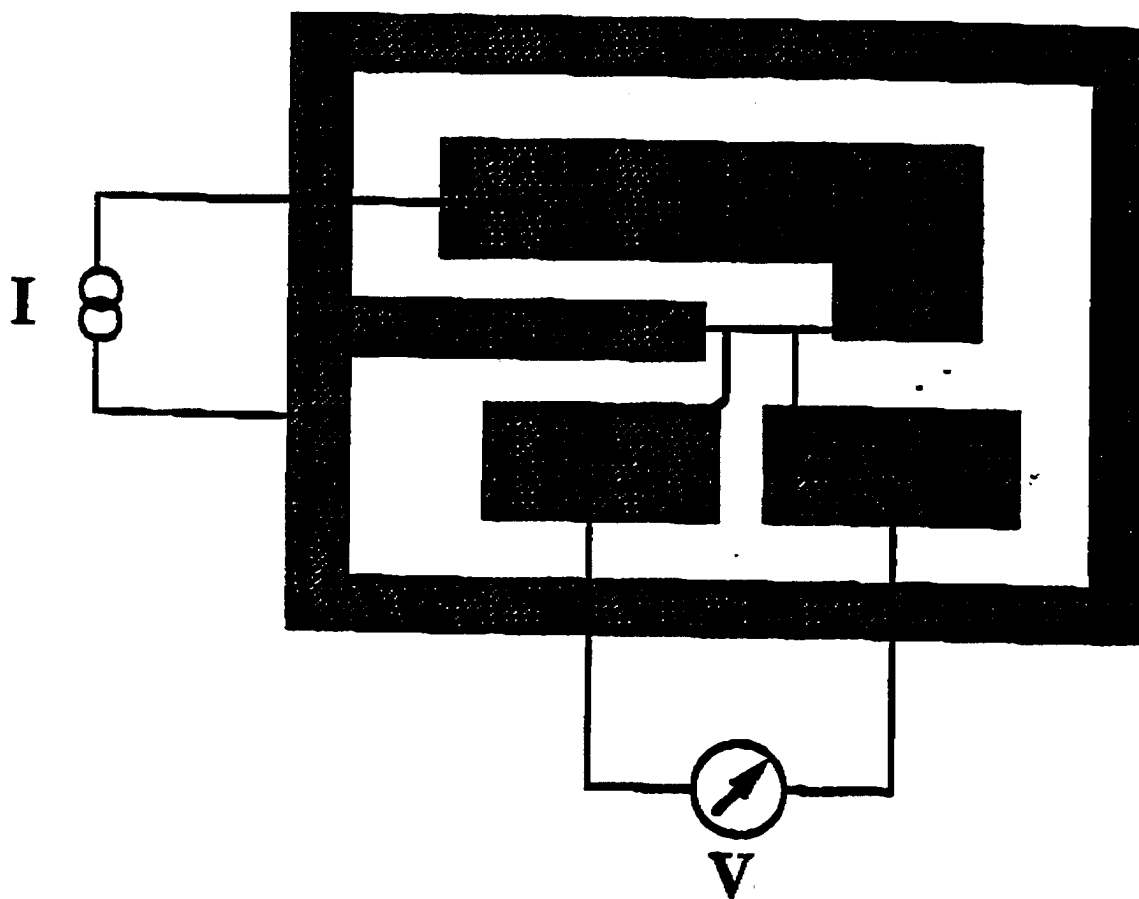


Figure 6. Pattern design of the YBCO microbridge and 4-terminal wiring.

integrating r from, say, $r \equiv w/2 = 20 \mu\text{m}$ to 2 mm , with ℓ the length of the strip. Then, the physical inductance of the strip is

$$L_p \approx 0.75 \mu_0 \ell. \quad (16)$$

The fact that the current density peaks at the film edges does not alter this result by more than a few percent. For the sample patterns of chapter IV, $\ell = 600 \mu\text{m}$, thus $L_p \approx 0.5\text{--}0.6 \text{ nH}$. The signal we want to detect will always ride on this physical inductance.

The system described here is based on the 4-terminal configuration, which is appropriate for wide-range impedance measurements of a low-grounded superconducting microbridge⁵⁷ and is the typical way to measure low-frequency current-voltage (I-V) characteristics of the films. The components of the complex impedance of the load are measured by a commercial lock-in, whose bandwidth is extended by using a heterodyning technique. The variation of the (very small) load is overcome by careful termination of the coaxial cables that minimizes reflections, pick-up, and the sensitivity of the measurements to the length of the wires.

In Fig. 7, we show two alternative ways that the sample is connected to the detection electronics for a 4-terminal impedance measurement. The one most commonly used (Fig. 7b) has a large current-limiting resistor $R = 10^2\text{--}10^5 \Omega$ in series with the sample, and has very poor response for measurements at $f > 1000 \text{ Hz}$. [The voltage drop across the smaller resistor $R' = 1\text{--}10 \Omega$ ($R \gg R'$) -also connected in

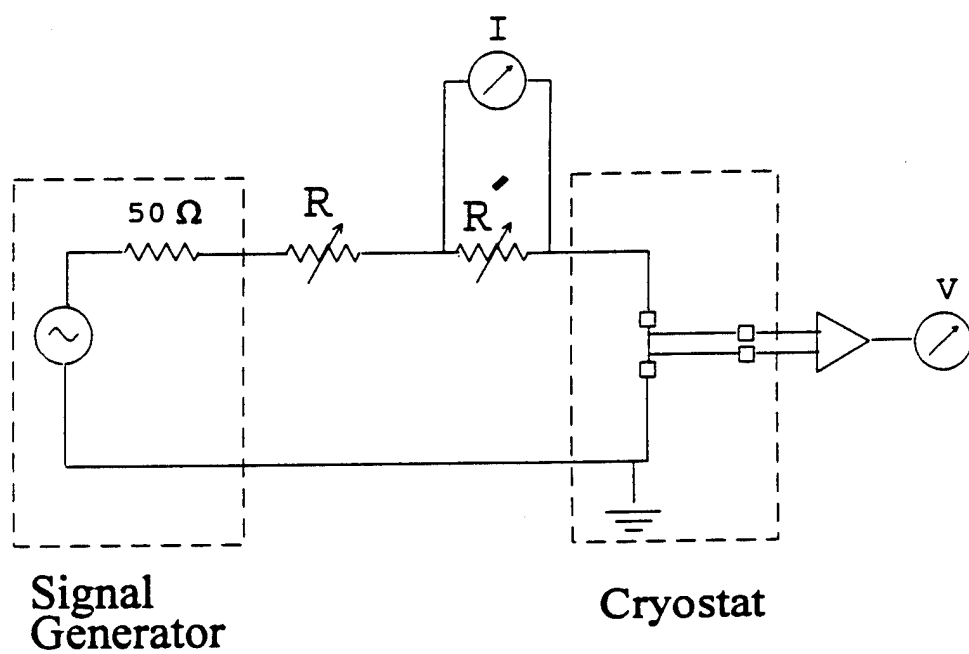
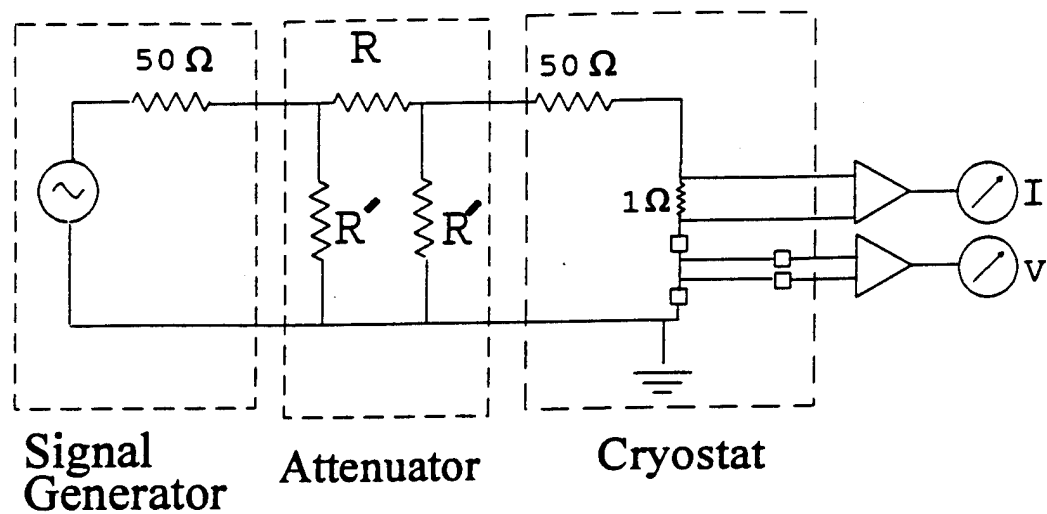


Figure 7. Two configurations for 4-terminal I-V measurements. Values of R , R' are given in the text.

series with the sample- indicates the current passing through the bridge]. Instead, the configuration in Fig. 7a has a $50\ \Omega$ resistor in series with the microbridge, located in the cryostat very close to the sample. Thus, the coaxial cable connecting the signal generator at room temperature to the sample (through a $50\ \Omega$ symmetric attenuator realized with the resistors R, R') is properly terminated when the film is in the superconducting state, which reassures the absence of unwanted end-reflections of the current at the sample up to frequencies in the MHz region. Moreover, we found that the $1\ \Omega$ resistor in series to the sample for measuring the current can be safely eliminated, simplifying the setup considerably: the current passing through the bridge can be calculated (to within $\pm 3\%$) by dividing the (attenuated) voltage from the signal generator by the two-terminal resistance of $50\ \Omega$. A note of caution: the configuration in Fig. 7a can be used only in the case when the temperature was close to T_c so that the magnitude of the 2-terminal (complex) sample impedance is much smaller than $50\ \Omega$ at the frequency of the measurement. Clearly, contact resistance in the order of $\sim 1\ \text{m}\Omega$ is desirable.

We now emphasize on the connection of the voltage pads (in the cryostat) to the instrumentation preamplifier (at room temperature). The sample is grounded at one end to the sample holder through a short wire. A single coaxial cable ($\sim 1.5\ \text{m}$ long, running parallel inside the probe to the one that carries the current) connects the voltage pads to a floating $50\ \Omega$ input of the preamplifier. [Alternatively, two coaxial cables were connected to the voltage pads, with their jackets shorted at the grounded end of the film, for a differential measurement. This configuration was rather

involved in that it required good matching of the two $50\ \Omega$ inputs of the preamplifier, and gave no improved results compared to the simpler cabling.] In order to properly terminate each of these cables *at both ends*, we could insert a $50\ \Omega$ resistor between its center conductor at the cryostat end and the voltage pad of the film. However, no significant improvement of the background signal of the setup is observed with such an addition. Finally, the preamplifier is based on the Signetics 592 chip and can be used with either single-ended or differential input. Using standard topology we achieved a 500 Hz - 22 MHz (-3dB) bandwidth with 30 dB gain. We found that one amplification stage suffices to provide the necessary isolation to the sample and dominate the mixer losses, at the high frequency measurements.

For measurements at frequencies 500 Hz -100 KHz, the lock-in is connected directly to the voltage leads. At 10-500 Hz, the rf preamplifier is substituted by a low noise commercial model (such as EG&G 113). Finally, at $f > 100$ KHz, the voltage signal is heterodyned to be detected from the lock-in, as it is shown in Fig. 8. Following the typical heterodyning scheme,⁵⁸ we mix both the amplified signal from the sample and the reference output of the signal oscillator with a clean sinusoidal signal from a separate local oscillator. The frequency of the two oscillators differs by Δf . The output of the IF port of each mixer is fed to a low-pass filter (with a final amplification stage) that provides the necessary $50\ \Omega$ termination for the mixers and attenuates the upper sidebands (of frequency higher than Δf). In most of our measurements, a personal computer controls both oscillators keeping $\Delta f = 5$ KHz. As expected from the broad bandwidth of the double-balanced mixers Synergy CLK-702B

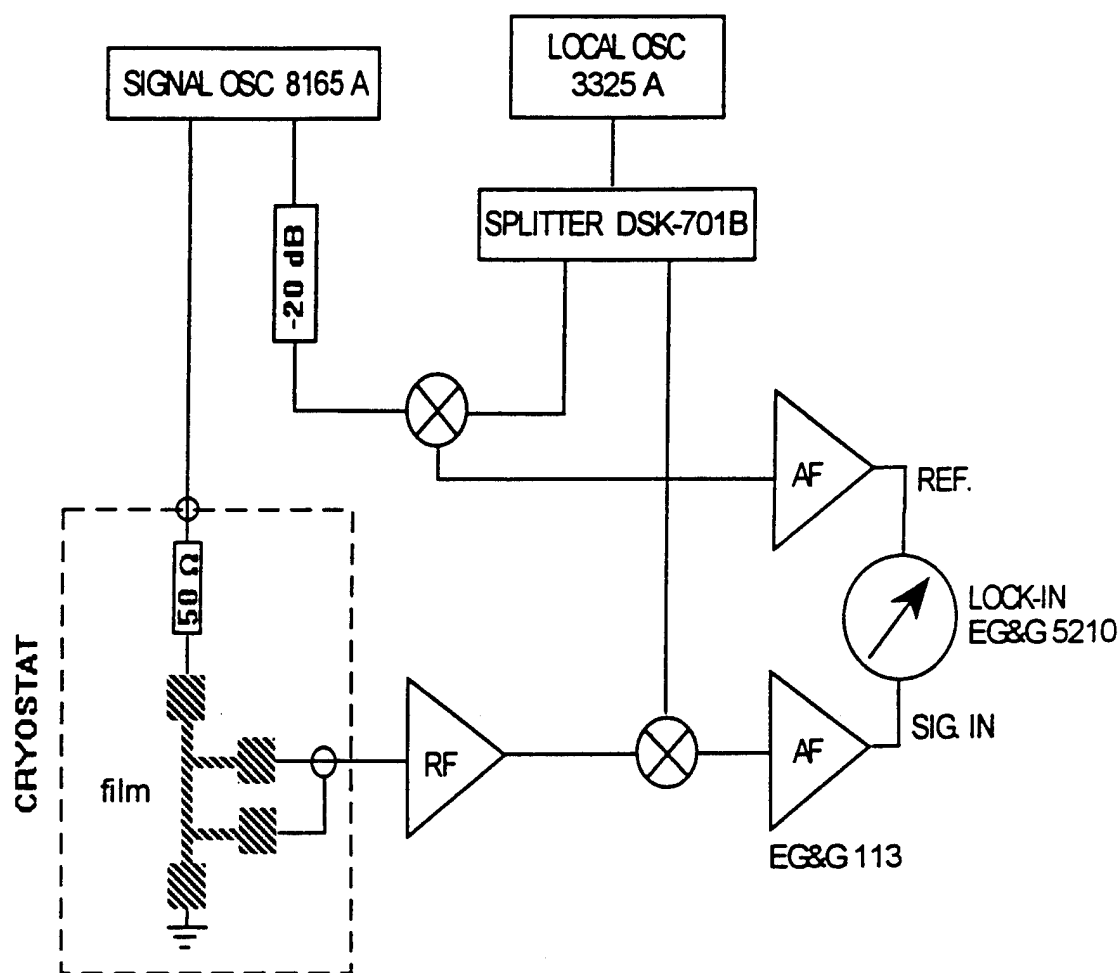


Figure 8. Heterodyning scheme used for dynamical measurements at frequency range 500 Hz-20 MHz.

(0.01-125 MHz at the RF/LO ports and *dc*-125 MHz in the IF port), variation of the frequency difference Δf from 1 to 50 KHz gives no detectable difference in our measurements. It only sets a lower limit for the frequency of the current passing through the sample, as heterodyning a signal of frequency f typically requires $f \gg \Delta f$.

In Fig. 9, we show the calibration of the apparatus. First, the bandwidth of our setup is determined by bypassing the sample and applying a *square wave* of known amplitude 1 mV directly to the input of the rf preamplifier. Its output was connected either directly to our EG&G lock-in for measurements at frequencies $f < 120$ KHz (open triangles) or according to the schematics of Fig. 7 for measurements at $f = 40$ KHz - 20 MHz (open squares). In the latter case, the rms value of the *sinusoidal signal* at frequency Δf measured by the lock-in, was converted to its amplitude value by multiplying it by $\sqrt{2}$. The -3 dB points are 500 Hz and 22 MHz, essentially the bandwidth of the rf preamplifier measured independently on a digital scope. The reason we calibrated the apparatus with a square signal and not a sinusoidal one is that the latter is -in general- deformed from a nonlinear current-voltage characteristic of the system, leading to a wrong estimation of the fundamental frequency when measured by the lock-in. On the other hand, a square wave remains square, even when it passes through a nonlinear element, and the ratio of the amplitude of the input to that of the output signal equals the ratio of their components at the fundamental frequency, even in the case of a nonlinear I-V. The impedance measurements that we will discuss in chapter IV are taken in a low current, so that

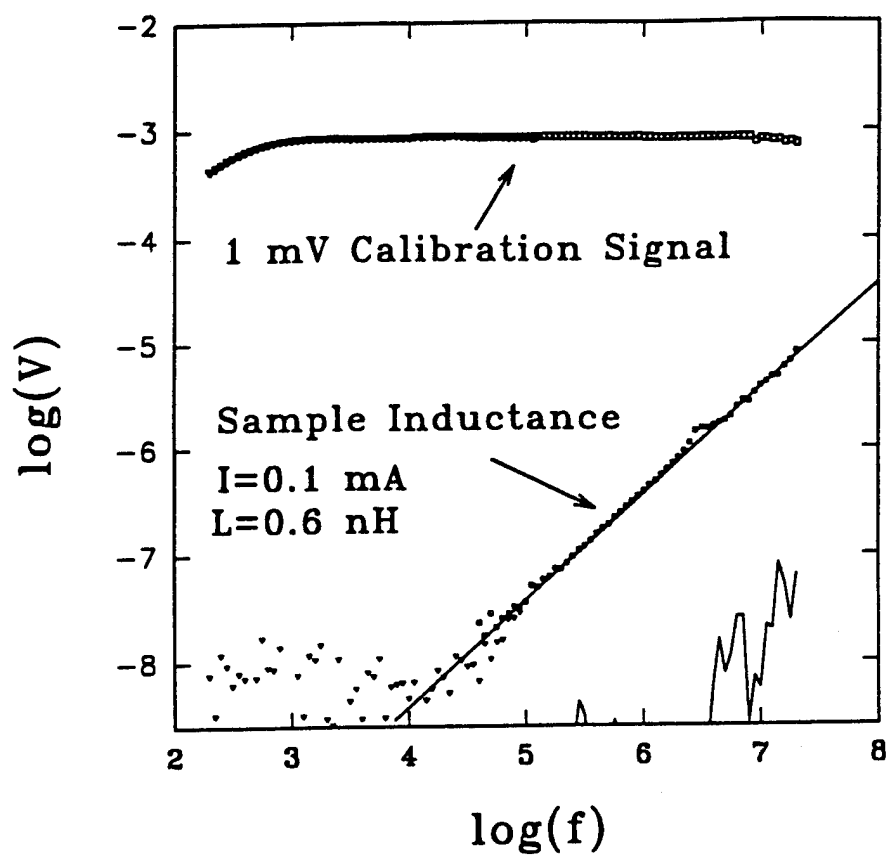


Figure 9. Calibration of the electronic setup with: 1 mV reference (top); inductive microbridge (middle); 50 Ω resistor at the rf preamp input (bottom).

square wave and sine wave signals give the same voltage at the fundamental frequency.

We then measured the inductive response of a $600\text{ }\mu\text{m} \times 50\text{ }\mu\text{m} \times 2000\text{ }\text{\AA}$ superconducting strip at temperature below the mean field transition at zero field. This particular film was made by laser ablation on LaAlO_3 substrate. It had zero-resistance transition temperature at 82 K and normal state resistivity of $160\text{ }\mu\Omega\text{ cm}$ at 100 K, indicating that this sample was probably oxygen deficient. In the superconducting state, the sample exhibited the expected purely inductive response: at $T=50\text{ K}$ and $I=10^{-4}\text{ A}$ square wave current applied, the amplitude of the signal was proportional to the frequency of the current I (Fig. 9), and the phase was $90 \pm 3^\circ$ relative to I . The magnitude of the measured inductance is in excellent agreement (within $\pm 10\%$) with the previously estimated geometrical inductance of the strip (see Eq. 12). The small deviation ($\pm 20\%$) from the linearity of the signal amplitude at $f > 3\text{ MHz}$ is caused by a background signal $\sim 10^{-7}\text{ V}$, which is very reproducible from day-to-day for the same sample (largely depending on the details of the cabling such as the impedance characteristics of the contacts on the film) and is independent of the current passing through the sample. The part of this background that is caused by our lock-in technique can be measured separately from the pick-up from the sample cabling, by setting a $50\text{ }\Omega$ resistor in the input of the rf preamplifier in the place of the voltage cable from the sample. The solid line in Fig. 9 indicates that this term rises above $3 \times 10^{-8}\text{ V}$ only for $f > 3\text{ MHz}$, with a bandwidth of $1/3\text{ Hz}$. This noise figure provides enough sensitivity to resolve changes in the inductive response of the

sample that correspond to a few nanovolts. It enabled us to measure the kinetic inductance of YBCO films in the presence of a magnetic field over a wide temperature and frequency range, which typically represents a few percent of the physical inductance. [The ratio between the two quantities at $B=0$ is $\lambda^2/dw \approx 1\%$, where λ is the magnetic penetration depth -typically 1500 Å at $T=0$ K diverging at T_c , and d and w are the thickness and the width of the strip, respectively].

We finish the discussion for our experimental setup with some comments for systems that have been previously used or are promising for improvement in the future. Several months after we constructed our apparatus, we learnt about a new 50 Ω lock-in (EG&G 5202). It covers the frequency range 0.1-50 MHz, thus it can substitute the mixer portion of our setup, probably providing a noise figure comparable to Fig. 9. Although at the moment (March 1993) this product is rather expensive (3-4 times) compared to our alternative, it is a clear sign that the market moves towards commercializing radio-frequency the radio-frequency phase sensitive detection.

Another possible improvement of our setup may be accomplished with a better video amplifier in the rf preamplification stage, in place of the Signetics 592. The only good choice available today could be the INA103 (1nV/ $\sqrt{\text{Hz}}$) from Burr-Brown, but with relatively similar bandwidth characteristics to the chip we used.

Last but not least, we should note that measurements of vortex dynamics in the resistive transition at high magnetic fields are subject to specific limitations of the detection instrument that couples to the superconducting sample. It became apparent

in the work of Olsson *et al*⁹, for instance, that, if standard cables have to be used with the detection instrument (lock-in amplifier or network analyzer), the size of the cryostat may be severely restricted, preventing the use of superconducting magnets. On the other hand, permanent magnets operating at room temperature typically reach magnetic fields $B \sim 0.5$ T, a value that is in the limit where dynamical phenomena from correlated vortices can be observed.⁹ Our setup avoids this difficulty, since it is not sensitive to the length of the semirigid $50\ \Omega$ cables connecting the film (cryostat) to the rf preamplification stage (at room temperature). Our sample was placed in a vacuum probe in the core of a 9 T superconducting magnet, where the temperature was regulated with stability better than 0.1 K. Our data of the kinetic inductance in Tesla fields below the glass transition are among the first in the literature.

CHAPTER III

STATICS

A. Universal characteristics at $T \geq T_c$

Is it possible to justify the existence of a phase transition in the vortex system in superconducting films through only transport measurements? It is fair to say that unambiguous proof for the phase transition can not be obtained. There are at least two reasons for this: First, the film geometry itself prohibits test the critical scaling predictions at temperatures very close to T_c , where the -diverging- vortex correlation length exceeds the thickness of the sample. Thus, conventional models¹¹ with sufficient adjustable parameters may provide at least semiquantitative fits to the transport data that claim to provide evidence for the transition²⁰. Second, the defect structure in the films that give rise to the phase transition is extremely complicated, so that different theoretical models for the transition (vortex glass or Bose-glass) could be relevant to the problem. The proper way to resolve this is for one to start with samples with no defects, and then introduce defects of a certain type (ex., either point defects by electron irradiation or columnar defects with ion bombardment) and study the properties of the transition. However, this can be done only on HTSC single crystals. The films, therefore, provide us with many challenges: Since we cannot

overlook their potential for technological applications we should carefully record the properties in their mixed state. We have to consider all the (sometimes circumstantial) evidence for the existence of the phase transition and see if they have universal character in many vortex pinning environments. We should finally determine ways to control the non-universal quantities in the mixed state in order to determine the appropriate theoretical model for the transition. The way the present work addresses these issues is by doping the YBCO films and by measuring the current-voltage characteristics at low frequencies ("statics") and the film impedance over a wide range of frequencies ("dynamics") associated with the magnitude of the vortex correlation time in the transition.

In this chapter we will show evidence for a phase boundary in the mixed state, drawn from current-voltage characteristics of $\text{YBa}_2(\text{Cu}_{1-x}\text{Al}_x)_3\text{O}_{7-\delta}$ films [$0 \leq x \leq 0.03$], in fields $0.5\text{T} \leq B \leq 6\text{T}$. The critical exponents and scaling functions of the transition are independent of Al concentration. Then, we will determine the characteristic length scale for vortex correlations that diverges at the transition temperature. We will also show that critical scaling persists over 60% of the resistive transition (which widens from 3 to 30 K as doping concentration and magnetic field increase) and breaks down when the correlation length decreases below 500-1250 Å, a value that *does not* depend on the intervortex spacing. Finally, we will discuss our results in the light of the phenomenological vortex-loop picture, and suggest that pinning in as-made pure and doped films of $\text{YBa}_2\text{Cu}_3\text{O}_{7-\delta}$ is dominated by extended rather than point defects.

The films that we report on in this chapter are made by co-deposition of Y, BaF₂, Cu, and Al, with an *ex situ* postanneal in oxygen.⁵⁶ They are 1000Å thick, single-phase, and highly oriented with the c-axis perpendicular to the substrate.⁵⁶ The zero-field transition temperature measured by *ac* susceptibility in these films is suppressed at only 1.2 K/at. % of Al, in accordance with the (thicker) films of Fig. 3, a relatively weak suppression compared to other dopants like Ni and Zn.^{56,60} As usual, the films are patterned for 4-wire measurements, with the strip between the two voltage leads now 100μm x 42μm. The normal state resistivity $\rho(T)$ is metallic, and $\rho(95\text{ K})$ increases from 110 μΩcm for undoped YBCO films to 150 and 200 μΩcm in the 2% and 3% Al doped films, respectively.

Fig. 10 shows I-V curves for the 2 at. % Al film at B=4T parallel to c-axis at temperatures evenly spaced by approximately 1 K from 54.0 to 73.4 K (all logarithms in this work are at base 10). These I-V's are typical of all films at all fields studied. Following standard procedure in the literature, we define the glass temperature, $T_g = 62 \pm 1\text{ K}$, to be the highest temperature at which the I-V fits to a single power law, within our voltage resolution (50 nV-1 mV). All I-Vs above T_g exhibit systematic upward curvature, thus restricting the uncertainty of T_g to $\pm 1\text{ K}$. Fig. 11 summarizes $T_g(B)$ [or, $B_g(T)$] for films with 0%, 2%, and 3% Al. Note that T_g for the 2% and 3% Al films is much lower than for undoped YBCO. Surprisingly, doping at this level weakens pinning and enhances flux wandering. However, as we will see below, it does not change the scaling functions and exponents of the transition.

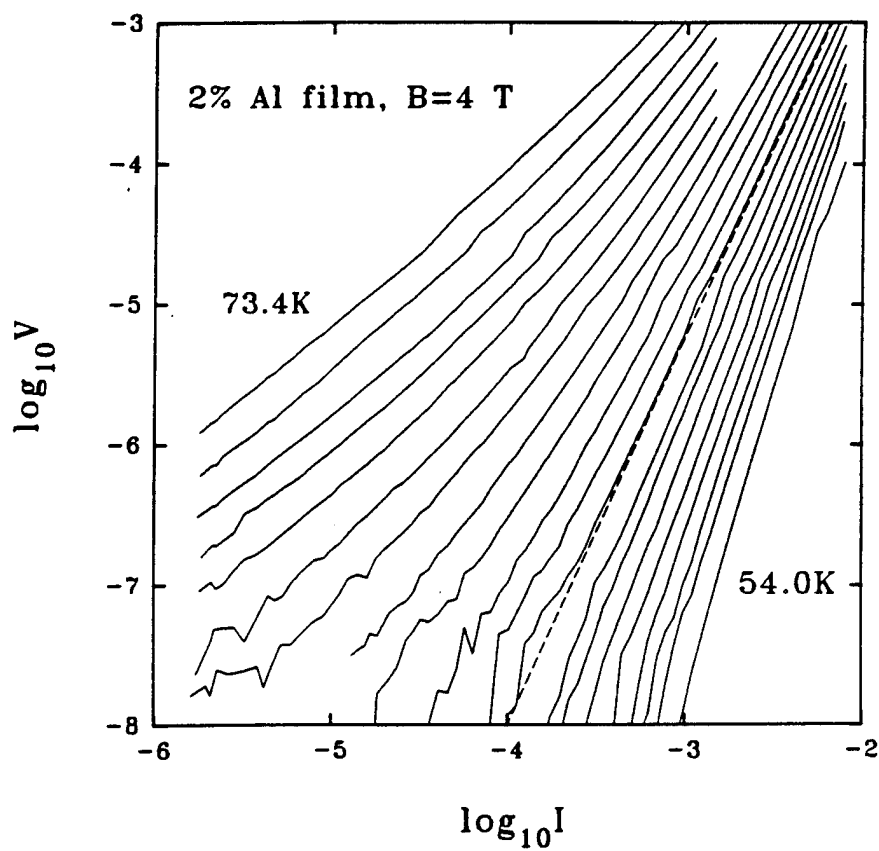


Figure 10. I-V curves on a 2 at. % Al film, at $B=4$ Tesla. The dashed line indicates the transition at $T_g = 62 \pm 1$ K. Curves are taken approximately 1 K apart.

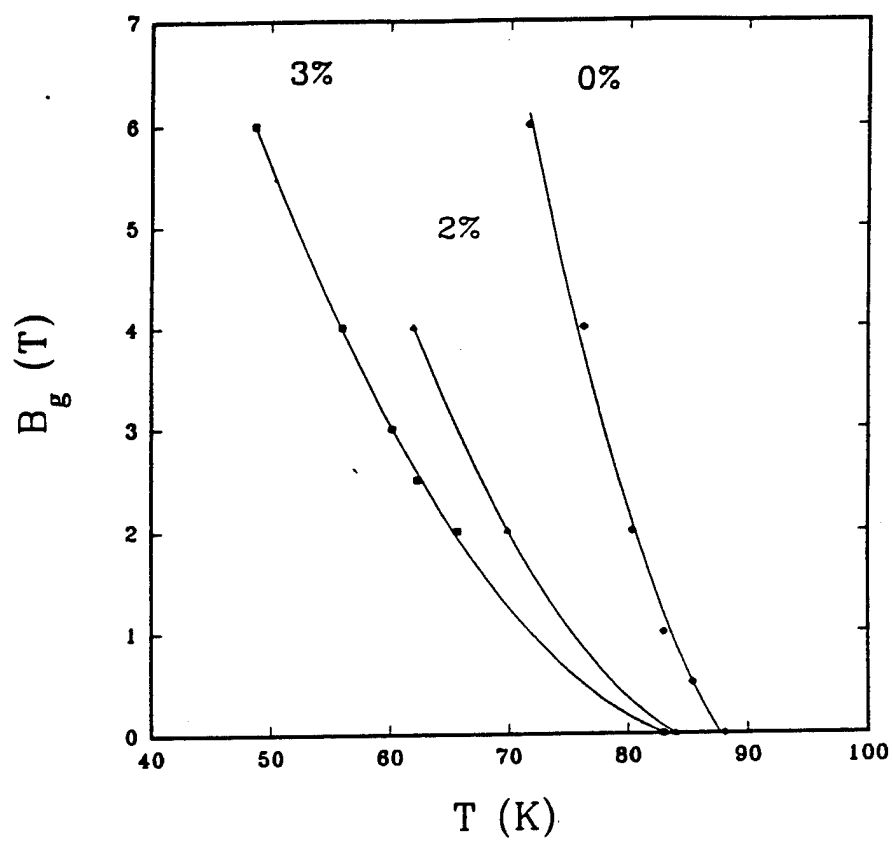


Figure 11. Glass phase boundary $B_g(T)$ for three samples of variable Al concentration.

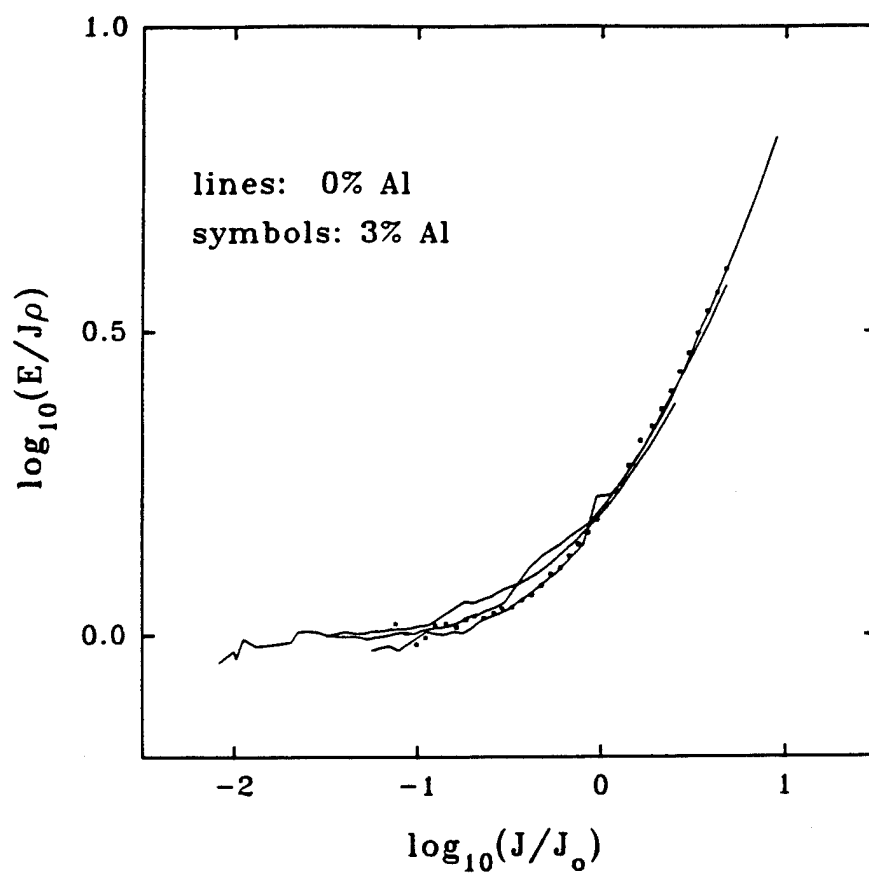


Figure 12. Scaling functions of a 3 at. % Al (dots) and a pure YBCO film (lines) at $B=4$ T.

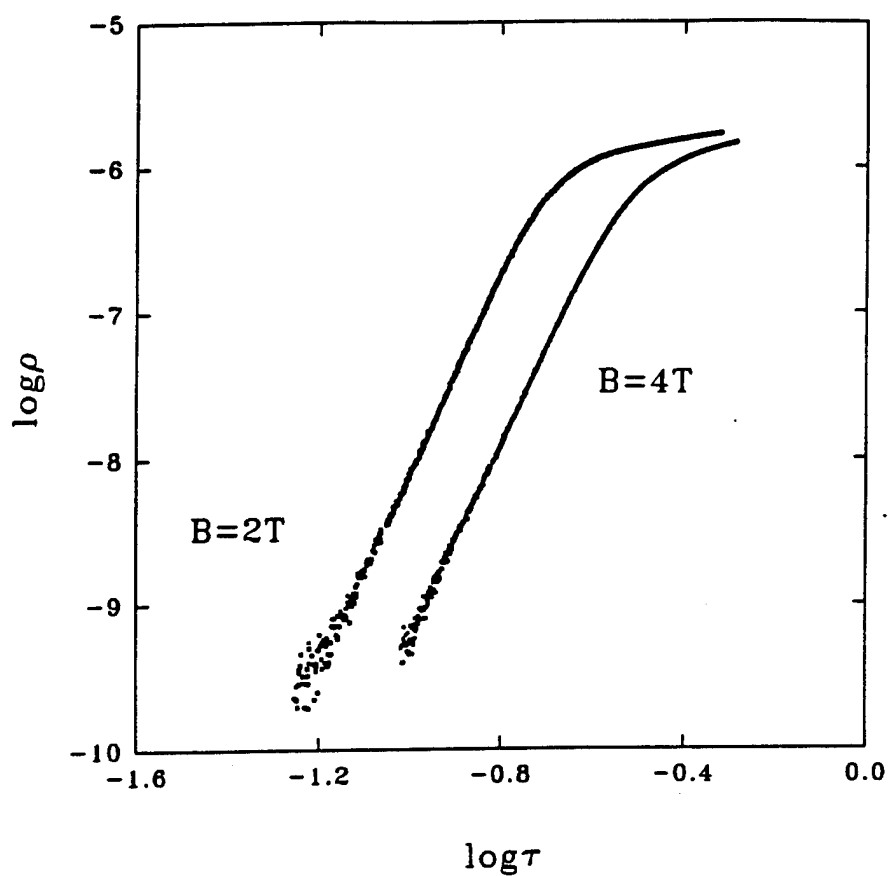


Figure 13. Low-current linear resistivity of a 3 at. % Al film at $B=2, 4T$. The data follow a power law $\rho \propto \tau^7 \equiv (T/T_g - 1)^7$ at low temperatures to within $\pm 1\%$.

In Fig. 12, we demonstrate how the I-Vs above T_g from different samples collapse on the same scaling curve. Here, we use the data from the 0% and 3% sample, at $B=4$ T. The two fitting parameters are the low-voltage linear resistivity $\rho(T)$, and the crossover current density $J_o^+(T)$ separating linear from nonlinear conductivity. We arbitrarily chose $J_o^+(T)$ to be the current density where $E/(J\rho)=1.5$. A different choice for would $J_o^+(T)$ would only move the lines parallel to the x-axis, but not affect the quality of the fit which is better than $\pm 5\%$.

The critical exponents of the transition are also independent of doping. The theory of vortex glass suggest ways to calculate z and ν from power laws extracted from the I-Vs. First, from Eq. 13 we see that, $V(T=T_g) \propto I^{(z+1)/2}$, given that the dimensionality of the problem is $D=3$. Thus, the slope of the I-V at $T=T_g$ (in a logarithmic plot) gives directly the critical exponent z . Second, the theory predicts $\rho \propto (T-T_g)^{\nu(z-1)}$ and $J_o^+ \propto (T-T_g)^{2\nu}$. In Fig. 13 we show typical resistivity data from the 3% film. Fitting the low-temperature dependence with the predicted law we extract the values of $\nu(z-1)$. Finally, the values of J_o^+ extracted from the fitting of the I-Vs on the universal scaling curve as in Fig. 12, lead to the estimation of 2ν . The fits of $V(T=T_g)$, $\rho(T)$ and $J_o^+(T)$ to the predicted power laws provide another self-consistent way to define T_g , that leads to the same value of T_g (within 2 K) with its operational definition from the curvature of the I-Vs. In Table 1 we show the values for the exponents $\nu(z-1)$ and 2ν , as well as $(z+1)/2$ from these fits, which are in excellent agreement with the values reported for YBCO films^{19,20} and twinned crystals²².

Theoretical models (other than vortex glass) would predict similar scaling laws with different expressions of the exponents in terms of ν and z . For example, we mentioned in the introduction the suggestions of the Bose-glass model, which is proposed for samples with columnar defects rather than microscopic disorder.²⁴ In any case, the fact that scaling occurs with the same exponents and scaling functions, even as the width of the resistive transition increases from 3 K to 30 K with increasing doping level and field, supports the existence of a phase transition at $T_g(B)$ and our use of appropriate models to interpret our data.

B. Nonuniversal characteristics at $T \geq T_g$

Despite the success of the models which embody the idea of a vortex phase transition to describe the scaling of the I-V curves, no consideration has been given to the interpretation of the nonuniversal parameters of the transition. These include the dependence of the phase boundary, the magnitude of the vortex correlation length and time, and the width of the transition where scaling laws hold, to fundamental quantities of the superconducting state such as the penetration and the coherence length, or the details of the pinning structure in films. In this section we address these issues.

We first comment on the reduction of T_g in the doped samples. For reference, our 2% film showed $T_g = 62 \pm 0.5$ K at $B = 4$ T, to be compared to $T_g = 76.3$ K for our undoped film and $T_g = 79.5$ K for a laser ablated film in ref. 19. No theoretical model predicts how the glass transition depends on materials parameters, with the

exception of the numerical simulations of Stroud and coworkers for the case of pure YBCO^{49,50}. In general though, several authors propose that T_g may lie inside the fluctuation region that is estimated from the "Ginzburg criterion".^{23,28,60} This criterion marks the point at which the system crosses over from mean-field to fluctuation-dominated critical behavior as T_C is approached from below. Then, from ref 23 (FFH), page 138 we get:

$$\Delta T_C/T_C = (\pi c_s \lambda_o \kappa / \gamma \Lambda_T)^2 \quad (17)$$

ΔT_C is the width of the fluctuation-dominated regime below the superconducting transition $T_C=85-90$ K, $\kappa=\lambda/\xi_{GL}\approx 100$ is the Ginzburg-Landau parameter, $\gamma=(m_{ab}/m_c)^{1/2}\approx 0.2$ the anisotropy parameter associated with different effective masses in the ab-planes and along the c-axis, $c_s\approx 0.4$ a constant predicted by rough theoretical estimations, and a thermal length $\Lambda_T\approx 2 \times 10^8/T_C$ Å. The zero-temperature penetration depth is $\lambda_o=1600\text{Å}$ and 2800Å in our pure YBCO and our 3% Al film respectively, measured by *ac*-susceptibility [E.R. Ulm *et al.* to be published]. Substituting in the above equation we find $\Delta T_C/T_C=0.15-0.20$ for pure YBCO, and therefore $T_g(B)$ lies inside the fluctuation-dominated regime for $B\leq 6T$. In 3% Al, ΔT_C is 3 times larger, *consistent with even the widest transition we see (30K at $B=6T$)*. The increase of λ_o is common in doped samples [also shown for Ni-doped YBCO: E.R. Ulm, Jin-Tae Kim and T.R. Lemberger, to be published in Physica B] and O-depleted YBCO samples [W.C. Lee and D.M. Ginsberg, *Phys. Rev. B* 44,

2815 (1991)].

Then, could one predict the magnitude of the reduction of T_g with doping given the increase in the penetration depth λ_0 due to doping? In general terms, there should be a "Lindeman criterion" relating T_g to parameters such as the vortex pinning energy, the Ginzburg-Landau coherence length, the penetration depth, etc. In particular, the energy gain per unit length from a vortex core pinned in a defect

$$\epsilon = \phi_0^2 / (64\pi^2 \lambda^2) \quad (18)$$

decreases by a factor of 3 with 3 at% doping, given that the zero-temperature λ_0 , as mentioned above, increases to 2800 Å relative to 1600 Å of pure YBCO. However, T_g decreases by only 20%. It is possible that Al introduces defects in the films that tend to *raise* T_g , like screw dislocations in the crystallites or edge dislocations in the grain boundaries. Such mechanism may dominate the reduction of ϵ at lower Al concentrations ($x < 0.01$) and consequently raise the T_g above its value in pure YBCO.

We are now ready to proceed beyond scaling arguments, to estimate the *magnitude* of the vortex correlation length $\xi_G(T)$ in a model-independent fashion. In particular, we are interested in estimating ξ_G at the temperature T^* where the scaling breaks down, and associating its value $\xi^* \equiv \xi_G(T^*)$ to some important mesoscopic length scale for vortex correlations. We define T^* as the temperature where $\rho(T)$ decreases 5% below the value predicted by the scaling power law $\rho \propto (T - T_g)^{(z-1)}$. To

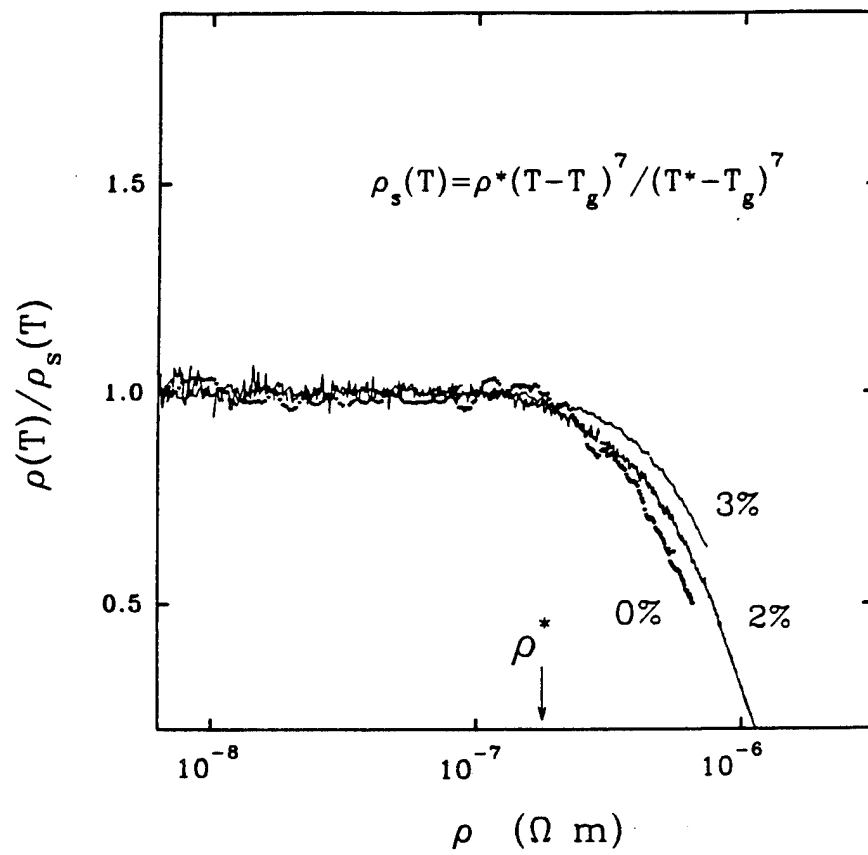


Figure 14. The linear resistivity deviates from critical power law at $\rho^*(T=T^*) = 22 \pm 5 \mu\Omega \text{ cm}$.

illustrate, Fig. 14 shows $\rho(T)/(T/T_c - 1)^{(z-1)}$ vs. $\rho(T)$ for the 3% Al doped film at $B = 2, 4$, and $6T$. Dividing out the strongest T -dependence of ρ emphasizes the deviation from the power law. The value of T^* and thus our conclusions are not particularly sensitive to our criterion of 5%, which determines T^* to ± 1 K. Interestingly, the critical scaling persists over $60 \pm 5\%$ of the width of the resistive transition, *i.e.*, $(T^* - T_c)/(T_c^B - T_c) \approx 0.60$, even though the width varies from 3 K to 30 K. Here, we take the onset of the resistive transition T_c^B to be where $\rho(T)$ in the applied magnetic field is about 75% of the extrapolated normal state resistivity. This corresponds to a suppression in the mean-field transition temperature of ~ 0.6 K/T, about the same as in pure YBCO. The significance of this "universal" behavior for T^* is unknown. From the applied point of view though, doped samples may thus be proved a useful tool in case a large critical temperature regime is required, as their broader resistive transitions correspond to wider critical regions.

We now estimate $\xi_G(T)$ using the crossover current density J_o^+ , which we define from the scaling forms as the current density J where $E/\rho J = 1.5$ (see Fig. 12). Since all I - V s in the critical regime collapse on the same scaling curve, other choices of this ratio between 1 and 3 do not affect our results. We use the conventional expression^{5,6}

$$J_o^+ \phi_o \xi_l \xi_{\perp} \approx kT \quad (19)$$

that does not depend on the particular model for the phase transition, to determine

$$\xi_0^2 \equiv \xi_{\parallel} \xi_{\perp} \quad (20)$$

Physically, this relation means that nonlinear behavior occurs when the current density is large enough to produce translations of correlated vortex segments of length ξ_{\parallel} over distance ξ_{\perp} perpendicular to the current, as readily as thermal fluctuations do. At $J < J_0^+$ translations of correlated segments are thermally induced, while at $J > J_0^+$, Lorentz-force-induced translations dominate. Since $J_0^+ \propto (T - T_g)^{2\nu}$, the size of vortex fluctuations diverges at T_g as $\xi_0^2 \sim (T - T_g)^{-2\nu}$, consistent with an increasing number of vortices becoming correlated and moving coherently as $T \rightarrow T_g$. To simplify the notation, we define $\tau \equiv (T/T_g - 1)$, $\tau^* \equiv (T^*/T_g - 1)$, and write

$$\xi_0 = \xi^* (\tau^*/\tau)^{\nu} \quad (21)$$

$$J_0^+ = \frac{kT}{\phi_0 \xi^{*2}} \left(\frac{\tau}{\tau^*} \right)^{2\nu}. \quad (22)$$

Fig. 15 shows $\xi_0^{-2} = J_0^+(T) \phi_0 / kT$ vs. τ/τ^* for a 3% Al film for $B = 2$ and 6T. The fact that the two data sets overlap means that both the magnitude and scaling law for $\xi_0(T)$ are independent of B , and hence independent of the average intervortex spacing. The intercept at $\tau/\tau^* = 1$ for this film yields $\xi^* = 515 \pm 40$ Å, which exceeds somewhat the intervortex spacing $a_v \equiv (\phi_0/B)^{1/2} \approx 190$ Å and 320 Å for $B = 6$ T and 2 T,

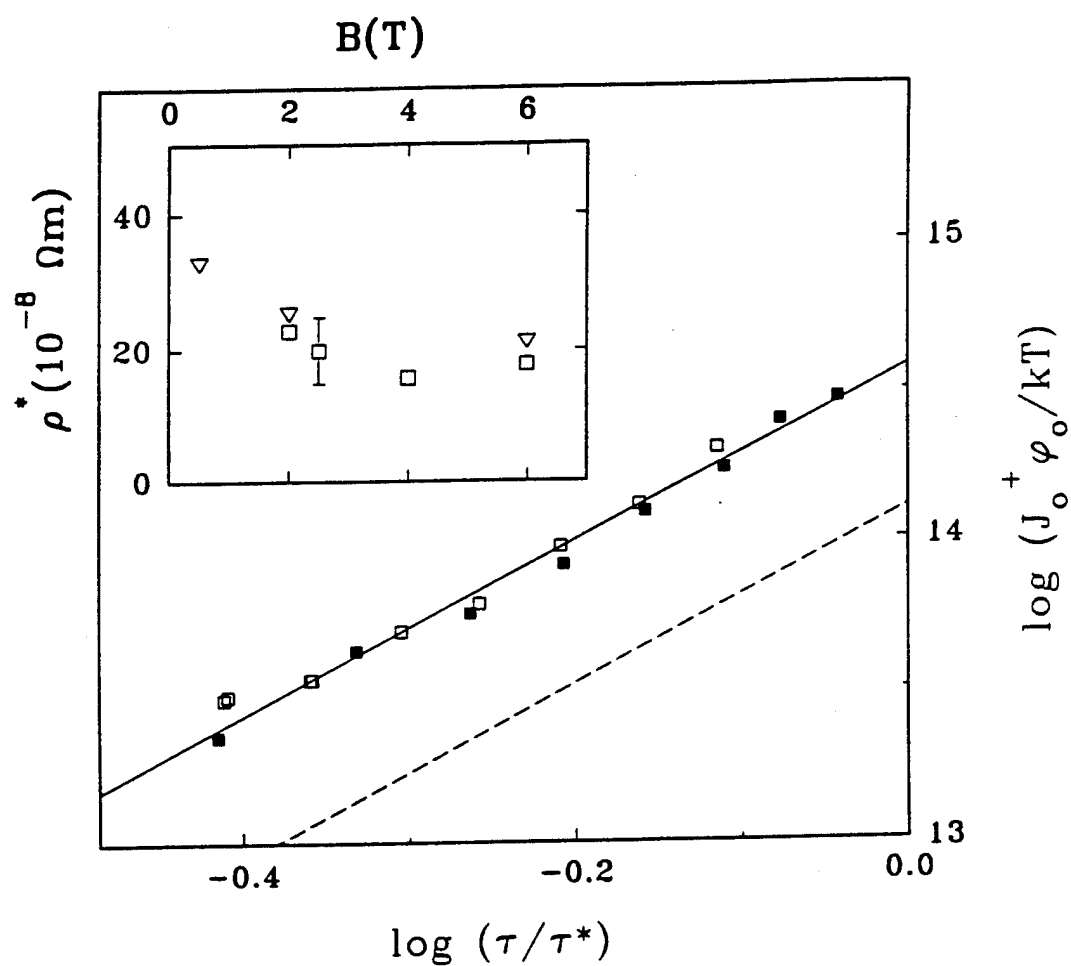


Figure 15. Data of a 3% Al film at $B=2, 6T$ fall on the same line $\xi_0^2 = (515\text{\AA})^2 (\tau/\tau^*)^{3.0}$. Inset: ρ^* vs. B for 0% (∇) and 3% Al (\square) films.

respectively. If ξ^* were proportional to a_{\perp} , then the 2 T data (filled symbols in Fig. 15) would fall on the dashed line. Taking into account the uncertainties of our estimation in T_g , T^* and the exponent $\nu(z-1)$, we find

$$\xi^* \propto B^{0 \pm .03}, \quad (23)$$

i.e., an extremely weak dependence of ξ^* on the applied field. This is the main result of this work and it holds for all the samples we studied, and for the laser ablated films of ref. 19 (see Fig. 16). Table 1 records the values of ξ^* obtained for each film. Al doping up to 3 at. % has only a small 15% effect on the magnitude of ξ^* . On the other hand, evidently film morphology affects ξ^* . In a 2500 Å-thick YBCO film with a sharp transition, we found $\xi^* = 1240 \pm 60$ Å. In an unusually resistive 2500 Å-thick YBCO film with a wider superconducting transition but the same scaling exponents we found $\xi^* = 730 \pm 40$ Å. Analyzing the measured $J_c^+(T)$ for $B = 2, 3$ and 4 T from Koch *et al.*¹⁹ on laser-ablated 4000 Å-thick YBCO films (Fig. 16), we find $\xi^* = 1100 \pm 200$ Å, independent of the magnetic field.

What is the significance of this result? First we consider the case that ξ^* strongly depends on the specifics of the behavior *above the transition* T^* . This is suggested by M. Salamon *et al.*,⁶¹ who note that T^* may mark the crossover between two regimes with different *scaling characteristics*. They propose that, in the temperature region centered on T_c and estimated by the Ginzburg criterion, a "3-D X-Y critical scaling model" describes the film conductivity. This argument is

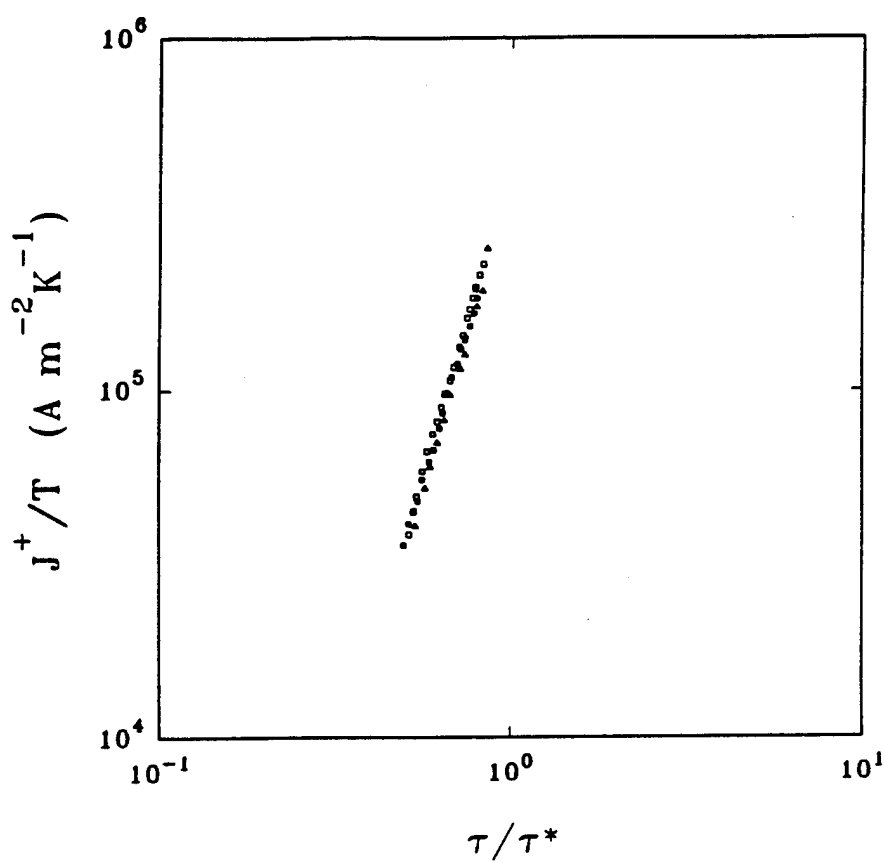


Figure 16. Measurements of ref. 19 analyzed according to Eq. 22. All data for $B=2, 3, 4T$ fall on the same line, leading to $\xi^* = 1100 \pm 200 \text{ \AA}$.

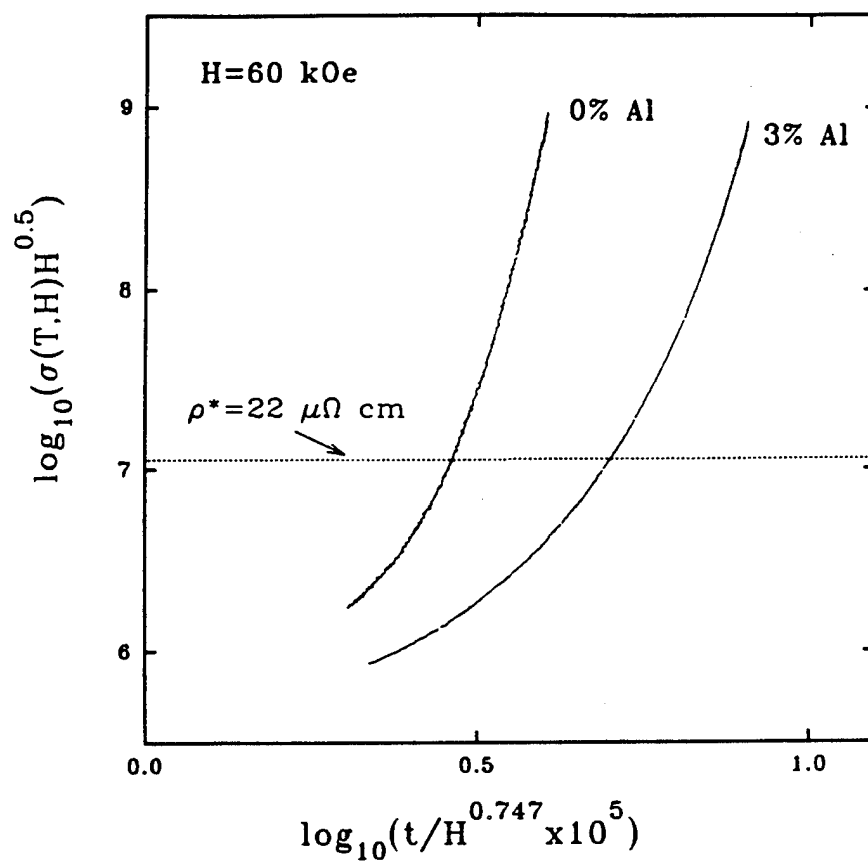


Figure 17. Scaled conductivity $\sigma(T,H)$ data according to X-Y model in ref. 61 from a pure and a 3 at. % Al film do not collapse onto a universal line. $t \equiv 1-T/T_C$

consistent with our observation that both boundaries $T^*(B)$ and $T_g(B)$ scale with field with the same power exponent (which in principle can be related to a 3-D critical exponent ν'):

$$(T_C - T^*) \propto (T_C - T_g) \propto H^{1/2\nu'}, \quad \nu' \approx 0.7 \quad (24)$$

However, an attempt to scale our $\rho(T)$ data in the vicinity of T to the expected form⁶¹

$$\sigma(T, H) H^{1/2} = s(\xi H^{1/2}) \quad (25)$$

[$H \approx B$, $\sigma = 1/\rho$ is the low-current ohmic conductivity, $\xi \propto (T_C - T)^{-\nu'}$ is the coherence length] leads to non-universal scaling functions $s[\xi(T)H^{1/2}]$, strongly dependent on dopant concentration. This is demonstrated in Fig. 17, where the left-hand-side of Eq. 25 is plotted against $t/H^{0.747} \equiv (1 - T/T_C)/H^{0.747} \propto [\xi(T)H^{1/2}]^{-1/\nu'}$. Even if we consider an increase of the magnitude of ξ to accommodate the broadening of the transition with doping, still the two curves would move relative to each other parallel to the x-axis of the plot, and they would not fall on the same scaling curve as Eq. 25 suggests. During my presentation in LT-20 conference, Dr. A. Koshelev mentioned that the failure of this particular model by Salamon *et al* could mean that the problem is considerably more complicated than is previously thought, rather than that the 3-D XY scaling model is completely inapplicable. Definitely, more theoretical work has to be done to clarify the issue.

We now approach the problem from the phenomenological point of view of the vortex loops, and consider the magnitude of ξ^* in terms of vortex correlations. In any model for the phase transition at T_c , the critical response must involve correlated motion of multiple vortices.⁶² Hence, the correlation length ξ_G (or at least ξ_L) should be larger than the average intervortex spacing in the critical region. Models in which pinning is from quenched disorder with an average spacing between pinning centers much smaller than the intervortex spacing lead to the conclusion that scaling should break down when the correlation length is roughly the intervortex spacing (a field dependent quantity). In the vortex glass theory in particular, the spatial extent ξ_G of phase coherence of the superconducting order parameter is assumed to exceed the range of translational order of the flux lattice. Thus, the critical scaling is expected to break down when ξ_G decreases below the Larkin-Ovchinnikov length²⁵, which is at most a few flux-lattice spacings.¹⁹ Again, ξ^* should be quite sensitive to B if a bundle of vortices are involved in the problem, and sensitive to T , as shown from Eq. 4 even in the case of a single vortex, in sharp contrast to our observations.

A natural interpretation of our result is that ξ^* reflects the underlying pinning structure in the films. Quite generally, models for critical scaling in samples where correlated disorder dominates pinning, require the transverse displacement ξ_L of liberated vortex segments to be at least the distance between neighboring macroscopic defects in the sample²⁴, and thus lead to a field independent value for ξ^* at the temperature where critical scaling breaks down. Equally probable sites for flux pinning in our films are grain boundaries, twin planes perpendicular to the substrate,

and columnar defects along the c-crystallographic axis. A typical grain size of 500 Å in YBCO films has been measured by TEM⁶², a value close to our ξ^* . Pinning in twin planes is also shown to dominate the regime above the T_c in twinned YBCO crystals.^{33,34} Finally, assuming that only columnar defects such as screw dislocations in crystallites or edge dislocations in grain boundaries are responsible for the pinning, a Bose-glass²⁴ calculation leads to a reasonable $d \approx 200$ Å for the distance between adjacent defects.⁵⁴ Although our experiment cannot decide for the nature of the extended defects responsible for the critical scaling, it suggests that their structure is dictated by the morphology of the substrate and/or misfits in the substrate-film interface rather than the dopant concentration, since Al doping has only a 15% effect on ξ^* . Furthermore, the variation of ξ^* with film thickness in undoped films suggests that sample defects change somewhat when the film thickness exceeds the typical grain size. It remains to be understood how Al doping weakens the pinning properties of the extended defects.

Below, we give the argument of the Bose-glass theory leading to the estimation of the distance between correlated defects mentioned in the previous paragraph, that was communicated to us by David Nelson. In ref. 24, Nelson and Vinokur show in detail how the correlation length ξ_1 relates to the distance d between columnar defects:

$$\xi_1 = d(T/T_{BG}^*)^2 \quad (26)$$

with $T_{BG}^* = 60$ K a characteristic temperature in the model, $\xi_{\parallel} = \xi_{\perp}^2/D_0$, where ξ_{\parallel} and ξ_{\perp} are the parallel and perpendicular to the field correlation lengths. $D_0 = 3 \times 10^{-6}$ cm is a diffusion length, suggestive of how far out from the applied field direction does a vortex segment deviate relative to its length ξ_{\parallel} . In our 2500 Å film we have $(\xi_{\parallel}\xi_{\perp})^{1/2} = 1250$ Å at $T = T^*$, and thus $d = 200$ Å. In our 1000 Å -thick films, $d = 250$ Å.

As a final point in the chapter, we discuss the striking result that the values of $\rho^* = \rho(T = T^*)$ are clustered around $22 \mu\Omega$ cm for all our samples and at all fields (inset in Fig. 15). Laser ablated films also show $\rho^* \approx 25 \mu\Omega$ cm at fields $B = 2-4$ T.¹ A sample-independent ρ^* sets a strong constraint for the magnitude of the vortex correlation length $\xi \propto (T - T_g)^{-\nu}$ and time $t \propto \xi^z$, with ν , z the static and dynamical critical exponent of the transition. In the framework of the vortex glass model, $\rho \propto (T - T_g)^{-(z-1)}$ and thus $\rho \propto \xi/t$. Therefore, at $T = T^*$, the ratio ξ/t is independent (similar to ρ) on the applied magnetic field, the width of the transition or the normal state resistivity of the sample. The magnitude of ξ and t can be measured independently by dc -^{54,55} and ac -⁵⁹ conductivity measurements respectively, and provide quantitative checks for the theoretical models that describe the critical response of the vortex system.

Although above we used a vortex-glass argument, the fact that the B -independent values of ρ^* , ξ^* set a strong constraint for the magnitude of the relaxation time $t = t^*(\xi_0/\xi)^z$, associated with the critical slowing down, is fairly robust. We estimate t^* by considering a vortex excitation of area ξ^2 , formed when current density

J_0^+ passes through the sample at temperature T^* . The energy gained in the system by the generation of the excitation is $J_0^+ \phi_0 \xi^2 \approx kT^*$. As this excitation relaxes, it dissipates energy at a rate $\int \mathbf{J} \cdot \mathbf{e} d^3x$, with \mathbf{J} and \mathbf{e} being the local current density and local electric field caused by the excitation, integrated over volume. Assuming that the integral is significant only at the core of the vortex of radius ξ_{GL} , and that

$$\mathbf{e} \approx \rho^* J_0^+ (a_v / \xi_{GL}) \quad (27)$$

is the macroscopic electric field $E \approx \rho^* J_0^+$ increased by the geometric factor a_v / ξ_{GL} , we obtain

$$\int \mathbf{J} \cdot \mathbf{e} d^3x \approx J_0^+ e \xi_{GL}^2 \xi^* \quad (28)$$

Letting t^* be the time for the fluctuation to dissipate its energy of kT , we find

$$t^* \approx (\xi^3 \phi_0^2) / (a_v \xi_{GL} kT^* \rho^*) \quad (29)$$

Olsson *et al.*¹⁵ find from the complex impedance of a 2500 Å-thick YBCO film at $B=0.55$ T that critical scaling persists for $t \geq 2 \times 10^{-8}$ s. Using values for ξ^* and ρ^* from our 2500 Å pure YBCO film, and $\xi_{GL} \approx 100$ Å at $T^*=88$ K, we estimate $t^* \approx 3 \times 10^{-8}$ s, in reasonable agreement with the experiment. As B increases and T^* moves away from $T_c(B)$, inflated values of ξ_{GL} are avoided and the system should become slower with $t^* \propto a_v^{-1}$. One should note however, that a different

phenomenological picture for the vortex excitations could lead to a new combination of the relevant length scales (including possibly an anisotropic ξ_a) in the estimation of t^* . The issue may be resolved by dynamical measurements in an extended region of magnetic fields and film thicknesses, and will be partially addressed in the following chapter. These measurements have the potential to estimate directly the relaxation time of the vortex excitations, which reflects the dynamics of the flux lines as they cross and recombine in the sample.

TABLE 1: Critical scaling parameters of $\text{YBa}_2(\text{Cu}_{1-x}\text{Al}_x)_3\text{O}_{7-\delta}$ films. The uncertainties represent possible systematic errors in the calculations.

% Al	thick (Å)	B (T)	$(z+1)/2$ (± 0.1)	$\nu(z-1)$ (± 0.4)	2ν (± 0.6)	ξ^* (± 40) Å
3	1000	6	3.0	7.1	2.8	521
3	1000	2	3.0	7.4	3.0	508
2	1000	4	2.8	6.7	3.6	462
2	1000	2	2.8	6.7	3.4	465
0	1000	6	2.8	7.1	3.2	441
0	1000	2	3.0	7.1	3.4	438
0	1000	0.5	3.1	7.2	3.2	439
0	2500	4	3.0	6.7	3.4	1240 ± 60
0*	4000	4	2.8	6.5	3.4	1100 ± 200

*Laser ablated film from ref. 20.

CHAPTER IV

DYNAMICS

A. Glass phase at $T < T_g$

In the previous chapter we examined the scaling characteristics in the vortex liquid state above the transition and identified the parameters that are universal and those which vary with doping. We now proceed to study the pinning characteristics of the glass vortex phase below T_g . Our goal is to determine experimentally the strength of the pinning force exerted on the vortices due to the sample disorder, so that a detailed description of the interaction between magnetic flux and defects can be achieved. Currently, there are two theoretical models that start from specific considerations about the sample disorder and lead to a melting transition: the collective pinning theory^{26,51}, which treats the flux lattice as an elastic medium in weak quenched disorder and concludes that a vortex glass phase exists at low temperatures, and the Bose-glass model²⁴ for vortices strongly pinned on correlated disorder, which leads to a Bose-glass vortex phase below T_g . Furthermore, recent numerical simulations that incorporate correlated disorder are also promising in calculating the vortex pinning strength and are consistent with flux melting at T_g .^{49,50} The physiognomy and the strength of the vortex pinning sites in the sample assumed in

these models are quite diverse and should be determined experimentally, so that a correct description for the observed phenomena be reached.

Direct observation of pinning effects can be obtained from the electrodynamic response of the samples, *i.e.*, the study of the complex response functions such as impedance and susceptibility.⁶⁴⁻⁶⁶ In particular, the *ac*-conductivity of the HTSC in the presence of *dc* magnetic field $B \parallel c$ has shown direct evidence for critical slowing down above the melting transition^{59,67}, and evidence for "intrinsic pinning", *i.e.*, pinning of a vortices on the *ab*-plane when the magnetic field is applied at small angles with the *ab*-crystallographic plane⁶⁸. In our work, we expand the technique to study the film inductive response at the temperatures below the onset of *dc* dissipation [at $T = T_g(B)$ estimated independently from current-voltage (*I-V*) curves]. For the first time we find a phenomenological relationship between the pinning strength of the vortices (those being macroscopic objects) in the glass phase and the inductive response of the supercurrents at zero field (which directly relates to the magnetic penetration depth, a fundamental superconducting parameter). Thus, we find that: 1) Each vortex in the sample feels the same pinning potential, 2) the effective restoring force constant due to pinning is inversely proportional to the square of the temperature-dependent of the magnetic penetration depth, and 3) the sample admittance drops to zero over a few degrees Kelvin in the vicinity of T_g , indicating that the sample disorder becomes ineffective to pin the flux lattice above that temperature. In addition, we find the *ac*-impedance of the sample in the vicinity of the melting temperature to be consistent with critical slowing down of the vortex

system. We discuss our results in the light of the different types of disorder that are present in the films.

The epitaxial YBCO thin film studied in this part of our work was deposited by pulsed laser ablation onto a heated SrTiO_3 substrate. The film was $d=2500\pm400$ Å thick, with its c-axis perpendicular to the film plane, and it exhibited a sharp transition (the 20%-80% transition width was less than 2 K). The zero-temperature penetration depth of the ab-planes was $\lambda(0)=1730\pm100$ Å measured with the 2-coil method, in good agreement with that of high quality crystals.⁶⁹ Following our established procedure, the film was patterned into a 4-contact microbridge of width $w=35$ μm and length $\ell=600$ μm by usual photolithographic techniques and wet etching in dilute nitric acid. The contacts were defined by ion milling (to clean the film surface) and subsequent Ag deposition (0.5 μm thick). The zero-resistance temperature of the film at $B=0$ was 88.5 K.

Measurements were taken in the transport microbridge using a square pulse current of amplitude I (much less than the critical current of the strip) and frequency $f=10^2 - 2\times10^6$ Hz and a lock-in to measure the amplitude of the signal V from the sample. The current was kept small compared to the critical current of the strip, so that the measured *ac*-voltage V was *linear in I at all temperatures of interest* (elastic limit⁶⁸). For frequencies $f=50$ KHz- 20 MHz, it was necessary to heterodyne the sample response into audio frequency in order to be detected by the lock-in, using the apparatus in chapter II. Special care has been taken to eliminate reflections in the transport lines from load mismatch by inserting 50 Ω resistors in series with the

sample (which is essentially a short, as its complex impedance never exceeds $10 \text{ m}\Omega$ in our measurements). In that way, we managed to reduce parasitic signals to a magnitude 2-10 times smaller than that from the physical inductance of the sample, throughout the frequency region this inductance was measurable, and at excitation currents as low as $\sim 30 \text{ }\mu\text{A}$.

In Fig. 18 we plot the magnitude $|Z_b|$ (*inset*: phase ϕ) of the impedance $Z_b \equiv (V/I)dw/\ell = |Z_b|e^{i\phi}$ measured accross the microbridge corrected by the geometrical factor dw/ℓ so that we can relate Z_b to microscopic sample parameters, as a function of magnetic field B applied parallel to the c -axis, at $f=1 \text{ MHz}$. The average current density $I/(dw)$ used in the measurement was $6 \times 10^6 \text{ Am}^{-2}$, *i.e.*, as low as 1-3 orders of magnitude smaller than the critical current. [The actual current density is expected to peak at the film edges, and this will be taken into consideration below.] From the figure we see that the bridge impedance Z_b can be separated into three components

$$Z_b = Z_p + Z_k + Z_v \quad (30)$$

with distinct physical meaning. First, a term

$$Z_p = \omega L_p(dw/\ell) \quad (31)$$

due to the magnetic flux coupled into the voltage circuit (dashed line), can be estimated to about $\pm 20\%$ accuracy from its geometrical dimensions (Eq. 17) as $L_p \approx$

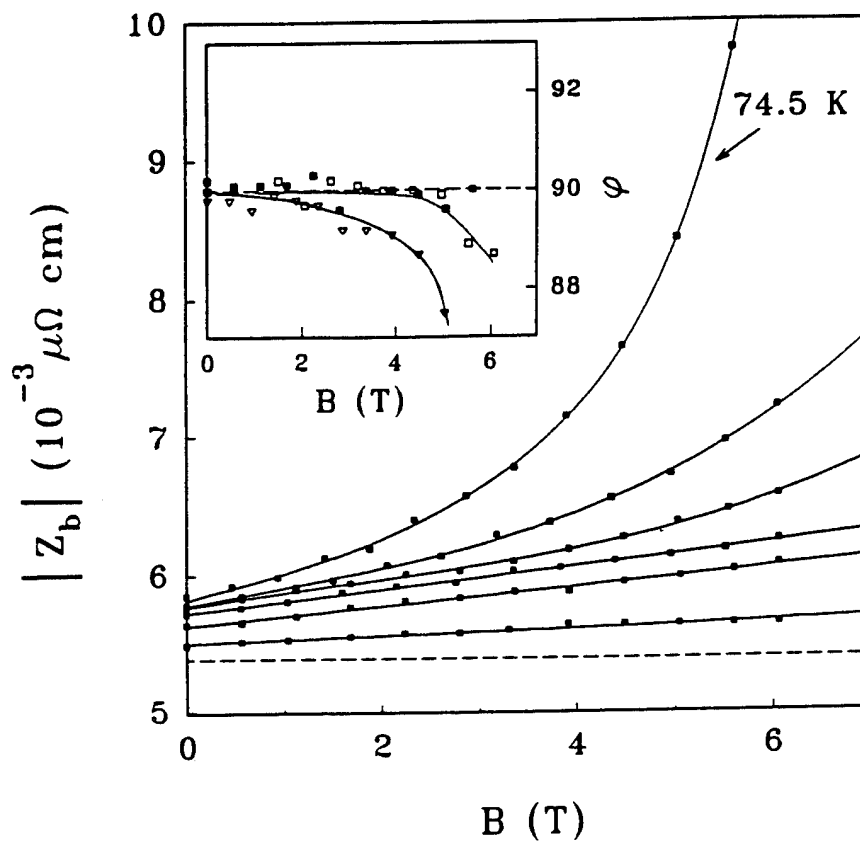


Figure 18. Raw data of the magnitude (inset: phase) of the impedance of the YBCO microbridge vs. B at $T=8, 54.2, 60.0, 65.2, 69.9, 74.5$ K (inset: $54.2, 69.9, 74.5$ K).

$\mu_0 l \approx 0.5-0.6$ nH. This term is treated as an adjustable parameter in our analysis, and it is important to consider its T- and B-dependence. Such dependences can arise from a change of the distribution of the current in the strip, which may alter the magnetic flux coupled between the voltage leads of the microbridge. This current distribution depends on the T-dependence magnetic penetration depth $\lambda(T)$ and the local vortex density in the film. However, $\lambda(T)$ changes by at most a factor of 2 in the temperature region below 80K where most of our data are taken, and the vortex density is reasonably uniform with an exception probably a distance comparable to the effective penetration depth $2\lambda^2/d$ from the film edges. A simple estimation of the flux coupled to the voltage leads shows that L_p does not change across the T- and B-range of our experiments by more than a few percent.

Given the above considerations regarding L_p , the y-intercept of the solid lines in fig. 18 represents the temperature dependent zero-field kinetic inductance

$$Z_k = \omega \mu_0 \lambda^2(T) \quad (32)$$

from the inertia of the superconducting carriers ($\omega = 2\pi f$ the angular frequency, and $\lambda(T)$ the magnetic penetration depth). Finally, the data at $B > 0$ indicate the effect of the driving current on the vortices. Driven by the Lorentz force $\mathbf{J} \times \mathbf{B}$, the flux quanta oscillate and give rise to a -generally- complex conductivity $\sigma_v = \sigma_{v1} + i\sigma_{v2} = 1/Z_v$. The data in Fig. 18 and its inset set a constraint for the real and imaginary part of the conductivity: in the region where $|Z_v| \propto 1/B$, the sample response is purely inductive

($\phi=90^\circ$ within our experimental error $\pm 0.4^\circ$). Conveniently expressing

$$\sigma_{v2} = 1/[\omega\mu_0\lambda_c^2(T,B)] \quad (33)$$

in terms of the phenomenological Campbell penetration depth $\lambda_c(T,B)$ in a notation similar to the form of the zero-field kinetic inductance, the above constraint suggests that, at temperatures where the signal is purely inductive $\lambda_c^2(T,B) \propto B$. This is the first important result of our dynamics measurements.

We now study the T-dependence of $\lambda_c(T,B)$ by comparing it with $\lambda(T)$. The data in Fig. 19 are taken at temperatures where the sample response is strictly inductive. Using a value of Z_p which is within 10% of our estimated value, the $B=0$ data lead to a magnetic penetration depth $\lambda = \lambda(0)/(1-T/T_C)^{1/2}$, where $\lambda(0)=1730 \text{ \AA}$ lies within the uncertainty of the value measured independently by *ac*-susceptibility in the same film before patterning. A change of our assumption for Z_p by $\pm 20\%$ does not affect the inferred T-dependence of $\lambda(T) \propto (1-T/T_C)^{-1/2}$ at $T > 60 \text{ K}$, and adjusts the x-intercept of the regressions in Fig. 19 (corresponding to T_C) by less than $\pm 1 \text{ K}$. At $B=1 \text{ T}$, the T-dependence of the signal remains the same, thus

$$(\lambda^2 + \lambda_c^2)^{-1} \propto (T_C - T) \quad (34)$$

Actually, because $\lambda^{-2}(T)$ has some downward curvature above 60 K, we expect the intercept of $\lambda^{-2}(T)$ to hit *above* the measured T_C . Combining the information from Eq.

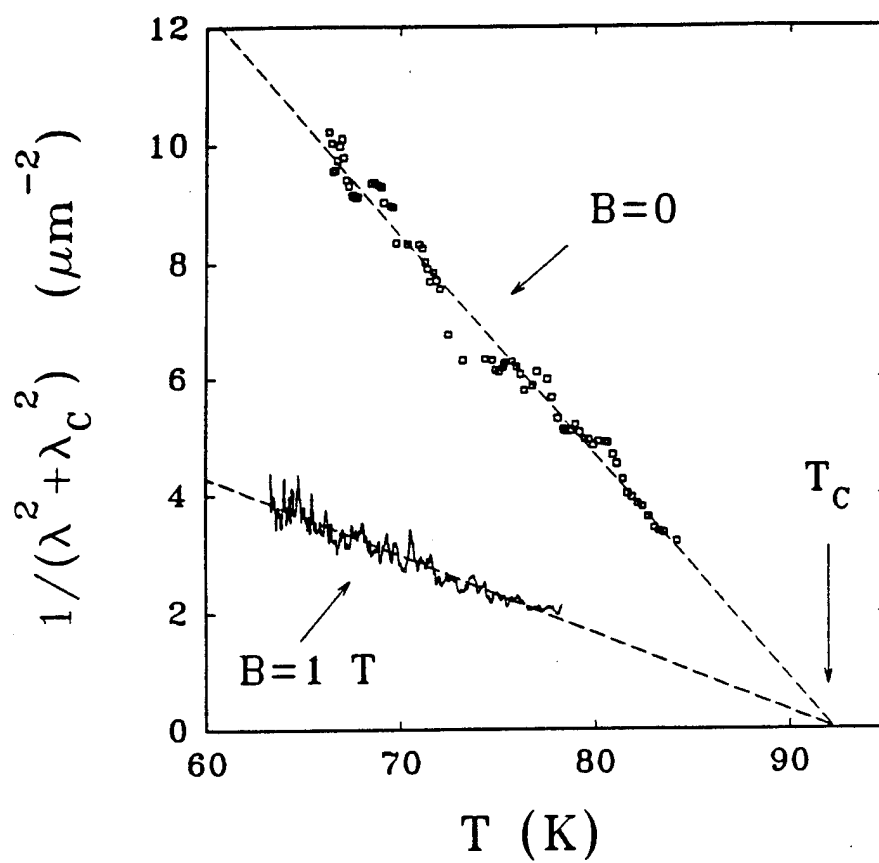


Figure 19. Temperature dependence of the purely inductive impedance plotted as $\omega\mu_0/(Z_0 - Z_p) \equiv 1/(\lambda^2 + \lambda_c^2)$ at $B=0$ and $B=1 \text{ T}$.

34 and our previous result $\lambda_c^2 \propto B$, we write

$$\lambda_c^2 = (B/B_0) \lambda^2 \quad (35)$$

with $B_0 = 0.48 \pm 0.05$ T. This means that the inductance of the vortices equals the kinetic inductance of the superconducting electrons at $B = 0.5$ T. In general, we find that a single value of B_0 describes all our data (*as long as* $\sigma_{v1} = 0$) for $0.5 \leq B \leq 6.5$ T, and up to our highest frequency $f = 20$ MHz. Furthermore, B_0 does not change in the presence of a *dc* current passing through the bridge, provided that it is less than the critical current. Finally, although we looked for it, we could not see any hysteresis in our field data whether B was increasing or decreasing, or its polarity was reversed. Using a time constant of 11 s in the lock-in, possible systematic deviations from Eq. (35) are within our experimental random error. Eq. (35) relates quantitatively the intrinsic magnetic penetration depth $\lambda(T)$ with a macroscopic quantity $\lambda_c(T)$ and is one of the central results of this work.

We analyze the T - and B -dependence of our data for $T < T_c$, in terms of the Labusch parameter α_L , which is the curvature of the pinning potential at its minimum.⁷³⁻⁷⁵ Driven by the Lorentz force, $F = \phi_0 J \sin \omega t$, each flux quantum ϕ_0 oscillates over distance $x = d_0 \sin \omega t$ giving rise to an inductive term in the measured complex impedance $\sigma_{v2}^{-1} = \omega B d_0 \cos \omega t$. Taking the phenomenological standpoint that each vortex oscillates under a restoring force per unit length $|F| = \alpha_L x$, and using $\sigma_{v2}^{-1} = \omega \mu_0 \lambda_c^2$, we find using Eq. 35

$$\lambda_c^2(T) = B\phi_0/(\mu_0\alpha_L). \quad (36)$$

$$\alpha_L = B_0\phi_0/(\mu_0\lambda^2). \quad (37)$$

Since, at any given temperature, α_L is observed to be constant for transport currents up to the critical current, the elastic limit ξ_d (*i.e.*, the width of the potential where our approximation for its quadratic form breaks down) is determined by the critical current density $J_c(T)$:

$$\xi_d = \phi_0 J_c(T)/\alpha_L(T) \quad (38)$$

Since both $J_c(T)$ and $\alpha_L(T)$ are approximately proportional to $T_c - T$ in the YBCO films, we find that ξ_d is in the order of 10 Å almost independent of temperature, *i.e.*, it is approximately the size of the vortex core in the sample. Given the form of α_L , the height of the pinning potential at ξ_d is in the order of 10 meV, a value much smaller than estimations for the potential barrier height derived from magnetic relaxation experiments in YBCO (typically 200 -300 meV).

Another important consequence of Eq. 31 is that it sets a semiquantitative limit in the range over which the strength of the pinning overcomes the intervortex interactions and thus destroys the translational order of the Abrikosov lattice in the YBCO film. We notice that

$$\alpha_L \approx 4\pi c_{66} \quad (39)$$

i.e., that the magnitude of the pinning restoring force constant α_L in the range of fields of our experiment is of the same order as

$$c_{66} = B\phi_0 / (4\pi\mu_0\lambda^2) \quad (40)$$

the *mean-field shear modulus of the triangular lattice*⁷⁶. This result indicates that the strength of pinning is comparable to the energy needed to shear the flux lattice, and is consistent with estimations from *dc* I-V curves at $T < T_g$ that the Larkin length in YBCO is only a few intervortex spacings.⁷⁷ Furthermore, the fact that the mismatch between the Labusch parameter and the shear modulus is temperature independent (both are proportional to $1/\lambda^2$) suggests that the range over which the flux lattice is ordered does not change with temperature at $T < T_g$, exactly as expected in a "frozen" vortex state.

By far, however, the most surprising result in this work is that α_L is field independent. This underlines that *each vortex is subjected to the same restoring pinning force*, rather than a distribution of pinning potentials. This fact excludes the possibility that vortices are pinned on isolated pinning sites, hierarchically filling the deepest potential wells first and then (as more vortices enter the sample by the increase of B) occupying weaker defect sites. It rather suggests that the number of pinning sites in the film greatly exceeds the number of vortices. Then, in the case

that pinning in correlated disorder dominates, one concludes that only macroscopic defects (as columnar defects) *of certain size* provide effective pinning. According to the work of Šášik and Stroud, the pinning strength of such sites resembles that of columnar defects of diameter 50 Å, where the superconducting order parameter is reduced by 10%. On the other hand, pinning due to microscopic disorder in the sample cannot be ruled out from our data. In this eventuality, each vortex core may rest on a large number of defects, thus averaging out their strength and leading to a Labusch parameter independent of the vortex density or the position of vortices in the film. In this case, the collective pinning theory should in principle describe our experimental form of α_L , the magnitude of which could be estimated considering either vortex-core pinning or magnetic pinning of the fluxons on the point defects.^{26,78}

B. Critical region at $T \approx T_c$

We now proceed to study the linear response of the vortices at temperatures and magnetic fields where the conductivity of the strip has a component in-phase with the excitation current ($\sigma_{v1} \neq 0$). In this region, the sample conductivity is frequency dependent, as is demonstrated in Fig. 20. There we show the reactance, $1/\sigma_{v2}(f, T)$, measured at an applied field $B=6$ T, after we subtracted the data taken at the same temperature but zero field. The straight lines represent fits $\sigma_{v2}^{-1} \propto f^\alpha$, with the exponent α determined without adjustable parameters from the slope in the logarithmic plot, and shown separately in Fig. 21a. Such power law behavior has been shown to

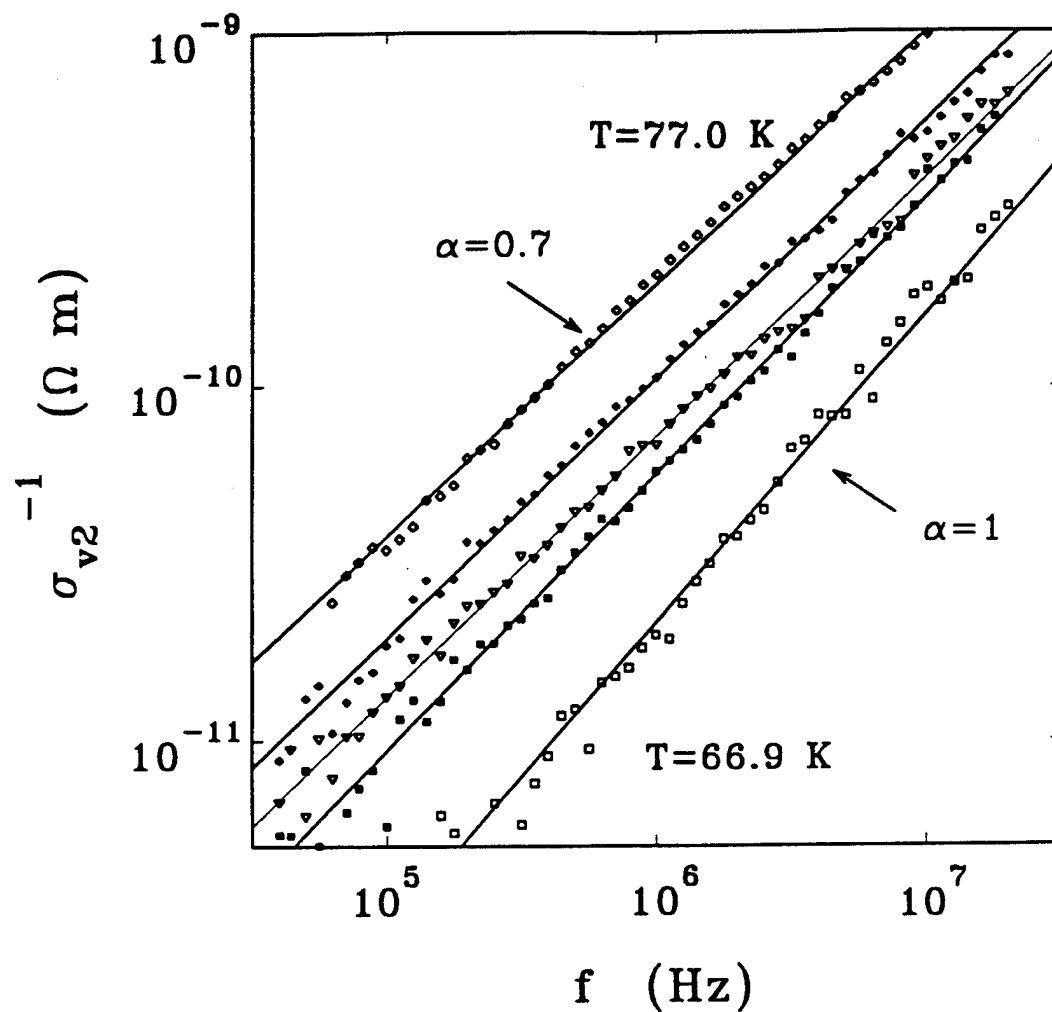


Figure 20. Logarithmic plot of σ_{v2}^{-1} vs. frequency, at temperatures 66.9, 74.6, 75.3, 75.9, and 77.0 K. The straight lines correspond to $\sigma_{v2}^{-1} \propto f^\alpha$.

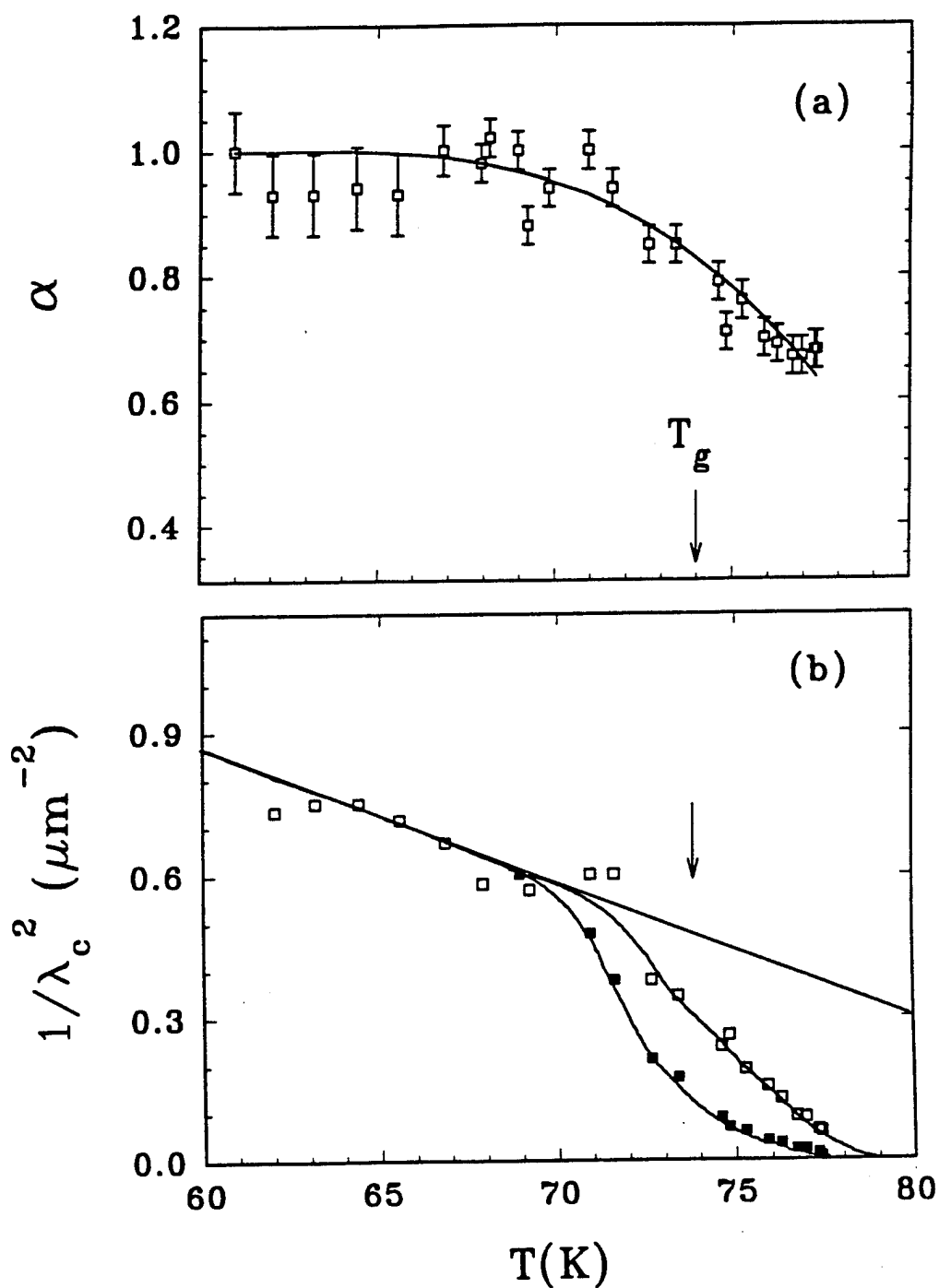


Figure 21. T-dependence of: (a) the exponent α , and (b) the $1/\lambda_c^2 \equiv \sigma_v \omega \mu_0$ at 10 MHz (open) and 100 KHz (filled symbols). The straight line is a fit with $B_0 = 0.44T$.

be consistent with the existence of a phase transition of the vortex system.⁶⁷

A reasonable question that arises is whether the observed scaling is quantitatively consistent with previous results. To check it, we took I-V curves at $f=100$ Hz (*dc* limit) and estimated the transition temperature $T_g(B=6T) = 73.7 \pm 0.7$ K as the lowest temperature with non-zero linear resistivity (using the analysis of Refs. 20, 22). Then, at $T=T_g$, Fig. 21a shows

$$\alpha = 0.82 \pm 0.04, \quad (41)$$

corresponding to vortex-glass dynamical critical exponent $z=6 \pm 1$. The same value of α is found from analysis of

$$\sigma_{v1}^{-1}(T=T_g) \propto \omega^{0.83 \pm 0.03}, \quad (42a)$$

$$1/(\sigma_{v1}^2 + \sigma_{v2}^2)^{0.5} \propto \omega^{0.83 \pm 0.04} \quad (\text{at } T=T_g). \quad (42b)$$

In addition, Fig. 22 shows that $\phi(T=T_g) = 72 \pm 4^\circ$, a value which is predicted directly from a Kramers-Kronig transformation of the power law in Eq. (29b).⁷⁰ This value is in excellent agreement with previous work on complex impedance measurements around T_g , and is consistent with critical scaling of the *dc* measurements (vortex glass dynamical critical exponent $z=6 \pm 1$). In Fig. 21b we go beyond scaling arguments to show a novel characteristic suggestive of a phase transition at T_g : a drop in the admittance $\omega\sigma_{v2}(T) = 1/(\mu_0\lambda_c^2)$, which becomes sharper

as frequency is reduced. At $T < T_g$, the sample inductance is nonzero (it follows Eq. (27)) and proportional to f (so that $\sigma_{v2}^{-1} \propto \omega$), thus the admittance is a *nonzero f -independent quantity*. On the contrary, at $T > T_g$, $\sigma_{v2}^{-1} \propto \omega^\alpha$ with $\alpha < 1$. Therefore, the admittance $\omega\sigma_{v2}$ drops to zero over a T -region that decreases as $\omega \rightarrow 0$.

Although Fig. 21b is suggestive of such trend, finite size effects do not allow the transition to become very narrow: analysis of *dc* I-V curves (as in chapter III) indicate that the vortex correlation length $\xi_c(T)$ at $B=6$ T exceeds the film thickness in a region of 3-4 K around the glass temperature T_g . Thus, the transition cannot be narrower than what is indicated in our Fig. 21b, even if we had enough resolution to take inductance data at lower frequencies.

What is the significance of this result? A drop in the film admittance at zero field in conventional superconductors has been correlated with a Kosterlitz-Thouless phase transition.^{71,72} In the presence of a net magnetic field, the film admittance is related to the perpendicular to the field component of the helicity modulus tensor by the form $\gamma_\perp \propto \omega\sigma_{v2}$, taken in the limit of zero frequency.⁵⁰ Thus, the drop in $\omega\sigma_{v2}$ from its frequency-independent finite value $\omega\sigma_{v2} = 1/(\mu_0\lambda_c^2)$ at $T < T_g$ to zero over a few degrees above T_g , indicates a sharp decrease of the superfluid density. This effect is recently predicted by Šášik and Stroud⁵⁰ using Monte Carlo simulations on disordered YBCO samples, and is a strong evidence of melting of the flux lattice at T_g .

Summarizing the work in this chapter, we have measured the field ($0.5 \leq B \leq 6.5$ T), temperature ($50 \leq T \leq 90$ K) and frequency ($50 \text{ KHz} \leq f \leq 20 \text{ MHz}$)

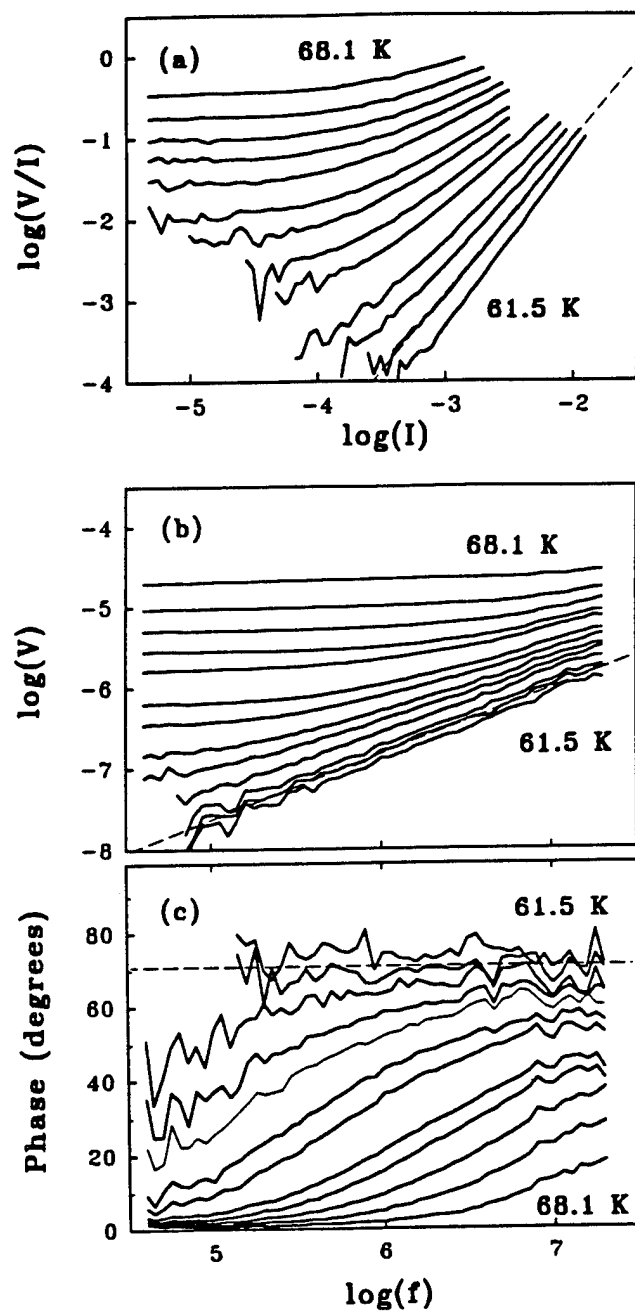


Figure 22. (a) I-V curves plotted as $\log(V/I)$ vs. $\log(I)$; f-dependence of the amplitude of V (b) and the phase of V/I (c), with $I = 40 \mu\text{A}$. Temperatures are approximately 0.6 K apart.

dependence of the complex conductivity of a YBCO microstrip. We found a drop in the admittance at $T \approx T_g$ (T_g was estimated independently from *dc* I-Vs). Scaling at T_g is consistent with the existence of a phase transition of the vortex system. At $T < T_g$, we extracted the restoring force that pins the flux in the sample. Finally, we estimated the elastic limit where a quadratic pinning potential well describes our dynamics data, and related it to the possible types of defects in the sample that may dominate the low-temperature elastic response of the flux lattice.

CHAPTER V

CONCLUSIONS

In this work we attempted a thorough study of vortex pinning effects as they are realized in statics and dynamical response of the flux lattice on transport currents. We proceeded in two directions: First, we tested the universality of phenomena that were previously observed in pure YBCO films, and are supposed to hold in a variety of high- T_C materials with similar defects in their crystal lattice. To this end, we used films with small concentration of Al substituting the Cu in the atomic cell. Second, we derived for the first time empirical laws that describe quantitatively the temperature dependence of the complex conductivity in the mixed state, related quantities in the superconducting transition as the transition width and the magnitude of the linear resistivity, and estimated the fundamental quantities such as the vortex correlation length and time.

In some of the issues, our data are strongly suggestive. For example, the question "are there true critical currents in high temperature superconductors?" is answered with a clear "yes": All our data are consistent with a phase transition at a temperature $T_g(B)$ from a vortex phase with linear dc resistivity to a glass phase where the flux lattice is effectively pinned in the sample disorder. In particular, we find that

the static nonlinear I-V characteristics obey power laws with critical exponents and scaling functions that are independent of doping (and thus independent of numerous quantities that characterize the films as transition width, normal state resistivity, London penetration depth etc.). For the first time we showed a drop in the sample admittance at the $T_c(B)$ that is defined from the I-V curves. Finally, the critical slowing down was directly observed in the frequency response of the *ac* conductivity at rf frequencies.

Parallel to clarifying the above issues, our data revealed a deep weakness of theoretical models to relate the measured quantities (resistivity, value of $T_c(B)$, etc.) to fundamental parameters in the superconducting state as the penetration depth, or to information on the microscopics of the disorder in the films. It is certainly quite true that an experimental work, such as the present one, is always allowed to stop at a phenomenological level of understanding of the phenomena at hand, attempting only to describe them in a self-consistent manner. However, such fact can hardly let the mind ease, at the prospect of a better arrangement of ideas that we are so certain that will come. In the meanwhile, what I will only add at the end of this manuscript is a table of the empirical formulas resulted through this work, as a monument -I hope- of my extreme dedication to the experimental detail that conducted my way.

Table 2. Summary of the phenomenological laws in this work.

	Empirical formulas	Prefactors
linear resistivity	$\rho = \rho^* \left(\frac{T - T_g}{T^* - T_g} \right)^{7.0 \pm 0.3}$	$\rho^* = 22 \pm 5 \mu\Omega\text{cm}$
correlation length ^a	$\xi_G = \xi^* \left(\frac{T^* - T_g}{T - T_g} \right)^{1.6 \pm 0.1}$	$\xi^* = 500 - 1250 \text{\AA}$
correlation time	$\tau = \tau^* \left(\frac{T^* - T_g}{T - T_g} \right)^{7.0 \pm 0.3}$	$\tau^* \sim 30 \text{ ns}$
Labusch parameter	$\alpha_L = B_0 \phi_0 / \mu_0 \lambda^2$	$B_0 = 0.48 \pm 0.05 \text{ T}$
transition width ^b	$T^* - T_g \approx 0.6 (T_C^B - T_g)$	-

^aThe value of ξ^* depends on the doping level and the film thickness, but is field independent.

^b T_C^B denotes the mean field transition temperature when field B is applied.

APPENDIX A

NONLINEAR MAGNETIZATION OF Y-B-C-O CRYSTALS

The early experimental work -late nineteen eighties- in YBCO run on two main themes: First, the need to record the novel character of these samples, especially at temperatures close to the mean field transition where the irreversibility line was identified. The result was a steady stream of publications from numerous laboratories that dealt with the peculiarities of the resistive transition, in addition to the question of the existence of true critical currents in the samples. Second, the effort to produce continuously improved samples in the form of single-phase powder, large monocrystals or thin films. Our lab quickly engaged in the effort in producing high-quality single crystals and films.

Following the successful fabrication of crystals with the desired sharp transitions, we developed a method to measure their magnetization in the presence of superimposed *ac* and *dc* magnetic fields in the order of a few Gauss. In particular, we focused on the harmonic content of the magnetization, which, in YBCO ceramics, has been shown to be surprisingly rich and had raised questions about the nature of the critical state in the high- T_C . To our surprise, we realized that a semiquantitative understanding of the phenomenon could be obtained by considering a toy-model for

the screening currents flowing in a resistive medium, where the resistance could be borrowed from available results from transport measurements. Our dynamics model was based on the observed "flux creep" resistance, in which the temperature T and the magnetic field B appear only in the ratio $(1-T/T_0)^{3/2}/B$. [The reader should refer for a detailed discussion of our results to ref. 79, which for technical reasons cannot be included in this manuscript.] Clearly, more complicated theories should have -at the very least- the same success in fitting the data, something that was not accomplished, as far as we know. It would be quite interesting for one to repeat these measurement in crystals with well characterized disorder (twin planes), which are available today, to confirm some of these early findings.

APPENDIX B

AC SUSCEPTIBILITY APPARATUS FOR MEASURING THE TRANSITION TEMPERATURE OF HIGH- T_c CRYSTALS, SINTERED SAMPLES, AND FILMS

The *ac* susceptibility technique is a reliable technique that can probe the onset of the diamagnetic response in a superconducting sample. As a non-contact technique, it is non-intrusive, allowing the sample under consideration to be used in subsequent measurements. Since it does not require a contingent superconducting path between two points where contacts are attached to the sample (as in a transport measurement), it can measure the superconducting volume of the sample and reveal the intergrain or intragrain origin of its diamagnetic response. Finally, by recording the transition width, it leads directly to information on the London penetration depth (when mGauss excitation magnetic fields are used) or the properties of the critical state.

The *ac* susceptibility method can be utilized by using 3 coils (one primary and two detection coils as in Appendix A), 2 coils (one excitation and one detection, as it is currently used in our lab to measure the penetration depth in films), or finally 1 coil in a tank circuit, as is described in this appendix.⁸⁰ Experimental details about the various methods of *ac* susceptibility can be found in ref. 81. Our setup, in

particular, serves as an extremely flexible device: in the past five years, it was used hundreds of times to characterize sub-millimeter-size crystals, thin films of area 1 cm², and sintered samples of various size used as targets in laser ablation and sputtering of YBCO films.

LIST OF REFERENCES

1. K. A. Muller, M. Takashige, and J. G. Bednorz, *Phys. Rev. Lett.* **58**, 1143 (1987).
2. A. P. Malozemoff, T. K. Worthington, Y. Yeshurun, and F. Holtzberg, *Phys. Rev. B* **38**, 7203 (1988), and references therein.
3. J. R. L. de Almeida and D. J. Thouless, *J. Phys. A* **11**, 983 (1978).
4. C. Ebner and D. Stroud, *Phys. Rev. B* **31**, 165 (1985).
5. Y. Yeshurun and A. P. Malozemoff, *Phys. Rev. Lett.* **60**, 2202 (1988).
6. T. T. M. Palstra, B. Batlogg, L. F. Schneemeyer, and J. V. Waszczak, *Phys. Rev. Lett.* **61**, 1662 (1988).
7. T. T. M. Palstra, B. Batlogg, R. B. van Dover, L. F. Schneemeyer, and J. V. Waszczak, *Appl. Phys. Lett.* **54**, 763 (1989).
8. M. Inui, P. B. Littlewood, and S. N. Coppersmith, *Phys. Rev. Lett.* **63**, 2421 (1989).
9. C. W. Hagen and R. Griessen, *Phys. Rev. Lett.* **62**, 2857 (1989).
10. C. W. Hagen, R. P. Griessen, and E. Salomons, *Physica C* **157**, 199 (1989).
11. R. Griessen, *Phys. Rev. Lett.* **64**, 1614 (1990).
12. P. W. Anderson, *Phys. Rev. Lett.* **9**, 309 (1962).
13. Y. B. Kim, *Rev. Mod. Phys.* **36**, 39 (1964).
14. M. R. Beasley, R. Labusch, and W. W. Webb, *Phys. Rev.* **181**, 682 (1969).
15. M. Tinkham, *Phys. Rev. Lett.* **61**, 1658 (1988).

16. V. Ambeogaokar and B. I. Halperin, Phys. Rev. Lett. **25**, 1364 (1969).
17. C. P. Bean, Phys. Rev. Lett. **8**, 309 (1962).
18. C. P. Bean, Rev Mod. Phys. **36**, 31 (1963).
19. R.H. Koch, V. Foglietti, W. J. Gallagher, G. Kogan, A. Gupta, and M. P. A. Fisher, Phys. Rev. Lett. **63**, 1511 (1989).
20. R. H. Koch, V. Foglietti, and M. P. A. Fisher, Phys. Rev. Lett. **64**, 2586 (1990).
21. M. P. A. Fisher, Phys. Rev. Lett. **62**, 1415 (1989).
22. P.L. Gammel, L.F. Schneemeyer, and D.J. Bishop, Phys. Rev. Lett. **66**, 953 (1990).
23. D.S. Fisher, M.P.A. Fisher, and D.A. Huse, Phys. Rev. B **43**, 130 (1991).
24. D.R. Nelson and V. M. Vinokur, Phys. Rev. Lett. **68**, 2398 (1992).
25. A.I. Larkin and Yu.N. Ovchinnikov, *J. Low Temp. Phys.* **34**, 409 (1979).
26. G. Blatter, M. V. Feigel'man, V. B. Geshkenbein, A. I. Larkin, and V. M. Vinokur, to be published in Rev. Mod. Phys.
27. M. Kardar and Y. -C. Zhang, Phys. Rev. Lett. **58**, 2087 (1987).
28. N.-C. Yeh , D. S. Reed, W. Jiang, U. Kriplani, F. Holtzberg, A. Gupta, B. D. Hunt, R. P. Vasquez, M. C. Foot, and L. Bajuk, Phys. Rev. B **45**, 5654 (1992).
29. N.-C. Yeh, D. S. Reed, W. Jiang, U. Kriplani, C. C. Tsuei, C. C. Tsi, and F. Holtzberg, Phys. Rev. Lett. **71**, 4043 (1993).
30. M. Charalambous, J. Chaussy, and P. Lejay, Phys. Rev. B **45**, 5091 (1992).
31. H. Safar, P. L. Gammel, D. A. Huse, D. J. Bishop, J. P. Rice, and D. M. Ginsberg, Phys. Rev. Lett. **69**, 824 (1992).
32. D. E. Ferrel, J. P. Rice, and D. M. Ginsberg, Phys. Rev. Lett. **67**, 1165 (1991).
33. W. K. Kwok, J. Fendrich, S. Fleshler, U. Welp, J. Downey, and G. W.

- Crabtree, Phys. Rev. Lett. **72**, 1088 (1994).
34. W. K. Kwok, J. Fendrich, U. Welp, S. Fleshler, J. Downey, and G. W. Crabtree, Phys. Rev. Lett. **72**, 1092 (1994).
35. H. Safar, P. L. Gammel, D. J. Bishop, W. C. Lee, J. Giapintzakis, D. M. Ginsberg, Phys. Rev. Lett. **70**, 3800 (1993).
36. T. K. Worthington, M. P. A. Fisher, D. A. Huse, J. Toner, A. D. Marwick, T. Zabel, C. A. Feild, and F. H. Holtzberg, Phys. Rev. B **46**, 11854 (1992).
37. E. H. Brandt, Proceedings of the NATO Advanced Study Institute, April 13-23, 1993, in Geilo, Norway: *Phase transitions and relaxation in systems with competing energy scales*; E. H. Brandt, Phys. Rev. Lett. **63**, 1106 (1989).
38. D. S. Fisher, Phys. Rev. B **22**, 1190 (1980).
39. D. R. Nelson, Phys. Rev. Lett. **60**, 1973 (1988).
40. D. R. Nelson and H. S. Seung, Phys. Rev. B **39**, 9153 (1989).
41. M. A. Moore, Phys. Rev. B **39**, 136 (1989).
42. W. K. Kwok, S. Fleshler, U. Welp, V. M. Vinokur, J. Downey, G. W. Crabtree, and M. M. Miller, Phys. Rev. Lett. **69**, 3370 (1992).
43. L. Civale, A. D. Marwick, T. K. Worthington, M. A. Kirk, J. R. Thompson, L. Krusin-Elbaum, Y. Sun, J. R. Clem, and F. Holtzberg, Phys. Rev. Lett. **67**, 648 (1991).
44. M. Konczykowski, F. Rullier-Albenique, E. R. Ycoby, A. Shalov, Y. Yeshurun, and P. Lejay, Phys. Rev. B **44**, 7167 (1991).
45. R. C. Budhani, M. Swenaga, and S. H. Liou, Phys. Rev. Lett. **69**, 3816 (1992).
46. D. R. Nelson, and V. M. Vinokur, Phys. Rev. B **48**, 13060 (1993).
47. T. Hwa, D. R. Nelson, and V. M. Vinokur, Phys. Rev. B **48**, 1167 (1993).
48. T. Hwa, P. Le Doussa, D. R. Nelson, V. M. Vinokur, to be published.
49. R. Šášík and D. Stroud, Phys. Rev. B **48**, 9938 (1993).

50. R. Šášik and D. Stroud, to be published in Physical Review Letters.
51. M.V. Feigel'man, V. B. Geshkenbein, A. I. Larkin, and V. M. Vinokur, Phys. Rev. Lett. **63**, 2303 (1989).
52. M. V. Feigel'man and V. M. Vinokur, Phys. Rev. B **41**, 8986 (1990).
53. V. M. Vinokur, P. H. Kes, and A. E. Koshelev, Physica C **168**, 29 (1990).
54. D.G. Xenikos, J.-T. Kim, and T.R. Lemberger, Phys. Rev. B **48**, 7742 (1993).
55. D.G. Xenikos and T.R. Lemberger, Physica B **194-196**, 1913 (1994).
56. J.-T. Kim, D.G. Xenikos, A. Thorns, and T.R. Lemberger, J. Appl. Phys. **72**, 803 (1992).
57. M. Honda, "The Impedance Measurement Handbook", Hewlett-Packard 1989.
58. J.R. Miller and J.M. Pierce, Rev. Sci. Instrum. **43**, 1721 (1972).
59. T.R. Chien, Z.Z. Wang, and N.P. Ong, Phys. Rev. Lett. **67**, 2088 (1991).
60. M.B. Salamon, Jing Shi, N. Overend, and M. A. Howson, Phys. Rev. B **47**, 5520 (1993).
61. Single vortex excitations of area $38 \times 92 \text{ \AA}^2$ are shown to characterize the depinning at low temperatures and fields: T.L. Hylton and M.R. Beasley, Phys. Rev. B **41**, 11669 (1990).
62. C.B. Eom, J. Z. Sun, B. M. Lairson, S. K. Streiffer, A. F. Marshall, K. Yamamoto, S. M. Anlage, J. C. Bravman, T. H. Geballe, S. S. Laderman, R. C. Taber, and R. D. Jacowitz, Physica C **171** (1990) 354-382.
63. A.M. Campbell and J.E. Evetts, Adv. Phys. **21**, 199 (1972).
64. A. M. Campbell, J. Phys. C **4**, 3186 (1971).
65. A. M. Campbell, J. Phys. C **2**, 1492 (1961).
66. H.K. Olsson, R. H. Koch, W. Eidelloth, and R. P. Robertazzi, Phys. Rev. Lett. **66**, 2661 (1991).
67. Hui Wu, N.P. Ong, and Y.Q. Li, Phys. Rev. Lett. **71**, 2642 (1993).

68. R.A. Doyle, A.M. Campbell, and R.E. Somekh, Phys. Rev. Lett. 71, 4241 (1993).
69. W.N. Hardy, D. A. Bonn, D. C. Morgan, Ruixing Liang, and Kuan Zhang, Phys. Rev. Lett. 70, 3999 (1993).
70. Alan T. Dorsey, Phys. Rev. B 43, 7575 (1991).
71. A.T. Fiory, A.F. Hebard, and W.I. Glaberson, Phys. Rev. B 28, 5075 (1983).
72. A. M. Kadin, K. Epstein, and A. M. Goldman, Phys. Rev. B 27, 6691 (1983).
73. J. R. Clem and M. W. Coffey, Phys. Rev. B 46, 14662 (1992).
74. M. W. Coffey and J. R. Clem, Phys. Rev. Lett. 67, 386 (1993).
75. R. Labusch, Crystal Lattice Defects 1, 1 (1969).
76. E. M. Brandt, J. Low Temp. Phys, 26, 735 (1977).
77. C. Dekker, W. Eidelloth, and R.H. Koch, Phys. Rev. Lett. 68, 3347 (1992).
78. C.J. van der Beek and P.H. Kes, Phys. Rev. B 43, 1303 (1991).
79. D. G. Xenikos and T. R. Lemberger, Phys. Rev. B 41, 869 (1990).
80. D. G. Xenikos and T. R. Lemberger, Rev. Sci. Instr. 60, 831 (1988).
81. R. B. Goldfarb, M. Leleental, and C. A. Thompson, in *Magnetic susceptibility of superconductors and other spin systems*, edited by R. A. Hein T. L. Frankavilla, and D. H. Liebenberg (Plenum Press, New York and London, 1992).

Approved for public release,
distribution unlimited

21-OCT 1993
SI PUB 0000

(AFSC)

Publications

Vortex correlations in the superconducting transition of $\text{YBa}_2(\text{Cu}_{1-x}\text{Al}_x)_3\text{O}_{7-\delta}$ films in high magnetic fields

Dimitrios G. Xenikos, Jin-Tae Kim, and Thomas R. Lemberger

Department of Physics, The Ohio State University, Columbus, Ohio 43210

(Received 28 May 1993)

We determine the characteristic length scale for vortex correlations in $\text{YBa}_2(\text{Cu}_{1-x}\text{Al}_x)_3\text{O}_{7-\delta}$ films [$0 \leq x \leq 0.03$] by studying their current-voltage characteristics in fields $0.5 \text{ T} \leq B \leq 6 \text{ T}$. We find that critical scaling persists over 60% of the resistive transition (which widens from 3 to 30 K as doping concentration and field increase) and breaks down when the correlation length is 500–1250 Å, a value that does not depend on the intervortex spacing. This result suggests that pinning in as-made films of $\text{YBa}_2\text{Cu}_3\text{O}_{7-\delta}$ is dominated by extended rather than microscopic defects.

Vortex pinning in disorder high-temperature superconductors has generated a number of different theoretical models, which deal with the static and dynamical characteristics of the mixed state and often introduce phases with qualitatively different correlations among the vortices. There is strong experimental evidence from current-voltage (I - V) curves in $\text{YBa}_2\text{Cu}_3\text{O}_{7-\delta}$ (YBCO) films¹ and twinned crystals² supporting the idea of a phase boundary associated with the “irreversibility line”³ in these materials. The details, though, of the pinning mechanism that gives rise to the critical behavior are still a matter of controversy. Fisher and co-workers^{4,5} model vortex behavior when vortex pinning is from microscopic quenched disorder, and they find a second-order phase transition separating a vortex-glass phase with vanishing linear resistivity from a vortex-fluid phase with a finite low-voltage resistivity. However, the nature of the phase transition may be quite different from that of the vortex-glass theory, if *correlated disorder* in extended defects is responsible for the flux pinning in these samples.⁶ Since both models are consistent with measured exponents and scaling functions for $V(I)$, one must look to nonuniversal parameters to distinguish them.

In this paper, we investigate the type of disorder that pins vortices in the glass state in high- T_c films by examining the length ξ_G associated with vortex correlations above the glass transition. We report that critical scaling persists over temperatures where the spatial extent ξ_G for phase correlations of the superconducting order parameter exceeds a length ξ^* (500–1250 Å) that *does not* depend on the intervortex separation. Such mesoscopic length scale is absent from models that assume pinning only in pointlike disorder, including the vortex-glass model. To investigate the generality of this result, we dope our YBCO films by substituting up to 3% of Cu with Al. This substitution leaves the critical exponents and scaling functions, theoretically universal quantities, unchanged, although it enhances thermal fluctuations and reduces $T_g(B)$. The length ξ^* is hardly affected by doping, and it is independent of the intervortex separation.

The films are made by co-deposition of Y, BaF_2 , Cu,

and Al, with an *ex situ* postanneal in oxygen.⁷ They are 1000-Å thick, single-phase, and highly oriented with the c axis perpendicular to the substrate.⁷ Doping suppresses the zero-field transition temperature measured by *ac* susceptibility at only 1.2 K/at. % of Al, a relatively weak suppression compared to other dopants like Ni and Zn.^{7,8} The films are patterned with standard photolithographic techniques for four-wire measurements, with the strip between the two voltage leads typically $100 \times 42 \mu\text{m}$. The normal state resistivity $\rho(T)$ is metallic, and $\rho(95 \text{ K})$ increases from $110 \mu\Omega \text{ cm}$ for undoped YBCO films to 150 and $200 \mu\Omega \text{ cm}$ in the 2% and 3% Al doped films, respectively. Scanning-electron microscopy (SEM) pictures show no evidence of misoriented grains in the surface topography. The most prominent defects we observe in the doped samples are holes about 1000 Å in diameter which occur in groups of 1–5 clustered about $1 \mu\text{m}$ apart. The clusters are typically $20 \mu\text{m}$ apart. These holes may arise from the collective release of fluorine gas from the films during postannealing. The similarity of our results with results on laser ablated films¹ without such defects indicates that they are not of fundamental importance here.

The inset in Fig. 1 shows I - V curves for the 2 at. % Al film at $B = 4 \text{ T}$ parallel to c axis at temperatures evenly spaced by 1 K from 54.3 to 73.3 K (all logarithms in this work are at base 10). These I - V 's are typical of all films at all fields studied. We define the glass temperature, $T_g = 62 \pm 1 \text{ K}$, to be the highest temperature at which the I - V fits (to $\pm 30\%$) to a single power law, within our voltage resolution (50 nV–1 mV). All I - V 's above T_g exhibit systematic upward curvature, thus restricting the uncertainty of T_g to $\pm 1 \text{ K}$. Figure 1 summarizes $T_g(B)$ [or, $B_g(T)$] for films with 0%, 2%, and 3% Al. Note that T_g for the 2% and 3% Al films is much lower than for undoped YBCO. Surprisingly, doping at this level weakens pinning and enhances flux wandering. It does not change the scaling functions and exponents of the transition. In the inset of Fig. 2, we demonstrate how the I - V 's above T_g from different samples collapse on the same scaling curve. The two fitting parameters are the low-voltage linear resistivity $\rho(T)$, and the crossover current density $J_0^+(T)$ separating linear from nonlinear conductivity.

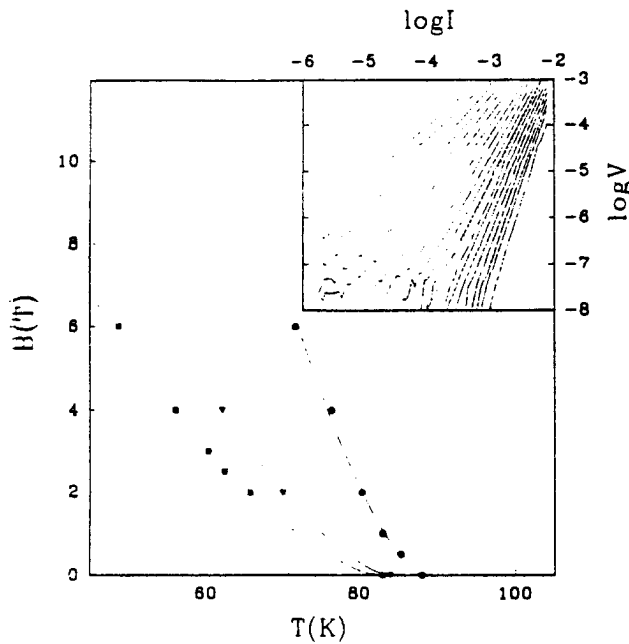


FIG. 1. Transition temperature T_g vs magnetic field, for pure YBCO (circles), 2% Al (triangles) and 3% Al doped films (squares). The solid lines are fits $B \sim (T_c - T_g)^{3/2}$, with T_c where $\rho = 0$ at $B = 0$. Inset: Typical I - V data (in mks units) for a 2% Al film at $B = 4$ T, from 73.3 to 64.3 K. The dashed line indicates the T_g at 62 ± 1 K.

We extract the critical exponents z and ν of the transition by fitting ρ and J_0^+ to the vortex-glass relations $\rho \propto (T - T_g)^{\nu(z-1)}$ and $J_0^+ \propto (T - T_g)^{2\nu}$. This provides another way to define T_g , that leads to the same value of T_g (within 2 K) with its operational definition from the I - V s. Table I shows values for the exponents $\nu(z-1)$ and 2ν , as well as $(z+1)/2$ from the slope of the I - V at T_g [$V \propto I^{(z+1)/2}$], which are in excellent agreement with values reported for YBCO films¹ and twinned crystals.² Theoretical models (other than vortex glass) would predict similar scaling laws with different expressions of the exponents in terms of ν and z .⁶ In any case, the fact that scaling occurs with the same exponents and scaling functions, even as the width of the resistive transition increases from 3 to 30 K with increasing doping and field, supports the existence of a phase transition at $T_g(B)$ and our use of appropriate models to interpret our data.

Beyond scaling arguments, it is possible to estimate the magnitude of the vortex correlation length $\xi_G(T)$ in a

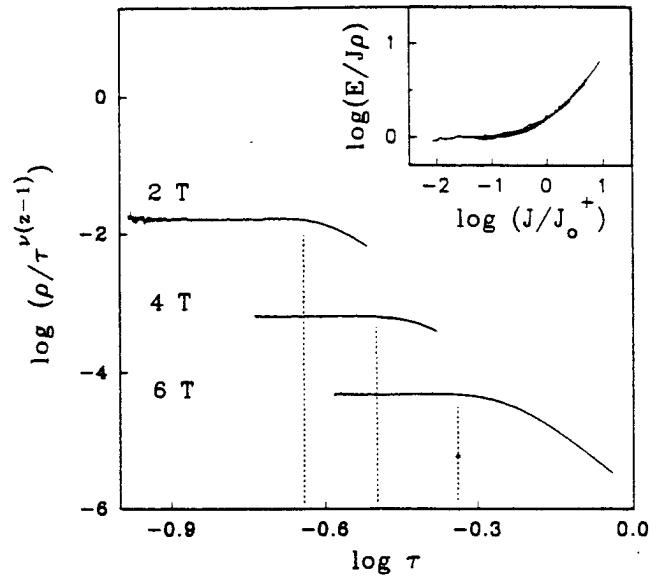


FIG. 2. Normalized resistivity (mks units) from a 3% Al film vs $\tau \equiv (T/T_g - 1)$ for $B = 2, 4$, and 6 T [with $\nu(z-1) = 7.4, 7.2$, and 7.1 respectively]. The dashed lines indicate τ^* which bounds the critical regime at high T . Inset: The scaling functions $E/J\rho$ vs J/J_0^+ for a 0% (lines) and a 3% (circles) film collapse on the same curve.

model-independent fashion. In particular, we are interested in estimating ξ_G at the temperature T^* where the scaling breaks down, and associate its value $\xi^* = \xi_G(T^*)$ to some important mesoscopic length scale for vortex correlations. We define T^* as the temperature where $\rho(T)$ decreases 5% below the value predicted by the scaling power law $\rho \propto (T - T_g)^{\nu(z-1)}$. To illustrate, Fig. 2 shows $\rho(T)/(T/T_g - 1)^{\nu(z-1)}$ vs $(T/T_g - 1)$ for the 3% Al doped film at $B = 2, 4$ and 6 T. Dividing out the strongest T dependence of ρ emphasizes the break at T^* . The value of T^* and thus our conclusions are not particularly sensitive to our criterion of 5%, which determines T^* to ± 1 K. Interestingly, the critical scaling persists over $60 \pm 5\%$ of the width of the resistive transition, even though the width varies from 3 to 30 K. Here, we take the onset of the resistive transition to be where $\rho(T)$ is about 75% of the extrapolated normal state resistivity. This corresponds to a suppression in the mean-field transition temperature of ~ 0.6 K/T, about the same as in pure YBCO. The significance of this "universal" behavior for T^* is unknown.

TABLE I. Critical scaling parameters of $\text{YBa}_2(\text{Cu}_{1-x}\text{Al}_x)_3\text{O}_{7-\delta}$ films. The uncertainties represent possible systematic errors in the calculations.

% Al	B (T)	$(z+1)/2$ (± 0.1)	$\nu(z-1)$ (± 0.4)	2ν (± 0.6)	ξ^* (± 40) Å
3	6	3.0	7.1	2.8	521
3	2	3.0	7.4	3.0	508
2	4	2.8	6.7	3.6	462
2	2	2.8	6.7	3.4	465
0	6	2.8	7.1	3.2	441
0	2	3.0	7.1	3.4	438
0	0.5	3.1	7.2	3.2	439

We now estimate $\xi_G(T)$ using the crossover current density J_0^+ , which we define from the scaling forms, as the current density J where $E/\rho J = 1.5$ (inset of Fig. 2). Since all I - V 's in the critical regime collapse on the same scaling curve, other choices of this ratio between 1 and 3 do not affect our results. We use the conventional expression^{5,6} $J_0^+ \phi_0 \xi_1 \xi_1 \approx kT$ that does not depend on the particular model for the phase transition, to determine $\xi_G^2 \equiv \xi_1 \xi_1$. Physically, this relation means that nonlinear behavior occurs when the current density is large enough to produce translations of correlated vortex segments of length ξ_1 over distance ξ_1 perpendicular to the current, as readily as thermal fluctuations do. At $J < J_0^+$ translations of correlated segments are thermally induced, while at $J > J_0^+$, Lorentz-force-induced translations dominate. Since $J_0^+ \propto (T - T_g)^{2\nu}$, the size of vortex fluctuations diverges at T_g as $\xi_G^2 \sim (T - T_g)^{-2\nu}$, consistent with an increasing number of vortices becoming correlated and moving coherently as $T \rightarrow T_g$. To clarify the notation, we define $\tau \equiv (T/T_g - 1)$ and write $\xi_G = \xi^*(\tau/\tau^*)^\nu$. Then,

$$J_0^+ \approx \frac{kT}{\phi_0 \xi^{*2}} \left(\frac{\tau}{\tau^*} \right)^{2\nu}.$$

Figure 3 shows $\xi_G^{-2} = J_0^+(T) \phi_0 / kT$ vs τ/τ^* for a 3% Al film for $B = 2$ and 6 T. The fact that the two data sets overlap means that both the magnitude and scaling law for $\xi_G(T)$ are independent of B , and hence the average intervortex spacing. The intercept at $\tau/\tau^* = 1$ for this film yields $\xi^* = 515 \pm 40$ Å, which exceeds somewhat the intervortex spacing $a_v \equiv (\phi_0/B)^{1/2} \approx 190$ Å and 320 Å for $B = 6$ T and 2 T, respectively. Taking into account the

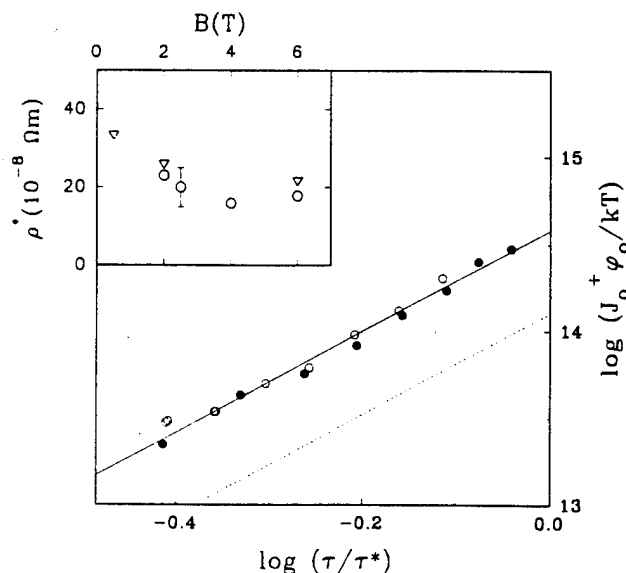


FIG. 3. Plot of $\xi_G^{-2} = (J_0^+ \phi_0 / kT)$ of a 3% Al film for $B = 2$ T (filled circles) and $B = 6$ T (open circles) vs τ/τ^* . The fit (solid line) corresponds to $\xi_G^2 = (515 \text{ Å})^2 (\tau/\tau^*)^{-3.0}$. If ξ^* were proportional to the intervortex spacing, then the 2 T data would fall on the dashed line. Inset: The resistivity $\rho(T = T^*)$ vs B for the undoped (triangles) and 3%-Al-doped film (circles). The uncertainty in ρ^* is indicated by the error bar in one data point. (All quantities in mks units.)

uncertainties of our estimation in T_g, T^* and the exponent $\nu(z-1)$, we find $\xi^* \propto B^{0 \pm 0.03}$, i.e., an extremely weak dependence of ξ^* on the applied field. This is the main result of this work and it holds for all the samples we studied, and for the laser ablated films of Ref. 1. Table I records the values of ξ^* obtained for each film. Al doping up to 3 at. % has a small 15% effect on the magnitude of ξ^* . Evidently film morphology affects ξ^* . In a 2500-Å-thick YBCO film with a sharp transition, we found $\xi^* = 1240 \pm 60$ Å. In an unusually resistive 2500-Å-thick YBCO film with a wider superconducting transition but the same scaling exponents we found $\xi^* = 732 \pm 40$ Å. Analyzing the measured $J_0^+(T)$ for $B = 2, 3$, and 4 T from Koch *et al.*¹ on laser-ablated 4000-Å-thick YBCO films, we find $\xi^* = 1100 \pm 200$ Å, independent of the magnetic field.

What is the significance of this result? First we consider the case that ξ^* strongly depends on the behavior at $T \geq T^*$, which is possible if T^* marks the crossover between two regimes with different scaling characteristics. A three-dimensional XY critical scaling model proposed⁹ to describe the conductivity around T_c is consistent with our observation that both boundaries $T^*(B)$ and $T_g(B)$ scale with field with the same XY-like exponent $[(T_c - T^*) \propto (T_c - T_g) \propto B^{1/2\nu}, \nu \approx 0.7]$. However, an attempt to scale our $\rho(T)$ data in the vicinity of T^* to the expected form⁹ $\sigma H^{1/2} = s(\xi_{GL} H^{1/2}) [H \approx B, \sigma = \text{ohmic conductivity}, \xi_{GL} \propto (T_c - T)^{-\nu} \text{ the coherence length}]$ leads to nonuniversal scaling functions $s(\xi_{GL} H^{1/2})$, strongly dependent on dopant concentration. This is true even if we consider an increase of the magnitude of ξ_{GL} to accommodate the broadening of the transition with doping.

We then consider the magnitude of ξ^* in terms of vortex correlations. In any model for the phase transition at T_g , the critical response must involve correlated motion of multiple vortices.¹⁰ Hence, the correlation length ξ_G (or at least ξ_1) should be larger than the average intervortex spacing in the critical region. Models, in which pinning is from quenched disorder with an average spacing between pinning centers much smaller than the intervortex spacing, lead to the conclusion that scaling should break down when the correlation length is roughly the intervortex spacing (a field-dependent quantity). In the vortex-glass theory in particular, the spatial extent of phase coherence of the superconducting order parameter ξ_G is assumed to exceed the range of translational order of the flux lattice. Thus, the critical scaling is expected to break down when ξ_G equals the Larkin-Ovchinnikov length,¹¹ which is at most a few flux-lattice spacings.⁵ Again, ξ^* should be quite sensitive to B and T , in sharp contrast to our observations.

A natural interpretation of our result is that ξ^* reflects the underlying pinning structure in the films. Quite generally, models for critical scaling in samples where correlated disorder dominates pinning, require the transverse displacement ξ_1 of liberated vortex segments to be at least the distance between neighboring macroscopic defects in the sample,⁶ and thus lead to a field-independent value for ξ^* at the temperature where critical scaling breaks down. Equally probable sites for flux pinning in our films

are grain boundaries, twin planes perpendicular to the substrate, and columnar defects along the *c*-crystallographic axis. A typical grain size of 500 Å in YBCO films has been measured by TEM,¹² a value close to our ξ^* . Pinning in twin planes is also shown to dominate the regime above the T_g in twinned YBCO crystals.¹³ Finally, assuming that only columnar defects such as screw dislocations in crystallites or edge dislocations in grain boundaries are responsible for the pinning, a Bose-glass⁶ calculation leads to a reasonable $d \approx 200$ Å for the distance between adjacent defects.¹⁴ Although our experiment cannot decide for the nature of the extended defects responsible for the critical scaling, it suggests that their structure is dictated by the morphology of the substrate and/or misfits in the substrate-film interface rather than the dopant concentration, since Al doping has only a 15% effect on ξ^* . Furthermore, the variation of ξ^* with film thickness in undoped films suggests that defects change somewhat when the film thickness exceeds the typical grain size. It remains to be understood how Al doping weakens the pinning properties of the extended defects.

As a final point, we discuss the striking result that the values of $\rho^* \equiv \rho(T=T^*)$ are clustered around $22 \mu\Omega \text{ cm}$ for all our samples and at all fields (inset in Fig. 3). Laser-ablated films also show $\rho^* \approx 25 \mu\Omega \text{ cm}$ at fields $B=2-4 \text{ T}$.¹ We can show that ρ^* and ξ^* set a strong constraint for the magnitude of the relaxation time $\tau = \tau^*(\xi_G/\xi^*)^2$ associated with the critical slowing down. We estimate τ^* by considering a vortex excitation of area ξ^{*2} , formed when current density J_0^+ passes through the sample at temperature T^* . The energy gained in the system by the generation of the excitation is $J_0^+ \phi_0 \xi^{*2} \approx kT^*$. As this excitation relaxes, it dissipates energy at a rate

$\int \mathbf{J} \cdot \mathbf{e} d^2x$, with \mathbf{J} and \mathbf{e} being the local current density and local electric field caused by the excitation, integrated over volume. Assuming that the integral is significant only at the core of the vortex of radius ξ_{GL} , and that $\mathbf{e} \approx \rho^* J_0^+ (a_y/\xi_{GL})$ is the macroscopic electric field $E \approx \rho^* J_0^+$ increased by the geometric factor a_y/ξ_{GL} , we obtain $\int \mathbf{J} \cdot \mathbf{e} d^2x \approx J_0^+ e \xi_{GL}^2 \xi^*$. Letting τ^* be the time for the fluctuation to dissipate its energy of kT , we find $\tau^* \approx (\xi^{*3} \phi_0^2)/(a_y \xi_{GL} kT^* \rho^*)$. Olsson *et al.*¹⁵ find from the complex impedance of a 2500-Å-thick YBCO film at $B=0.55 \text{ T}$ that critical scaling persists for $t \geq 2 \times 10^{-8} \text{ s}$. Using values for ξ^* and ρ^* from our 2500-Å pure YBCO film, and $\xi_{GL} \approx 100 \text{ Å}$ at $T^*=88 \text{ K}$, we estimate $\tau^* \approx 3 \times 10^{-8} \text{ s}$, in reasonable agreement with the experiment. As B increases and T^* moves away from $T_c(B)$, inflated values of ξ_{GL} are avoided and the system should become slower with $\tau^* \propto a_y^{-1}$. One should note however, that a different picture for the vortex excitations could lead to a new combination of the relevant length scales (including possibly an anisotropic ξ_G) in the estimation of τ^* . The issue may be resolved by dynamical measurements in an extended region of magnetic fields and film thicknesses. These measurements have the potential to estimate directly the relaxation time of the vortex excitations, which reflects the dynamics of the flux lines as they cross and recombine in the sample.

We are indebted to Eric Ulm for helping in the film fabrication stage, and to Saad Hebboul for many useful discussions. This work was supported primarily by Contract No. AFOSR-91-0188, with additional support for development of film fabrication from NSF-DMR88-22242 and DOE Grant No. DE-FG02-90ER4527 through the Midwest Superconductivity Consortium.

¹R. H. Koch *et al.*, Phys. Rev. Lett. **63**, 1511 (1989).

²P. L. Gammel, L. F. Schneemeyer, and D. J. Bishop, Phys. Rev. Lett. **66**, 953 (1990).

³A. P. Malozemoff, T. K. Worthington, Y. Yeshurun, and F. Holtzberg, Phys. Rev. B **38**, 7203 (1988), and references therein.

⁴M. P. A. Fisher, Phys. Rev. Lett. **62**, 1415 (1989).

⁵D. S. Fisher, M. P. A. Fisher, and D. A. Huse, Phys. Rev. B **43**, 130 (1991).

⁶D. R. Nelson and V. M. Vinokur, Phys. Rev. Lett. **68**, 2398 (1992).

⁷J.-T. Kim, D. G. Xenikos, A. Thorns, and T. R. Lemberger, J. Appl. Phys. **72**, 803 (1992).

⁸T. R. Chien, Z. Z. Wang, and N. P. Ong, Phys. Rev. Lett. **67**, 2088 (1991).

⁹M. B. Salamon *et al.*, Phys. Rev. B **47**, 5520 (1993).

¹⁰Single vortex excitations of area $38 \times 92 \text{ Å}^2$ are shown to characterize the depinning at low temperatures and fields: T. L. Hylton and M. R. Beasley, Phys. Rev. B **41**, 11 669 (1990).

¹¹A. I. Larkin and Yu. N. Ovchinnikov, J. Low Temp. Phys. **34**, 409 (1979).

¹²C. B. Eom *et al.*, Physica C **171**, 354 (1990).

¹³W. K. Kwok *et al.*, Phys. Rev. Lett. **69**, 3370 (1992).

¹⁴D. R. Nelson (private communication).

¹⁵H. K. Olsson, R. H. Koch, W. Eidelloth, and R. P. Robertazzi, Phys. Rev. Lett. **66**, 2661 (1991).

The effect of Al doping on the critical scaling of $\text{YBa}_2\text{Cu}_3\text{O}_7$ films, in high magnetic fields

Dimitrios G. Xenikos and Thomas R. Lemberger

Department of Physics, The Ohio State University, 174 West 18th Avenue, Columbus OH 43210, USA

We present current-voltage characteristics (I - V) in $\text{YBa}_2(\text{Cu}_{1-x}\text{Al}_x)_3\text{O}_7$ films ($0 \leq x \leq 0.03$), in magnetic fields $0.5 \leq B \leq 6$ T, which are consistent with the existence of a phase transition with critical exponents and scaling functions independent of Al concentration. We study the role of Al doping in flux pinning by analyzing the non-universal characteristics of the transition such as the width of the critical regime, the characteristic length for vortex correlations, and the temperature and the resistivity that correspond to the onset of the critical response.

1. INTRODUCTION

The nature of the disorder that pins the flux lines in high- T_c superconducting samples is still a controversial issue. One reason is that pinning of the vortex system manifests itself through a variety of novel static and dynamical characteristics, which are quite different in samples with varying degree of disorder - as in twinned and untwinned crystals,^{1,2} or films.³ In addition, it is shown theoretically that flux pinning in extended or point-like defects may lead to qualitatively different vortex phases.^{4,5} In this work we emphasize the *similarities* in the measured parameters in $\text{YBa}_2\text{Cu}_3\text{O}_7$ (YBCO) films, where we vary the disorder by doping with Al.

2. CRITICAL SCALING

It has been demonstrated that the dc -conductivity in laser ablated YBCO films can be described by appropriate scaling laws that do not depend on the applied magnetic field B .³ This fact supports the idea for the existence of a phase transition separating a "liquid" from a "glass" vortex phase. We test the universality of the critical exponents and scaling functions at the phase boundary $T_c(B)$ through I - V measurements in pure and Al-doped YBCO films, made by co-deposition of Y, BaF, Cu and Al, with an *ex-situ* postanneal in oxygen.⁶

Typical I - V curves for a $100 \mu\text{m} \times 42 \mu\text{m}$ strip on a 1000 \AA -thick film are shown in the inset of Fig. 1, where we define T_c to be the temperature at which $\log(V)$ vs. $\log(I)$ is closest to linear. In ref. 7, we

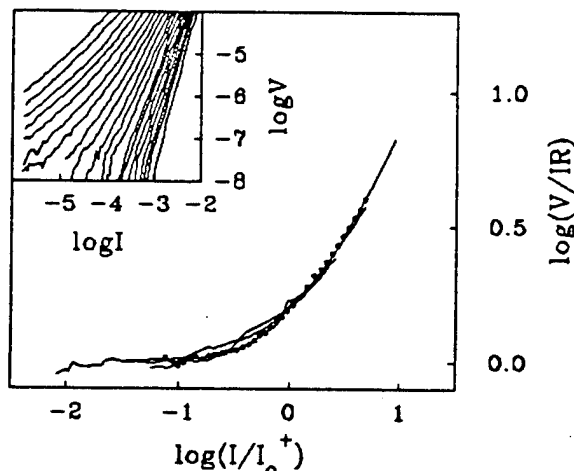


Figure 1. Scaling function for $T > T_c$, $B = 6\text{T}$. Data from a 3% (dots) and a 0% (lines) film collapse on the same curve. *Inset*: I - V s (in MKS units) for a 2% film at $54.3 \leq T \leq 73.3$ K and $B = 4\text{T}$.

collected the information from all our films (two pure YBCO films, one 2% Al and one 3% Al) in the range of fields $0.5 \leq B \leq 6$ T, and determined the scaling exponents of the transition from the I - V at T_c [$V \propto I^{3 \pm 0.2}$], the low-voltage resistance [$R \propto (T - T_c)^{7 \pm 0.3}$] and the crossover current separating the linear from the nonlinear conductivity [$I_0^+ \propto (T - T_c)^{3.3 \pm 0.3}$]. These exponents are in excellent agreement with the results from laser ablated YBCO films³. In Fig. 1, we go one step further to show that the scaling function describing the dc -conductivity above T_c is independent of Al concentration. All the above argue in favor of a

universal critical scaling in the vicinity of T_c .

3. TRANSITION WIDTH

Doping YBCO films with up to 7at% Al reduces uniformly the mean field transition T_c^B by 1.5 K per at%, and widens the superconducting transition at $B=0$.⁶ In the presence of a B field, it drastically reduces T_g , as shown in Fig. 2 (inset). For reference, our 2% film showed $T_g=62\pm0.5$ K at $B=4$ T, to be compared to $T_g=76.3$ K for our undoped film and $T_g=79.5$ K for a laser ablated film in ref. 3. This reduction can only partially be explained by the increase in the penetration depth λ_{ab} due to doping. The energy gain per unit length from a vortex core pinned in a defect $\epsilon = \phi_0^2/(64\pi^2\lambda_{ab}^2)$ decreases by a factor of 3 with 2at% doping, given that the zero-temperature λ_{ab} measured independently⁸ increases to 2800 Å relative to 1600 Å of pure YBCO. However, T_g decreases by only 20%. It is possible that Al introduces defects in the films that tend to raise T_g , like screw dislocations in the crystallites or edge dislocations in the grain boundaries. Such mechanism may dominate the reduction of ϵ at lower Al concentrations ($x < 0.01$) and consequently raise T_g above its value in pure YBCO.

4. CORRELATION LENGTH AND TIME

In Fig. 2 we illustrate that the resistivity $\rho(T)$ follows a scaling law up to a value of $\rho^* = 22 \pm 4 \mu\Omega$ cm, independent of the dopant concentration. Within $\pm 3\%$ error, $\rho(T)$ agrees with the form

$$\rho_s(T) = \rho^* [(T-T_g)/(T^*-T_g)]^{\nu} \quad (1)$$

for $T \leq T^*$, where T^* is the temperature at which $\rho(T) = \rho^*$. The same value of ρ^* fits all our data at fields $0.5 \leq B \leq 6$ T, despite the fact that Al doping doubles the normal state resistivity in samples with 3at% substituted Cu. In addition, we find that T^*-T_g is always $60 \pm 5\%$ of the resistive transition $T_c^B - T_g$, and varies from 3 to 30 K for the B-fields and Al concentrations we studied. Doped samples may thus be proved a useful tool in case a large critical temperature regime is required.

Eq. 1 sets a strong constraint for the magnitude of the vortex correlation length $\xi \propto (T-T_g)^{-\nu}$ and

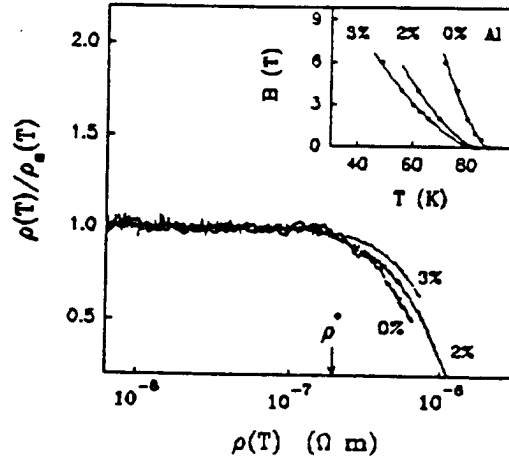


Figure 2. Deviation of the resistivity from power law at $B=4$ T. Inset: Phase boundary $B=B(T_g)$.

time $t \propto \xi^z$, with ν , z the static and dynamical critical exponent of the transition. In the framework of the vortex glass model, $\rho \propto (T-T_g)^{-(z-1)}$ and thus $\rho \propto \xi/t$. Therefore, at $T=T^*$, the ratio ξ/t is independent (similar to ρ^*) on the applied magnetic field, the width of the transition or the normal state resistivity of the sample. The magnitude of ξ and t can be measured independently by dc -⁷ and ac -⁹ conductivity measurements respectively, and provide quantitative checks for the theoretical models that describe the critical response of the vortex system.

We acknowledge support primarily by grant AFOSR-91-0188, and also by NSF-DMR 92-00870 and DOE grant DE-FG02-90ER45427.

REFERENCES

1. W.K. Kwok *et al.*, Phys. Rev. Lett. 69, 3370 (1992).
2. N.-C. Yeh *et al.*, Phys. Rev. B 45, 5654 (1992).
3. R.H. Koch *et al.*, Phys. Rev. Lett. 63, 1511 (1989).
4. D.S. Fisher *et al.*, Phys. Rev. B 38, 130 (1990).
5. D.R. Nelson and V.M. Vinokur, Phys. Rev. Lett. 68, 2398 (1991).
6. J.-T. Kim *et al.*, J. Appl. Phys. 72, 803 (1992).
7. D.G. Xenikos *et al.*, to be published.
8. E.R. Ulm *et al.*, to be published.
9. H.K. Olsson *et al.*, Phys. Rev. Lett. 66, 2661 (1991).

STATICS AND DYNAMICS OF THE MIXED STATE
IN PURE AND Al-DOPED $\text{YBa}_2\text{Cu}_3\text{O}_{7-\delta}$ HIGH-TEMPERATURE
SUPERCONDUCTORS

DISSERTATION

Presented in Partial Fulfillment of the Requirements for
the Degree Doctor of Philosophy in the Graduate
School of the Ohio State University

By

Dimitrios G. Xenikos, B.S., M.S.

The Ohio State University

1994

Dissertation Committee:

Prof. Thomas R. Lemberger

Prof. David G. Stroud

Prof. Gregory P. Lafyatis

Approved by

Advisor

Department of Physics

STATICS AND DYNAMICS OF THE MIXED STATE IN PURE AND Al-DOPED
 $\text{YBa}_2\text{Cu}_3\text{O}_{7-\delta}$ HIGH-TEMPERATURE SUPERCONDUCTORS

By

Dimitrios G. Xenikos, Ph.D.

The Ohio State University, 1994

Professor Thomas R. Lemberger, Adviser

The complexity of the properties of the mixed state in the high-temperature superconductors provides a challenge to both fundamental and applied research. The central issue is whether thermal fluctuations can destroy the defining property of superconductors- a vanishing linear resistivity. Early research on the static and dynamical properties of the mixed state answered the question in the affirmative, suggesting that true critical currents could not be obtained in these materials, and dissipation would dominate their behavior at technologically useful temperatures. However, as the quality of the samples improves and the sample disorder becomes better characterized, novel phenomena are revealed indicating that there is a transition in the phase diagram from a "liquid" vortex state with finite linear resistivity to a "glass" state with true critical currents. Issues relative to the nature of the transition and the role of the disorder that pins the vortices in the glass state are fiercely debated and are not by any means settled yet.

In our work we focus on films, where little has been done towards recording the

statics and the dynamics in the vicinity of the glass transition and in the low-temperature pinned vortex state. We demonstrate that the critical scaling near the transition does not depend on material properties of the normal and superconducting state, which are altered by doping the $\text{YBa}_2\text{Cu}_3\text{O}_{7-x}$ with Al. We propose empirical formulas that describe the complex conductivity of the vortex phases, and we estimate the magnitude of the fundamental quantities of the transition, namely, the vortex correlation length and time. We measure the strength of pinning in the glass phase, correlate it to the magnetic penetration depth, and provide the first evidence that the film admittance drops to zero over a few degrees Kelvin, a strong indication for a phase transition at the temperature where the sample disorder becomes ineffective to pin the vortex lattice. Finally, we suggest alternative ways to model the vortex excitations given the types of disorder present in our samples, and in the light of the theoretical models available at present.

This work was supported by contract No. AFOSR-91-0188.

Absence of a gap in the infrared reflectance of Ni-doped $\text{YBa}_2\text{Cu}_3\text{O}_{7-\delta}$ films

Michael J. Sumner, Jin-Tae Kim, and Thomas R. Lemberger

Department of Physics, The Ohio State University, Columbus, Ohio 43210

(Received 2 November 1992)

We study the effects of Ni doping on the infrared reflectance of $\text{YBa}_2(\text{Cu}_{1-x}\text{Ni}_x)_3\text{O}_{7-\delta}$ films with up to 4% substitution of Cu by Ni. Normal-state spectra indicate that the primary effect of Ni on the conduction carriers is to increase their elastic scattering rate. At 4 at. % Ni, the elastic-scattering rate is calculated to be large enough to generate a large absorption onset at the gap edge in the superconducting state, if a gap exists. The superconducting-state spectra show no evidence for such a feature. Comparisons with phenomenological models for the optical conductivity show that the conductivity, and hence the superconducting density of states, is very gapless.

I. INTRODUCTION

A great deal of effort has been expended studying the infrared spectra of $\text{YBa}_2\text{Cu}_3\text{O}_{7-\delta}$, and other oxide superconductors, as reviewed extensively in Refs. 1 and 2. After this effort, interpretation of the optical properties of $\text{YBa}_2\text{Cu}_3\text{O}_{7-\delta}$ remains controversial for both the normal and superconducting states.

One interpretation is the "two-component" model in which the normal-state optical conductivity arises from a conventional conduction band plus a "midinfrared band" involving bound electrons of uncertain origin.¹ In this model, the scattering rate $1/\tau$ for conduction electrons is roughly $2kT/\hbar$ for $T > T_c$,² and it decreases more rapidly upon cooling into the superconducting state.³⁻⁵ Hence, at low temperatures $T < T_c$, \hbar/τ is so much smaller than the superconducting energy gap $2\Delta(0)$ that the absorption onset at the gap frequency would be too small to observe, even for a BCS gap.⁶ In this model, all of the absorption observed at 10 K or lower is from the midinfrared band.

Another interpretation is the "one-component" model.² The normal-state optical conductivity arises from a single band of unconventional conduction carriers which are strongly coupled to an optically inactive boson of uncertain origin. The strong coupling generates an inelastic-scattering rate that increases linearly with frequency, and thereby accounts for the anomalously strong absorption observed in the midinfrared. The conduction carriers are responsible for absorption in the superconducting state. Small features in the reflectance spectra at 150 and 450 cm^{-1} are interpreted as gaps for excitations moving on the CuO chains and CuO_2 planes, respectively.

We discuss our data in terms of the two-component model, comprising Drude conduction carriers plus a midinfrared band. Our conclusions do not depend on this choice. Previous workers^{1,2} have applied this model to pure $\text{YBa}_2\text{Cu}_3\text{O}_{7-\delta}$ and found that the Drude conductivity corresponds well to the observed superconducting penetration depth $\lambda(0) = (m^*/ne^2\mu_0)^{1/2} \approx 160$ nm and normal-state resistivity $\rho(T) = m^*/ne^2\tau \approx 0.8 \mu\Omega \text{ cm}$ (T/K), where m^* is the effective band mass and n is the

density of conduction carriers. In other words, when the midinfrared band is subtracted from the experimental conductivity found by Kramers-Kronig analysis, the height and width of the remaining Drude peak correspond to the measured resistivity and to a scattering rate $\tau^{-1}(T) = \rho(T)/[\mu_0\lambda^2(0)]$.

We need to make an assumption about how the midinfrared band responds to Ni doping at the 4 at. % level. There is as yet no accepted model which would enable us to make physical estimates. Hence, we appeal to the spectra of Orenstein *et al.*⁷ on oxygen-depleted $\text{YBa}_2\text{Cu}_3\text{O}_{7-\delta}$ twinned crystals. Interpreting their conductivities at $T \ll T_c$ as the midinfrared band, we see that oxygen depletion monotonically reduces its magnitude without affecting its frequency dependence. Reducing T_c to 50 K, by removing one-third of the chain oxygens to reach $\text{O}_{6.6}$, halves the midinfrared band conductivity for $\nu < 2000 \text{ cm}^{-1}$. Two comments are in order. First, analysis of our data with a midinfrared band anywhere in this range leads to the same conclusions, primarily because the Drude conductivity is so much larger than the midinfrared band below about 400 cm^{-1} . Second, there is no evidence, either from doping levels, or T_c , or the Hall coefficient, that 4% Ni has an effect nearly as large as that of removing 33% of the chain oxygens. Therefore, we use for convenience the same T -independent Lorentz-oscillator parameterization of the midinfrared band which Kamaras *et al.*⁶ used to fit their data on twinned $\text{YBa}_2\text{Cu}_3\text{O}_{7-\delta}$ films. This conductivity falls at the low end of the range found by Orenstein *et al.*⁷

II. Ni-DOPED $\text{YBa}_2\text{Cu}_3\text{O}_{7-\delta}$ FILMS

Information about $\text{YBa}_2(\text{Cu}_{1-x}\text{Ni}_x)_3\text{O}_{7-\delta}$ comes primarily from bulk ceramic samples.^{8,9} The solubility limit is 10 at. %. As in Zn doping, the crystal remains orthorhombic, suggesting that the CuO chains remain intact and that a substantial fraction of the Ni goes into the CuO_2 planes. Smaller ionic radius dopants¹⁰ such as Al, Co, and Fe make the lattice tetragonal above 4 at. %, and apparently strongly prefer chain sites. Direct determinations are difficult, and site preferences for Ni remain con-

troverial. T_c decreases monotonically, but $T_c(x)$ curves vary somewhat from group to group,¹¹ perhaps because different annealing procedures lead to different site preferences for Ni. In our films, the relatively short postannealing time of 1 h at a peak temperature of 900°C, compared with weeks at comparable temperatures for ceramic samples, may favor random siting. In the end, $T_c(x)$ vs x for our films falls among curves reported for bulk ceramic samples.

Ni likely substitutes as Ni^{2+} for Cu^{2+} , so it should not affect the carrier density significantly. The Hall coefficients $R_H(T)$ for 3.3 at. % and 7 at. % Ni ceramics are identical to pure $\text{YBa}_2\text{Cu}_3\text{O}_{7-\delta}$ within the $\pm 30\%$ uncertainty imposed by ceramic samples.¹² In contrast, R_H for O-depleted $\text{YBa}_2\text{Cu}_3\text{O}_{7-\delta}$ with $T_c \approx 66$ K is about four times larger than for pure $\text{YBa}_2\text{Cu}_3\text{O}_{7-\delta}$.¹² 4 at. % Ni has a negligible effect on carrier density.

As discussed below, the dc resistivity of a patterned 3 at. % Ni $\text{YBa}_2(\text{Cu}_{1-x}\text{Ni}_x)_3\text{O}_{7-\delta}$ film (Fig. 2) indicates a residual resistivity of about $250 \mu\Omega \text{ cm}$, and a corresponding elastic-scattering rate of about $250 \text{ K} \times k/\hbar$. (k is Boltzmann's constant.) The resistivity deduced from our reflectance spectra for 4 at. % Ni are about half of this, which we consider good agreement.

The films are made by codeposition of Y, BaF_2 , Cu, and Ni onto (100) SrTiO_3 substrates in the presence of 3 microtorr of O_2 , with a postanneal in moist oxygen at 900°C.¹³ The films are nominally 300-nm thick and about 1 cm in diameter. Thickness is determined from measurements on identically prepared patterned films. x is the nominal concentration of Ni from the measured Ni and Cu deposition rates. We have made good films up to 10 at. % Ni.

The structure of each film is characterized by x-ray diffraction, scanning electron microscopy (SEM), and Raman spectroscopy.¹⁴ Powder x-ray diffraction indicates single-phase films highly oriented with the c axis perpendicular to the substrate. These results put an upper limit of about 10% on the volume of film consisting of misoriented grains and second phases. SEM micrographs show surface structure on a few percent of the sample surface, examples of which are in Ref. 13. This structure appears to be misoriented grains with dimensions ranging from 0.2 to $5 \mu\text{m}$. These grains do not show up in Raman spectra, even though they should have much stronger Raman signals than the properly oriented grains. We conclude that misoriented grains do not extend deeply into the film. Raman also is very sensitive to some second phases with large Raman signals, such as BaCuO_2 , but reveals none of these phases in the films. The overwhelming majority of the volume of our films consists of highly oriented grains of $\text{YBa}_2(\text{Cu}_{1-x}\text{Ni}_x)_3\text{O}_{7-\delta}$.

Figure 1 shows the low-frequency inductive response of films with up to 6% Ni. The ordinate is the change in the inductance of a tightly wound 10-turn 6-mm diameter pancake coil pressed gently against the sample film.¹⁵ The maximum current density induced in the film is about 300 A/cm^2 . These data have three important features. First, the onset of superconductivity is very sharp, as shown by the sharp "corner" at T_c . Poorer

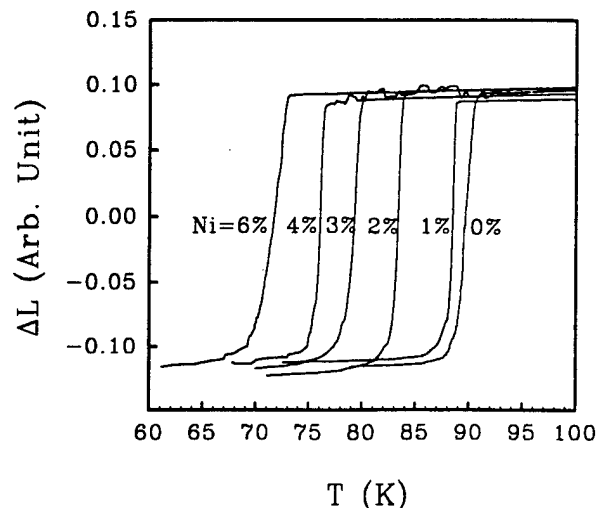


FIG. 1. Change in inductance of a pancake coil pressed against a film. The onset of superconductivity is sharp, and T_c decreases smoothly as Ni is added.

quality films show a rounded onset. Second, the transition widths are only a few percent of T_c , ensuring reasonable homogeneity. Third, $T_c(x)$ decreases linearly with increasing Ni concentration, demonstrating reproducibility of the fabrication technique. The rate of suppression of T_c with Ni doping is well within the range of values reported for bulk ceramic samples.⁹⁻¹¹

Figure 2 shows the resistivities of films made identically to those reported here, then patterned into strips.¹³ Our pure $\text{YBa}_2\text{Cu}_3\text{O}_{7-\delta}$ films have resistivities $\rho(100 \text{ K}) \approx 100 \pm 20 \mu\Omega \text{ cm}$; $\rho(T)$ extrapolates to zero at $T=0$, and the transitions are a couple of Kelvins wide. T_c ranges from 88 to 92 K. Figure 2 shows that 3% Ni in-

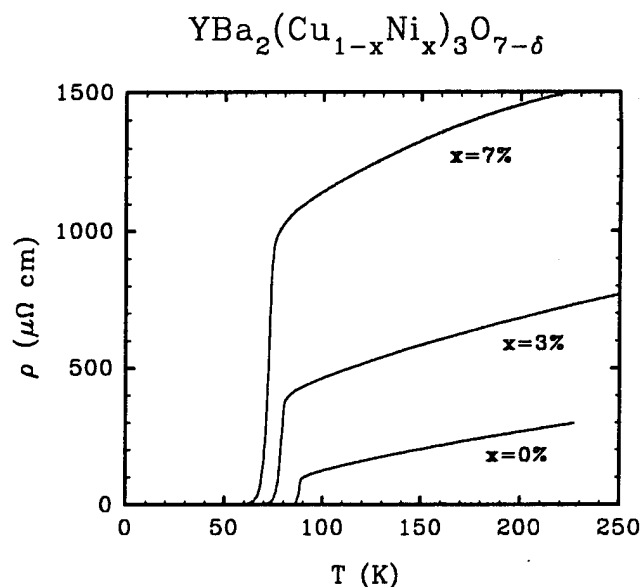


FIG. 2. Resistivities vs T of 0%, 3%, and 7% Ni-doped $\text{YBa}_2(\text{Cu}_{1-x}\text{Ni}_x)_3\text{O}_{7-\delta}$ films.

creases $\rho(T)$ and causes an apparent residual resistivity $\rho(0) \approx 250 \mu\Omega \text{ cm}$. The data at 7% Ni continue this trend. For comparison, the resistivity of Zn-doped $\text{YBa}_2\text{Cu}_3\text{O}_{7-\delta}$ twinned crystals increases with Zn concentration at about half the rate we observe for Ni doping.¹⁶

We conclude that Ni-doped $\text{YBa}_2\text{Cu}_3\text{O}_{7-\delta}$ films are of sufficient quality to warrant extensive optical measurements. Although films are twinned and less well characterized than untwinned crystals might be, and transmission of some radiation through the film into the substrate precludes a Kramers-Kronig determination of the optical conductivity, still there are several important advantages of films for optical measurements. One is that some features in the reflectance are traceable to the SrTiO_3 substrate, which means that all of the film is probed by the radiation, not just the surface as for a crystal. Thus, the measured resistivity and inductive response of the film are those of the carriers reflecting the radiation. Another advantage is that, if there is an energy gap, then there is an interference between the reflectances of the film and the SrTiO_3 substrate which amplifies the calculated drop in reflectance at the gap frequency. Both of these advantages will be exploited below.

III. NORMAL-STATE REFLECTANCE SPECTRA

The reflectances of our films are measured with a Bomem Corp. Fourier transform spectrometer with a spot diameter of 7 mm and with an angle of incidence 11° from normal. The high value of the dielectric function $\epsilon(\omega)$ of $\text{YBa}_2\text{Cu}_3\text{O}_{7-\delta}$ in the infrared ensures that radiation in the film is polarized almost entirely in the plane of the film. The sample film and a Au mirror are mounted several centimeters apart on the cold finger of a helium-flow cryostat. The cold finger can be raised and lowered, thereby placing either the sample or the Au mirror in the optical path of the spectrometer. Typically, at each temperature several alternate measurements of film and Au mirror ensure an accurate determination of the relative reflectance of the sample. When Au mirrors are mounted at both locations on the cold finger, alternate measurements produce reflectances which agree within 1%. The difference is reproducible and is taken into account in our analysis.

Because some radiation penetrates through the films into the SrTiO_3 substrates, a Kramers-Kronig analysis does not produce accurate values for the optical conductivity of the films. Therefore, we compare our reflectance data with calculated model reflectances. The complete model for our samples comprises a conducting or superconducting film 300-nm thick on an infinitely thick SrTiO_3 substrate. This is a good approximation, since the actual substrate thickness of 1 mm is much larger than the longest wavelength of interest here. The spectrometer is run at a resolution of 4 cm^{-1} to average over the resonances due to standing waves in the substrate.

The normal-state optical response of the films comprises Drude carriers plus a broad midinfrared band, so that the complex conductivity is given by

$$\sigma(\omega) = \sigma_0 / (1 - i\omega\tau) + \sigma_{\text{MIR}}(\omega). \quad (1)$$

The plasma frequency of the Drude carriers is taken to be $\nu_p/c = 8200 \text{ cm}^{-1}$ ($\omega_p = 1.55 \times 10^{15} \text{ rad/s}$; $\hbar\omega_p = 1 \text{ eV}$), independent of temperature and Ni concentration.¹ For reference, this value of ν_p yields $\lambda(0) = c/\omega_p = 190 \text{ nm}$, and for $\rho = 100 \mu\Omega \text{ cm}$, it corresponds to a scattering rate

$$1/\tau = \rho \epsilon_0 \omega_p^2 = 2 \times 10^{13} \text{ s}^{-1} = 2\pi c \times 106 \text{ cm}^{-1} \\ = 160 \text{ K} \times k/\hbar. \quad (2)$$

The midinfrared band is shown in Fig. 3. The peak value of the real part is about $(800 \mu\Omega \text{ cm})^{-1}$. The lowest conduction carrier conductivity at dc is about $(500 \mu\Omega \text{ cm})^{-1}$, for 4% Ni at 300 K. Hence, both the real and imaginary parts of the Drude conductivity dominate over the midinfrared band at low frequencies.

A four-parameter model of the measured conductivities and reflectances of SrTiO_3 at 300 and 85 K are shown in Figs. 4 and 5.¹⁷ We use the 300-K data to model reflectances at 300 K and the 85-K data to model reflectances at 100 and 10 K. Note the strength and temperature dependence of the phonon at the lowest frequency; this phonon is apparent in our spectra and is very useful in determining the best-fit resistivity of our films. The phonons at 175 and 540 cm^{-1} are also present, but weaker.

Let us begin with pure $\text{YBa}_2\text{Cu}_3\text{O}_{7-\delta}$. Figure 6 shows reflectance spectra for $50 < \nu < 600 \text{ cm}^{-1}$ of a pure $\text{YBa}_2\text{Cu}_3\text{O}_{7-\delta}$ film at 10, 100, and 300 K. The solid curves are model calculations. Each data set is a superposition of spectra taken with different light sources, beam splitters, and detectors as appropriate for different frequency ranges. The noise level varies, being especially large near 200 and 550 cm^{-1} , but is about $\pm 0.75\%$ for most frequencies. In general, the film becomes more

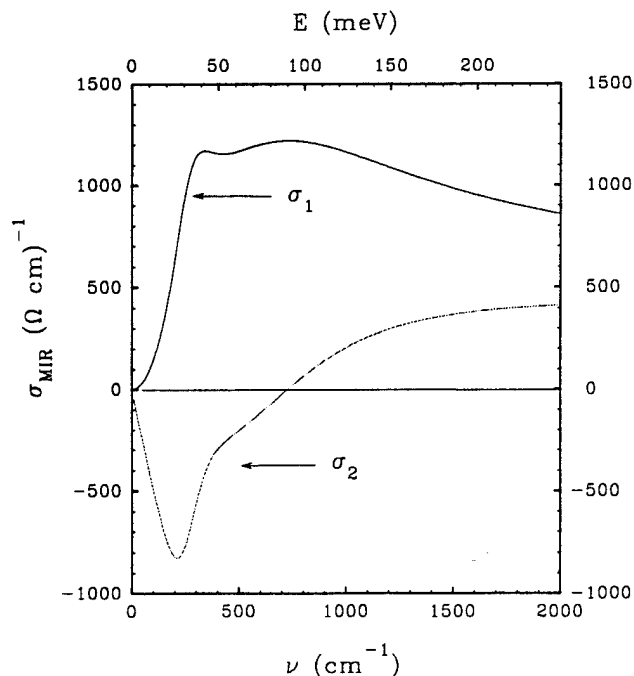


FIG. 3. Real and imaginary parts of the midinfrared band used to model our films.

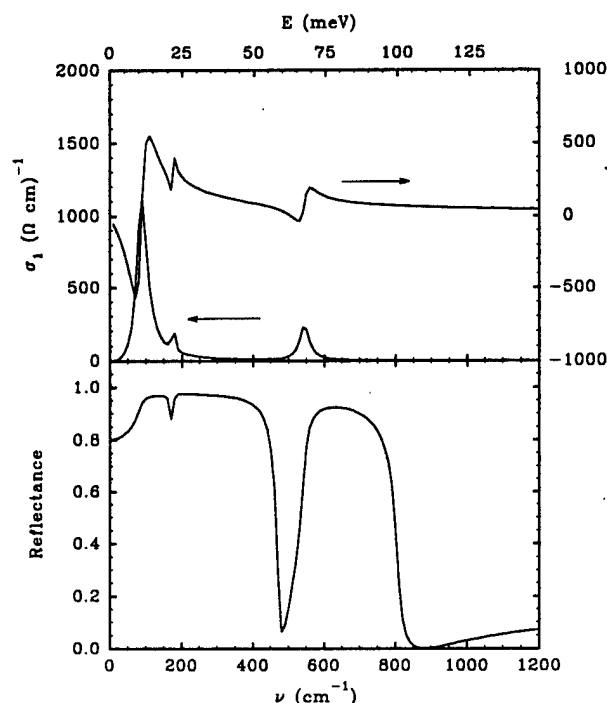


FIG. 4. Real part of the conductivity and reflectance of SrTiO_3 at 300 K.

reflective as it cools, as expected from a reduced resistivity. At 10 K, the film is nearly perfectly reflecting at the lowest frequencies. Apparently the surface structure observed under the SEM does not affect the film reflectance here.

Now consider more detail. The 300 K reflectance does

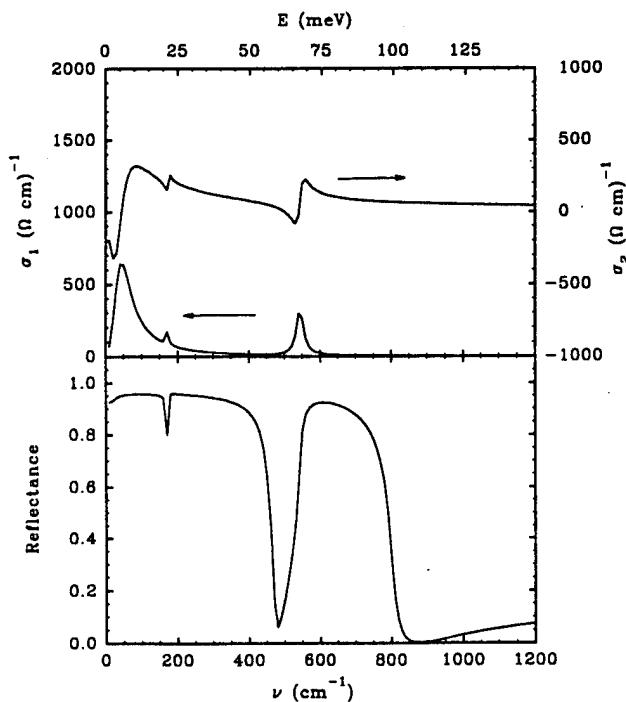


FIG. 5. Real part of the conductivity and reflectance of SrTiO_3 at 85 K.

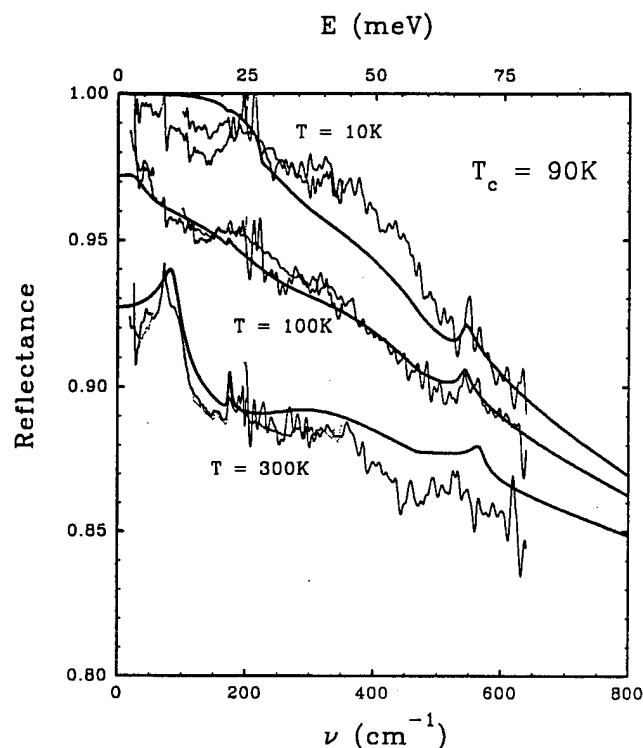


FIG. 6. Reflectance of a pure $\text{YBa}_2\text{Cu}_3\text{O}_{7-\delta}$ film at 10, 100, and 300 K. Solid curves are model calculations with $\rho(100 \text{ K}) = 125 \mu\Omega \text{ cm}$ and $\rho(300 \text{ K}) = 320 \mu\Omega \text{ cm}$.

not turn up toward unity at low frequency as expected for conductors. Instead, it has a maximum at $\nu \approx 100 \text{ cm}^{-1}$. The model calculation, which uses $\rho(300 \text{ K}) = 320 \mu\Omega \text{ cm}$, reveals that this feature arises from radiation passing through the film and interacting with the SrTiO_3 phonon at 80 cm^{-1} . At 100 K, the feature is softened because the film is less resistive [the model calculation uses $\rho(100 \text{ K}) = 125 \mu\Omega \text{ cm}$], so less light gets into the substrate. At 10 K, the model calculation uses a gap $2\Delta = 220 \text{ cm}^{-1} = 3.5kT_c$ and $\rho = 10 \mu\Omega \text{ cm}$. This is the clean limit, so the optical conductivity of the superconducting carriers is a δ function at $\nu = 0$. The reasonable agreement justifies our choice of midinfrared conductivity.

Figure 7 shows reflectance spectra for a 1% Ni film at 10, 100, and 300 K. The 100 and 300 K spectra are different from those of pure $\text{YBa}_2\text{Cu}_3\text{O}_{7-\delta}$, but not by very much. The model calculations use the same resistivities, $\rho(300 \text{ K}) = 320 \mu\Omega \text{ cm}$ and $\rho(100 \text{ K}) = 125 \mu\Omega \text{ cm}$. The reflectance should be almost identical to pure $\text{YBa}_2\text{Cu}_3\text{O}_{7-\delta}$ at such a low doping level, so differences indicate the "noise" from sample-to-sample variations. We will see that the gap feature expected from these films is much larger than sample-to-sample variations.

Figure 8 shows reflectance spectra for a 2% Ni film over a wide frequency range. The data above 1000 cm^{-1} show that the doped films behave the same as undoped $\text{YBa}_2\text{Cu}_3\text{O}_{7-\delta}$ in this range, becoming steadily less reflective. Below 600 cm^{-1} , this film is not quite as reflective as pure $\text{YBa}_2\text{Cu}_3\text{O}_{7-\delta}$, and its reflectance does

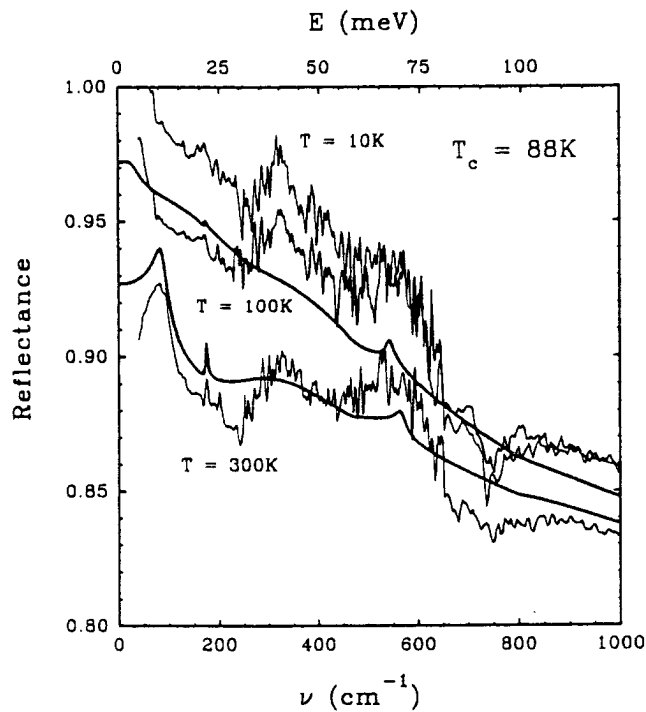


FIG. 7. Reflectance of a $\text{YBa}_2(\text{Cu}_{0.99}\text{Ni}_{0.01})_3\text{O}_{7-\delta}$ film at 10, 100, and 300 K. Solid curves are model calculations with $\rho(100 \text{ K}) = 125 \mu\Omega \text{ cm}$ and $\rho(300 \text{ K}) = 320 \mu\Omega \text{ cm}$.

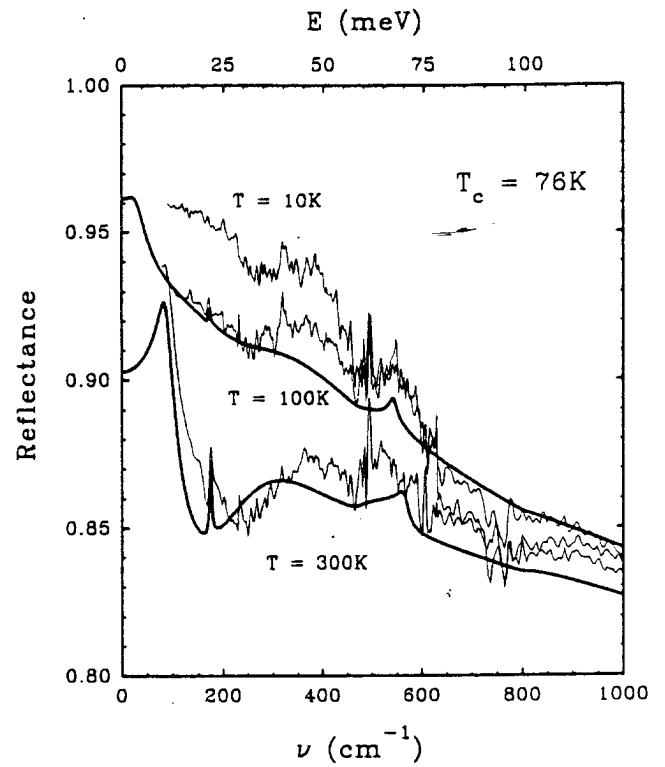


FIG. 9. Reflectance of a $\text{YBa}_2(\text{Cu}_{0.96}\text{Ni}_{0.04})_3\text{O}_{7-\delta}$ film at 10, 100, and 300 K. Solid curves are model calculations with $\rho(100 \text{ K}) = 220 \mu\Omega \text{ cm}$ and $\rho(300 \text{ K}) = 520 \mu\Omega \text{ cm}$.

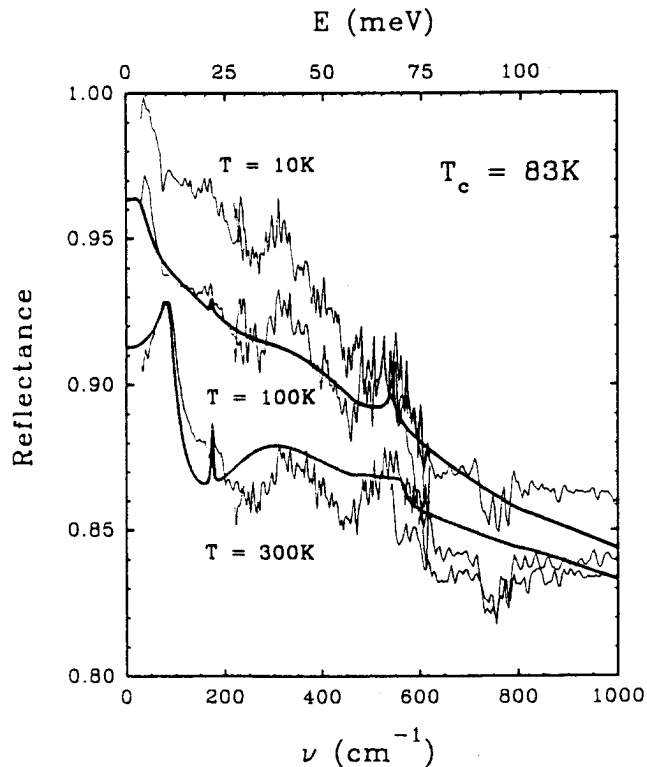


FIG. 8. Reflectance of a $\text{YBa}_2(\text{Cu}_{0.98}\text{Ni}_{0.02})_3\text{O}_{7-\delta}$ film at 10, 100, and 300 K. Solid curves are model calculations with $\rho(100 \text{ K}) = 200 \mu\Omega \text{ cm}$ and $\rho(300 \text{ K}) = 480 \mu\Omega \text{ cm}$.

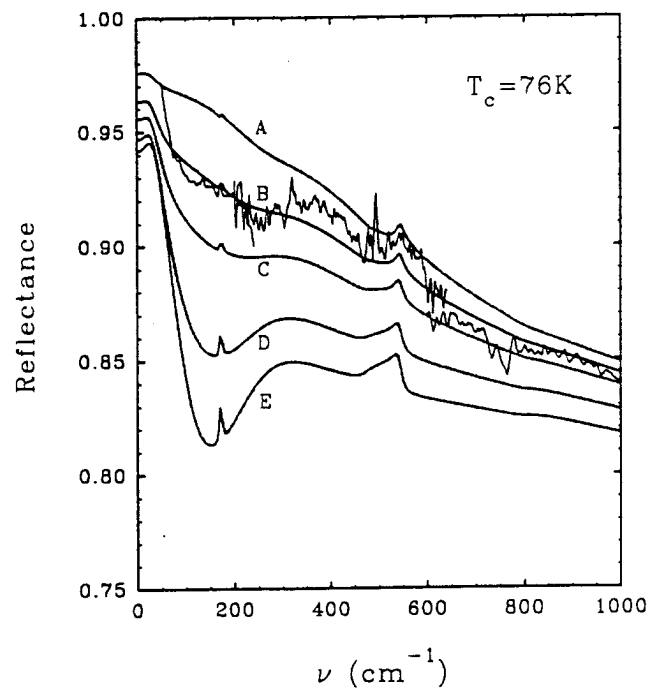


FIG. 10. Reflectance of a $\text{YBa}_2(\text{Cu}_{0.96}\text{Ni}_{0.04})_3\text{O}_{7-\delta}$ film at 100 K with model calculations for $\rho = 100, 200, 300, 500,$ and $700 \mu\Omega \text{ cm}$, curves A-E, respectively.

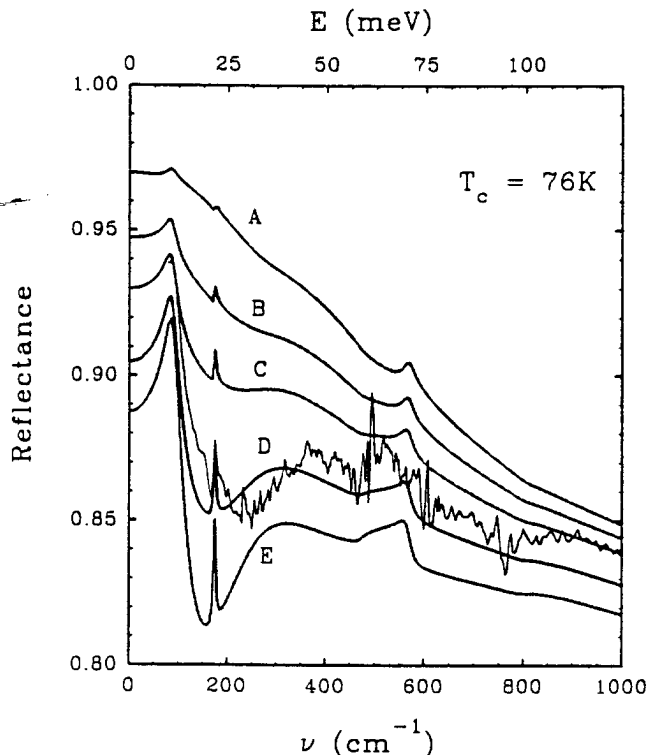


FIG. 11. Reflectance of a $\text{YBa}_2(\text{Cu}_{0.96}\text{Ni}_{0.04})_3\text{O}_{7-\delta}$ film at 300 K with model calculations for $\rho = 100, 200, 300, 500$, and $700 \mu\Omega \text{ cm}$, curves A–E, respectively.

not increase as much when it cools from 300 to 100 K. Model calculations, using $\rho(300 \text{ K}) = 480 \mu\Omega \text{ cm}$ and $\rho(100 \text{ K}) = 200 \mu\Omega \text{ cm}$, show that these features indicate a higher resistivity, as expected.

Figure 9 shows the reflectance of a 4% Ni film. The decreased reflectances at 300 and 100 K relative to pure $\text{YBa}_2\text{Cu}_3\text{O}_{7-\delta}$ are described well by an increase in resistivity to $\rho(300 \text{ K}) = 520 \mu\Omega \text{ cm}$ and $\rho(100 \text{ K}) = 220 \mu\Omega \text{ cm}$. Let us quantify the uncertainty in the optical determination of the resistivity. Figures 10 and 11 show the 100 and 300 K spectra for 4% Ni with curves calculated for several different resistivities. The most important feature in determining the best-fit resistivity is the steep drop below 100 cm^{-1} because the Drude conductivity is much larger than the midinfrared band in this range. The best fits are for $\rho = 220 \pm 50 \mu\Omega \text{ cm}$ and $520 \pm 50 \mu\Omega \text{ cm}$, respectively. These values are 100 and $200 \mu\Omega \text{ cm}$ larger than for pure $\text{YBa}_2\text{Cu}_3\text{O}_{7-\delta}$. We conclude that $100 \pm 50 \mu\Omega \text{ cm}$ is a reasonable estimate of the residual resistivity introduced by 4% Ni. This is somewhat less than the $250 \mu\Omega \text{ cm}$ inferred from the dc resistivity of a 3 at. % Ni film (Fig. 2), but in reasonably good agreement.

IV. SUPERCONDUCTING-STATE REFLECTANCE SPECTRA

The spectra at 10 K (Figs. 6–9) show that the films become gradually less reflective below 600 cm^{-1} as Ni is added. More significantly, no sharp features emerge.

Since the spectra are similar, we will concentrate our analysis on the 4% Ni film because it has the largest scattering rate.

First of all, let us calculate what would occur if all of the conduction carriers condensed into a conventional superconducting state. We obtain the frequency dependence of the conductivity from the theory of Chang and Scalapino¹⁸ (CS) for layered superconductors with weak electron-boson coupling. In the CS theory, currents are constrained to flow parallel to the planes so the anomalous skin effect does not occur for long mean free paths. The CS model applies at all temperatures and for electron-scattering rates ranging from clean $\hbar/\tau < 2kT_c$ to dirty $\hbar/\tau > 2kT_c$ limits. Of course, area missing from the optical conductivity at finite frequencies is found in a δ function at zero frequency. We examine dc conductivities of $\sigma_0 = 1/50, 1/100$, and $1/150 \mu\Omega \text{ cm}$, corresponding to $1/\tau \approx 53, 106$, and 160 cm^{-1} , respectively. The complete model includes the midinfrared band and an infinitely thick SrTiO_3 substrate.

Figure 12 shows the reflectance of the 4% Ni film at 10 K together with curves calculated for $2\Delta = 185 \text{ cm}^{-1} = 3.5kT_c$ ($T_c = 76 \text{ K}$) and various resistivities. Figure 13 shows the same data with curves calculated for $2\Delta = 400 \text{ cm}^{-1} = 7.6kT_c$. Note that the abrupt rise at about 70 cm^{-1} in the measured reflectance is associated with a substrate phonon which behaves differently in different substrates. Also, the “break” at 600 cm^{-1} in the measured reflectance is associated with uncertainty/noise

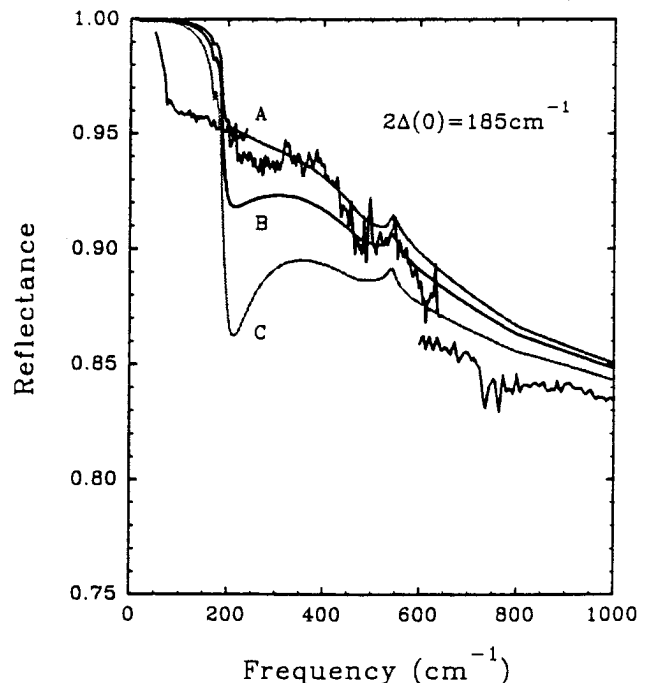


FIG. 12. Reflectance of a $\text{YBa}_2(\text{Cu}_{0.96}\text{Ni}_{0.04})_3\text{O}_{7-\delta}$ film at 10 K with model calculations for $2\Delta = 185 \text{ cm}^{-1} = 3.5kT_c$ and $\rho = 50, 100$, and $200 \mu\Omega \text{ cm}$, curves A–C, respectively. Abrupt changes in reflectance at 70 and 600 cm^{-1} are artifacts associated with the substrate and a change in infrared detectors, respectively.

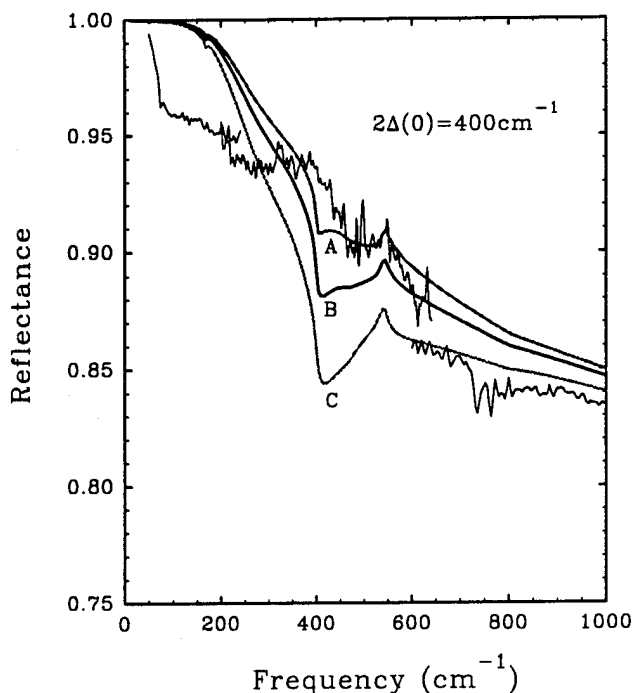


FIG. 13. Reflectance of a $\text{YBa}_2(\text{Cu}_{0.96}\text{Ni}_{0.04})_3\text{O}_{7-\delta}$ film at 10 K with model calculations for $2\Delta = 400 \text{ cm}^{-1} = 7.6kT_c$ and $\rho = 50, 100, \text{ and } 200 \mu\Omega \text{ cm}$, curves A–C, respectively.

in the pyroelectric detector used above 600 cm^{-1} . Increasing 2Δ beyond 400 cm^{-1} moves the model into the clean limit in which absorption is entirely from the midinfrared band, so there is no gap feature. Note the steep drop between 200 cm^{-1} and $2\Delta(0)$ and the minimum at $2\Delta(0)$ in the calculated reflectances. The minimum results from interference between the responses of the substrate and film, as discussed in Ref. 19. We emphasize that such strong features could not be masked by whatever is responsible for the 1–2 % discrepancies between the model calculations and data in the normal state. They are absent. The conduction carriers do not condense into a BCS-like state with a sharply defined energy gap.

The question then becomes, how non-BCS must the superconducting state be? We proceed by comparing physically motivated phenomenological models for the conductivity of the superconducting electrons with the data. Of course, in each of these models area missing from the optical conductivity at finite frequencies resides in a δ function at zero frequency.

The simplest model is motivated by the idea that some of the carriers, e.g., those on the CuO chains, remain “normal” at low temperatures. Thus, the conductivity of the conduction carriers consists of a fraction f_s that go superconducting and have a gap and a fraction $1-f_s$ which remain normal. Figure 14 shows reflectances calculated for $f_s = 0.2, 0.4, \text{ and } 0.6$ superimposed on the 10 K spectrum of the 4% Ni film. While the best fit is for $f_s = 0$, keeping in mind the differences between data and model in the normal state, we conclude that up to 40% of the carriers could go superconducting with a BCS-like density of states, if the other 60% remain normal. The

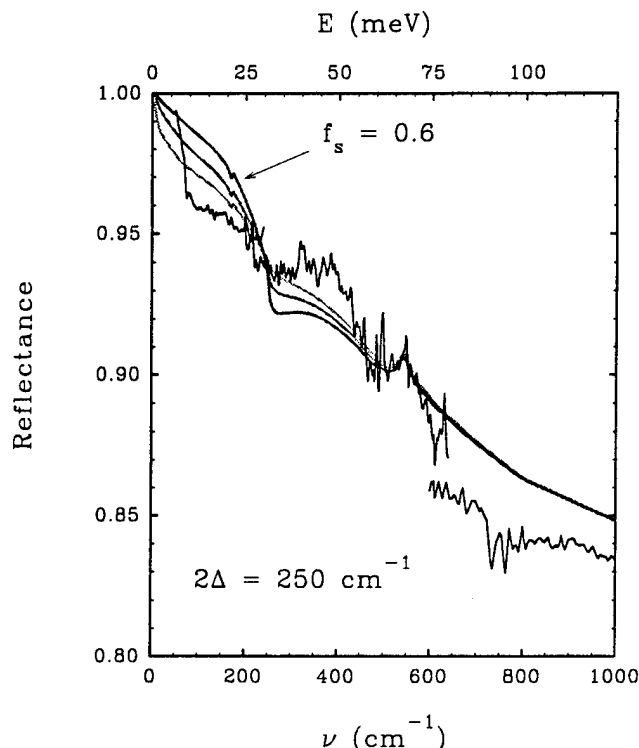


FIG. 14. Reflectance of a $\text{YBa}_2(\text{Cu}_{0.96}\text{Ni}_{0.04})_3\text{O}_{7-\delta}$ film at 10 K with two-fluid-model calculations for $f_s = 0.2, 0.4, \text{ and } 0.6$; $2\Delta = 250 \text{ cm}^{-1} = 4.7kT_c$; and $\rho = 100 \mu\Omega \text{ cm}$. The conductivities of the normal and superconducting carriers are shown in Fig. 15, labeled “normal drude” and “CS”, respectively.

calculated curve for 60% superconducting electrons is unacceptable primarily because it drops too steeply between 100 and 200 cm^{-1} , and secondarily because its absolute value at low frequency is higher than that observed. The steep drop arises from the abrupt increase in the real part of the conductivity at the gap frequency. Any theory with an abrupt feature superimposed on a smooth background conductivity will disagree with the data. The best-fit conductivity in this “two-fluid” model is very non-BCS in that at least 60% of the electrons remain normal. Note that a factor of 2.5 reduction in superfluid density implies that the penetration depth $\lambda(0)$ increases by a factor of $\sqrt{2.5}$ from pure $\text{YBa}_2\text{Cu}_3\text{O}_{7-\delta}$.

While we are considering coexisting normal and superconducting carriers, we should digress a moment to consider an inhomogeneous film with a putative normal layer on top of a superconducting layer. Model calculations of a three-layer system of normal film over superconducting film over substrate yield essentially the same results as the above calculation because infrared radiation penetrates through both layers. Thus, this type of inhomogeneity could explain our data only if the superconducting layer were less than 40% of the film thickness. Such a large inhomogeneity is not possible in our films.

Finally, let us examine phenomenological models in which the optical conductivity of the superconducting carriers is smooth, rather than having an abrupt feature at the gap edge. Perhaps then we can fit the data with a

response explains the effect of Ni on the normal-state spectra entirely in terms of the dependence of the scattering rate of the conduction electrons on temperature and Ni concentration. The relatively flat and featureless reflectance spectra in the superconducting state can be understood in this framework only if the conduction electron response is very gapless and therefore very non-BCS.

Experimentally, we need data on more doped systems with other dopants with different spin states and site preferences. Measurements on doped crystals would be very useful, for comparison in the midinfrared range. Also, we need corroborating evidence through direct low-frequency measurements of the penetration depth, as well as measurements in the far infrared, where $\lambda(0)$ can be determined from the increase in reflectance toward

unity that must occur even in very thin superconducting films.

ACKNOWLEDGMENTS

This work is based upon work supported in part by NSF Low-Temperature Physics Grant Nos. DMR 85-15370 and 88-22242 and from Ohio Edison Materials and Technology Centers. Substantial support for development of film fabrication and characterization techniques came additionally from AFOSR-91-0188 and DOE Grant No. DE-FG02-90ER45427 through the Midwest Superconductivity Consortium. We gratefully acknowledge discussions with David Tanner and Gordon Thomas.

- ¹T. Timusk and D. B. Tanner, in *Physical Properties of High-Temperature Superconductors I*, edited by D. M. Ginsberg (World Scientific, New York, 1989), p. 339.
- ²D. B. Tanner and T. Timusk, in *Physical Properties of High-Temperature Superconductors III*, edited by D. M. Ginsberg (World Scientific, New York, 1992), p. 363.
- ³D. B. Romero *et al.*, Phys. Rev. Lett. **68**, 1590 (1992).
- ⁴M. C. Nuss, P. M. Mankiewich, M. L. O'Malley, E. H. Westerwick, and P. B. Littlewood, Phys. Rev. Lett. **66**, 3305 (1991).
- ⁵D. A. Bonn, P. Dosanjh, R. Liang, and W. N. Hardy, Phys. Rev. Lett. **68**, 2390 (1992).
- ⁶K. Kamaras *et al.*, Phys. Rev. Lett. **64**, 84 (1990); **64**, 1692 (1990).
- ⁷J. Orenstein *et al.*, Phys. Rev. B **42**, 6342 (1990).
- ⁸J. T. Markert, Y. Dalichaouch, and M. B. Maple, in *Physical Properties of High-Temperature Superconductors I*, edited by D. M. Ginsberg (World Scientific, New York, 1989), p. 265.
- ⁹L. H. Greene and B. H. Bagley, in *Physical Properties of High-Temperature Superconductors II*, edited by D. M. Ginsberg (World Scientific, New York, 1990), p. 509.
- ¹⁰D. M. Ginsberg, in *Physical Properties of High-Temperature Superconductors I*, edited by D. M. Ginsberg (World Scientific, New York, 1989), p. 1.
- ¹¹Compare $T_c(x)$ curves from Fig. 28 of Ref. 8 and Fig. 24 of Ref. 9, for example.
- ¹²N. P. Ong, in *Physical Properties of High-Temperature Superconductors II*, edited by D. M. Ginsberg (World Scientific, New York, 1990), p. 459.
- ¹³J.-T. Kim, D. G. Xenikos, A. Thorns, and T. R. Lemberger, J. Appl. Phys. **72**, 803 (1992).
- ¹⁴K.-M. Ham, J.-T. Kim, R. Sooryakumar, and T. R. Lemberger, Phys. Rev. B (to be published).
- ¹⁵D. G. Xenikos and T. R. Lemberger, Rev. Sci. Instrum. **60**, 831 (1989).
- ¹⁶T. R. Chien, Z. Z. Wang, and N. P. Ong, Phys. Rev. Lett. **67**, 2088 (1991).
- ¹⁷A. S. Barker and M. Tinkham, Phys. Rev. **125**, 1527 (1962); **145**, 391 (1966).
- ¹⁸J.-J. Chang and D. J. Scalapino, Phys. Rev. B **40**, 391 (1989).
- ¹⁹M. J. Sumner, Ph.D. thesis, The Ohio State University, 1992 (unpublished).
- ²⁰S. Skalski, O. Betbeder-Matibet, and P. R. Weiss, Phys. Rev. **136**, A1500 (1964).
- ²¹M. Frick and T. Schneider, Z. Phys. B **88**, 123 (1992).
- ²²P. Monthoux, A. V. Balatsky, and D. Pines, Phys. Rev. B **46**, 14 803 (1992).
- ²³E. J. Nicol and J. P. Carbotte, Phys. Rev. B **44**, 7741 (1991).
- ²⁴P. B. Littlewood and C. M. Varma, Phys. Rev. B **46**, 405 (1992).